

## JCMT 850 $\mu$ m continuum observations of density structures in the G35 molecular complex

XIANJIN SHEN,<sup>1</sup> HONG-LI LIU,<sup>1</sup> ZHIYUAN REN,<sup>2,3,4</sup> ANANDMAYEE TEJ,<sup>5</sup> DI LI,<sup>2,3,4,6</sup> HAUYU BAOBAB LIU,<sup>7,8</sup> GARY A. FULLER,<sup>9,10</sup> JINJIN XIE,<sup>2</sup> SIHAN JIAO,<sup>3,4</sup> AIYUAN YANG,<sup>2,11,12</sup> PATRICK M. KOCH,<sup>13</sup> FENGWEI XU,<sup>14,15</sup> PATRICIO SANHUEZA,<sup>16,17</sup> PHAM NGOC DIEP,<sup>18</sup> NICOLAS PERETTO,<sup>19</sup> R.K. YADAV,<sup>20</sup> BUSABA H. KRAMER,<sup>12,20</sup> KOICHIRO SUGIYAMA,<sup>20</sup> MARK G. RAWLINGS,<sup>21</sup> CHANG WON LEE,<sup>22,23</sup> KEN'ICHI TATEMATSU,<sup>16,17</sup> DANIEL HARSONO,<sup>24</sup> DAVID EDEN,<sup>25</sup> WOOJIN KWON,<sup>26,27</sup> CHAO-WEI TSAI,<sup>2,28,4</sup> GLENN J. WHITE,<sup>29,30</sup> KEE-TAE KIM,<sup>31,23</sup> TIE LIU,<sup>32</sup> KE WANG,<sup>14</sup> SIJU ZHANG,<sup>14</sup> WENYU JIAO,<sup>14,15</sup> DONGTING YANG,<sup>33</sup> SWAGAT R. DAS,<sup>34,35</sup> JINGWEN WU,<sup>2,4</sup> AND CHEN WANG<sup>2</sup>

<sup>1</sup>School of Physics and Astronomy, Yunnan University, Kunming, 650091, People's Republic of China

<sup>2</sup>National Astronomical Observatories, Chinese Academy of Sciences, Datun Road A20, Beijing, People's Republic of China

<sup>3</sup>CAS Key Laboratory of FAST, NAOC, Chinese Academy of Sciences, Beijing, China

<sup>4</sup>University of Chinese Academy of Sciences, Beijing, People's Republic of China

<sup>5</sup>Indian Institute of Space Science and Technology, Thiruvananthapuram, Kerala 695 547, India

<sup>6</sup>NAOC-UKZN Computational Astrophysics Centre (NUCAC), University of KwaZulu-Natal, Durban 4000, South Africa

<sup>7</sup>Department of Physics, National Sun Yat-Sen University, No. 70, Lien-Hai Road, Kaohsiung City 80424, Taiwan, R.O.C.

<sup>8</sup>Center of Astronomy and Gravitation, National Taiwan Normal University, Taipei 116, Taiwan

<sup>9</sup>Jodrell Bank Centre for Astrophysics, School of Physics and Astronomy, University of Manchester, Oxford Road, Manchester, M13 9PL, UK

<sup>10</sup>Physikalisches Institut, University of Cologne, Zülpicher Str. 77, D-50937 Köln, Germany

<sup>11</sup>Key Laboratory of Radio Astronomy and Technology, Chinese Academy of Sciences, A20 Datun Road, Datun Road A20, Beijing, People's Republic of China

<sup>12</sup>Max-Plank-Institut für Radioastronomie, Auf dem Hügel 69, D-53121 Bonn, Germany

<sup>13</sup>Academia Sinica Institute of Astronomy and Astrophysics, No. 1, Sec. 4, Roosevelt Road, Taipei 10617, Taiwan

<sup>14</sup>Kavli Institute for Astronomy and Astrophysics, Peking University, 5 Yiheyuan Road, Haidian District, Beijing 100871, China

<sup>15</sup>Department of Astronomy, School of Physics, Peking University, Beijing 100871, People's Republic of China

<sup>16</sup>National Astronomical Observatory of Japan, National Institutes of Natural Sciences, 2-21-1 Osawa, Mitaka, Tokyo 181-8588, Japan

<sup>17</sup>Astronomical Science Program, The Graduate University for Advanced Studies, SOKENDAI, 2-21-1 Osawa, Mitaka, Tokyo 181-8588, Japan

<sup>18</sup>Vietnam National Space Center, Vietnam Academy of Science and Technology, 18 Hoang Quoc Viet, Hanoi, Vietnam

<sup>19</sup>Cardiff Hub for Astrophysics Research & Technology, School of Physics & Astronomy, Cardiff University, Queens Buildings, The Parade, Cardiff CF24 3AA, UK

<sup>20</sup>National Astronomical Research Institute of Thailand (NARIT), Sirindhorn AstroPark, 260 Moo 4, T. Donkaew, A. Maerim, Chiangmai 50180, Thailand

<sup>21</sup>Gemini Observatory/NSF's NOIRLab, 670 N. A'ohōkū Place, Hilo, HI 96720, USA

<sup>22</sup>Korea Astronomy and Space Science Institute, 776 Daedeokdae-ro, Yuseong-gu, Daejeon 34055, Republic of Korea

<sup>23</sup>University of Science and Technology, Korea (UST), 217 Gajeong-ro, Yuseong-gu, Daejeon 34113, Republic of Korea

<sup>24</sup>Institute of Astronomy, Department of Physics, National Tsing Hua University, Hsinchu 30013, Taiwan

<sup>25</sup>Armagh Observatory and Planetarium, College Hill, Armagh, BT61 9DB, United Kingdom

<sup>26</sup>Department of Earth Science Education, Seoul National University, 1 Gwanak-ro, Gwanak-gu, Seoul 08826, Republic of Korea

<sup>27</sup>SNU Astronomy Research Center, Seoul National University, 1 Gwanak-ro, Gwanak-gu, Seoul 08826, Republic of Korea

<sup>28</sup>Institute for Frontiers in Astronomy and Astrophysics, Beijing Normal University, Beijing 102206, People's Republic of China

<sup>29</sup>School of Physical Sciences, The Open University, Walton Hall, Milton Keynes, MK7 6AA, UK

<sup>30</sup>RAL Space, STFC Rutherford Appleton Laboratory, Chilton, Didcot, Oxfordshire, OX11 0QX, UK

<sup>31</sup>Korea Astronomy and Space Science Institute, 776 Daedeokdae-ro, Yuseong-gu, Daejeon 34055, Republic of Korea

<sup>32</sup>Shanghai Astronomical Observatory, Chinese Academy of Sciences, 80 Nandan Road, Shanghai 200030, People's Republic of China

<sup>33</sup>School of Physics and Astronomy, Yunnan University, Kunming, 650091, People's Republic of China

<sup>34</sup>Departamento de Astronomía, Universidad de Chile, Las Condes, 7591245 Santiago, Chile

Corresponding author: Hong-Li Liu, Zhiyuan Ren, Anandmayee Tej

hongliliu2012@gmail.com, jeremyrzy@gmail.com, tej@iist.ac.in

<sup>35</sup>Indian Institute of Science Education and Research (IISER) Tirupati, Rami Reddy Nagar, Karakambadi Road, Mangalam (P.O.), Tirupati 517507, India

## ABSTRACT

Filaments are believed to play a key role in high-mass star formation. We present a systematic study of the filaments and their hosting clumps in the G35 molecular complex using JCMT SCUBA-2 850  $\mu\text{m}$  continuum data. We identified five clouds in the complex and 91 filaments within them, some of which form 10 hub-filament systems (HFSs), each with at least 3 hub-composing filaments. We also compiled a catalogue of 350 dense clumps, 183 of which are associated with the filaments. We investigated the physical properties of the filaments and clumps, such as mass, density, and size, and their relation to star formation. We find that the global mass-length trend of the filaments is consistent with a turbulent origin, while the hub-composing filaments of high line masses ( $m_l > 230 \text{ M}_\odot \text{ pc}^{-1}$ ) in HFSs deviate from this relation, possibly due to feedback from massive star formation. We also find that the most massive and densest clumps ( $R > 0.2 \text{ pc}$ ,  $M > 35 \text{ M}_\odot$ ,  $\Sigma > 0.05 \text{ g cm}^{-2}$ ) are located in the filaments and in the hubs of HFS with the latter bearing a higher probability of occurrence of high-mass star-forming signatures, highlighting the preferential sites of HFSs for high-mass star formation. We do not find significant variation in the clump mass surface density across different evolutionary environments of the clouds, which may reflect the balance between mass accretion and stellar feedback.

**Keywords:** Star formation; Star forming regions; Molecular Clouds; Interstellar filaments; Molecular gas; Dust continuum emission

## 1. INTRODUCTION

High-mass stars ( $M > 8 \text{ M}_\odot$ ) significantly contribute to the energy and momentum of galaxies through their radiation, stellar winds, massive outflows, expanding HII regions, and supernova explosions (Zinnecker & Yorke 2007; Motte et al. 2018). Despite their importance, the formation process of these stars remains less understood than that of their low-mass counterparts, primarily due to their short lifetime scales, far distances, intense accretion processes and significant feedback effects.

Observational studies have revealed the ubiquity of filamentary structures in the Milky Way (e.g., André et al. 2010; Molinari et al. 2010; Kumar et al. 2020; Schisano et al. 2020; Zavagno et al. 2023, and references therein). These studies have also highlighted a strong correlation between star formation and filamentary molecular clouds (e.g., André et al. 2014; Lu et al. 2014, 2018; Liu et al. 2020, 2022). Intersecting filaments create distinct web structures, known as hub-filament systems (HFSs), representing a unique class of filaments in star formation, particularly for high-mass stars (e.g., Myers 2009; Liu et al. 2012b; Wang et al. 2016; Kumar et al. 2020; Zhou et al. 2022; Liu et al. 2023). In the context of HFSs, the central node is referred to as the hub, while the individual filaments associated with it are termed hub-composing filaments.

Recent studies of HFSs (e.g., Liu et al. 2012a; Peretto et al. 2013, 2014; Yuan et al. 2018; Liu et al. 2019;

Ren et al. 2021; Sanhueza et al. 2021; Saha et al. 2022; Xu et al. 2023; He et al. 2023; Yang et al. 2023b; Pan et al. 2024) have invoked the latest high-mass star formation models, such as Global Hierarchical Collapse (GHC, Vázquez-Semadeni et al. 2019) and Inertial Inflow (I2, Padoan et al. 2020) to understand star formation in these systems. In such models, filamentary structures are predicted to undergo self-growth through radial accretion from their surrounding environment and supply the formed clumps or cores through longitudinal accretion. Therefore, investigating how the physical properties (e.g., mass, density, size) of these hierarchical density structures evolve with time is helpful to understanding the complete picture of star formation, especially for high-mass star formation. To this end, conducting observational studies of large samples of filaments and embedded dense structures at different stages of evolution become the focus of this study.

The structure of the paper is as follows: Sections 2 and 3 describe the targeted region, and observations, respectively. Section 4 presents the results and analysis, focusing on distance measurement, identification of structures, and derivation of relevant physical parameters. Section 5 discusses the star formation scenario in the complex investigated. Specifically, Section 5.1 delves into the fragmentation of filaments; Section 5.2 discusses the role of HFS clouds in massive star formation; Section 5.3 explores the evolution of clump density over time. Section 6 gives the summary and conclusion.

## 2. PRESENTATION OF THE TARGETED REGION

The G35 molecular complex is selected as the target region investigated here due to the presence of many filamentary structures at different evolutionary stages. The target region, centered at  $\alpha_{2000} = 18^{\text{h}}56^{\text{m}}28^{\text{s}}.16$ ,  $\delta_{2000} = 2^{\circ}14'25.''71$  ( $l = 35.499^{\circ}$ ,  $b = -0.097^{\circ}$ ), with an approximate radius of  $0.41^{\circ}$ , covers five individual clouds which correspond to different systemic velocities (see Section 4.1) and thus are designated as Clouds 1, 2, 3, 4, and 5 (see Fig. 1).

Cloud 1, Cloud 2 and Cloud 3 harbour infrared dark clouds (IRDCs). Six IRDCs (i.e., G35.39, G35.60 and G35.69 in Cloud 1, G35.41 and G35.54 in Cloud 2, G35.46 in Cloud 3), as candidate sites for high-mass star formation, were cataloged by Peretto & Fuller (2009). One of them, G35.39, located at  $\sim 2.9$  kpc (Simon et al. 2006), is a well-known star-forming ridge (Nguyen Luong et al. 2011; Motte et al. 2018) that has been extensively studied for its fragmentation, kinematics, dust polarization, and/or chemical properties (e.g., Sanhueza et al. 2012; Jiménez-Serra et al. 2014; Barnes et al. 2016; Sokolov et al. 2017; Liu et al. 2018; Barnes et al. 2021; Xie et al. 2021). In comparison, IRDC G35.41, exhibiting a bipolar bubble feature in the  $8\mu\text{m}$  image, is at a more evolved stage. The elongated IRDC G35.46 in Cloud 3, together with IRDC G35.41 and G35.54 in Cloud 2, and IRDC G35.60 and G35.69 in Cloud 1, are less well studied. In addition, the entire targeted region contains 37 ATLASGAL clumps (Urquhart et al. 2014a, 2018), about a quarter of which are located within the IRDCs.

The other molecular cloud complex in the northern region is Cloud 4 centred at  $\alpha_{2000} = 18^{\text{h}}56^{\text{m}}09^{\text{s}}.55$ ,  $\delta_{2000} = 2^{\circ}22'58.''99$ . This cloud, approximately  $0.2^{\circ}$  in radius (corresponding to a physical scale of  $\sim 10$  pc), exhibits extended morphology and is bright in the IR. Its eastern side is connected to a large IR bubble (i.e., G356521-0002439; Jayasinghe et al. 2019), denoted as the largest magenta circle. The entire cloud encompasses several smaller IR bubbles surrounding HII regions (Anderson et al. 2014), also marked with colored circles in Fig. 1. Three massive young stellar objects (MYSOs) and a WISE Green Object (WGO) G35.417-0.285 denoted in Fig. 1 can be found within Cloud 4 (Urquhart et al. 2008; Zhang et al. 2023). Furthermore, the Spitzer/IRAC Candidate young stellar object (YSO) Catalog for the Inner Galactic Midplane project (SPICY; Kuhn et al. 2021) has revealed a group of over 300 young YSO candidates, which are not shown here. Fourteen HII regions and six methanol masers at 6.7 GHz, both suggestive of high-mass star formation, have been observed in this large area containing the four primary clouds by

the Global View on Star Formation (GLOSTAR) survey with high-resolution VLA observations (Brunthaler et al. 2021; Nguyen et al. 2022; Dzib et al. 2023; Yang et al. 2023a).

Cloud 5 appears to harbour four bubbles identified as (candidate) HII regions (Anderson et al. 2014), one of which is associated with a methanol maser at 6.7 GHz. In this cloud along with Cloud 3, most of the region show relatively weak cold dust emission as traced by  $850\mu\text{m}$  radiation (see Sect. 4.2, and Fig. 2), which is similar to those low intensity contrast observed in  $8\mu\text{m}$  emission.

In summary, the entire target complex encompasses active high-mass star-forming clouds at various evolutionary phases, from quiescent IRDCs to evolved bubbles or HII regions.

## 3. OBSERVATIONS

### 3.1. SCUBA-2 $850\mu\text{m}$ Continuum Data

The G35 molecular complex was observed as part of the  $850\mu\text{m}$  dust continuum survey, called "A Lei of the Habitat and Assembly of Infrared Dark Clouds" (ALOHA IRDCs<sup>1</sup>) under a JCMT large program (Proj. ID. M20AL021; Ren et al. 2024, in prep.). The survey was performed using the SCUBA-2 rotating Pong900 pattern. The entire observing coverage of the target region, which is delineated as the outermost white contour in Fig. 1, consists of three fields of view (FoV), each observed with a radius of approximately  $15'$  at a scan spacing of  $30''$ . The entire target was observed with an integration time of 22 hours. Raw data were reduced using the *Starlink*<sup>2</sup> software, yielding a final reduced  $850\mu\text{m}$  image and a rms noise map. The noise level varies between 5 to  $75\text{ mJy beam}^{-1}$  from the inner region to the edge, and the global *rms* distribution appears, except for the regions approaching the edge, reasonably uniform at an approximate  $10\text{ mJy beam}^{-1}$  (see Fig. A1). The beam size of the reduced data is  $14.1''$  and the adopted pixel size for mapping is  $4''$ . The flux calibration uncertainty of SCUBA-2 at  $850\mu\text{m}$  is  $\sim 6\%$  (Mairs et al. 2021). Note that ground-based (sub)millimeter continuum observations usually suffer from missing flux at large scales (e.g., Jiao et al. 2022) in the data-processing stage, since a filter has to be applied to remove large-scale atmospheric noises. Following the SCUBA-2 Data Reduction Cookbook<sup>3</sup>, a default filter scale of  $480''$  was adopted. This translates to scales  $> 4.5$  pc at the dis-

<sup>1</sup> <https://www.eaoobservatory.org/jcmt/science/large-programs/aloha-irdcs/>

<sup>2</sup> <https://starlink.eao.hawaii.edu/starlink>

<sup>3</sup> <http://starlink.eao.hawaii.edu/devdocs/sc21.htm>

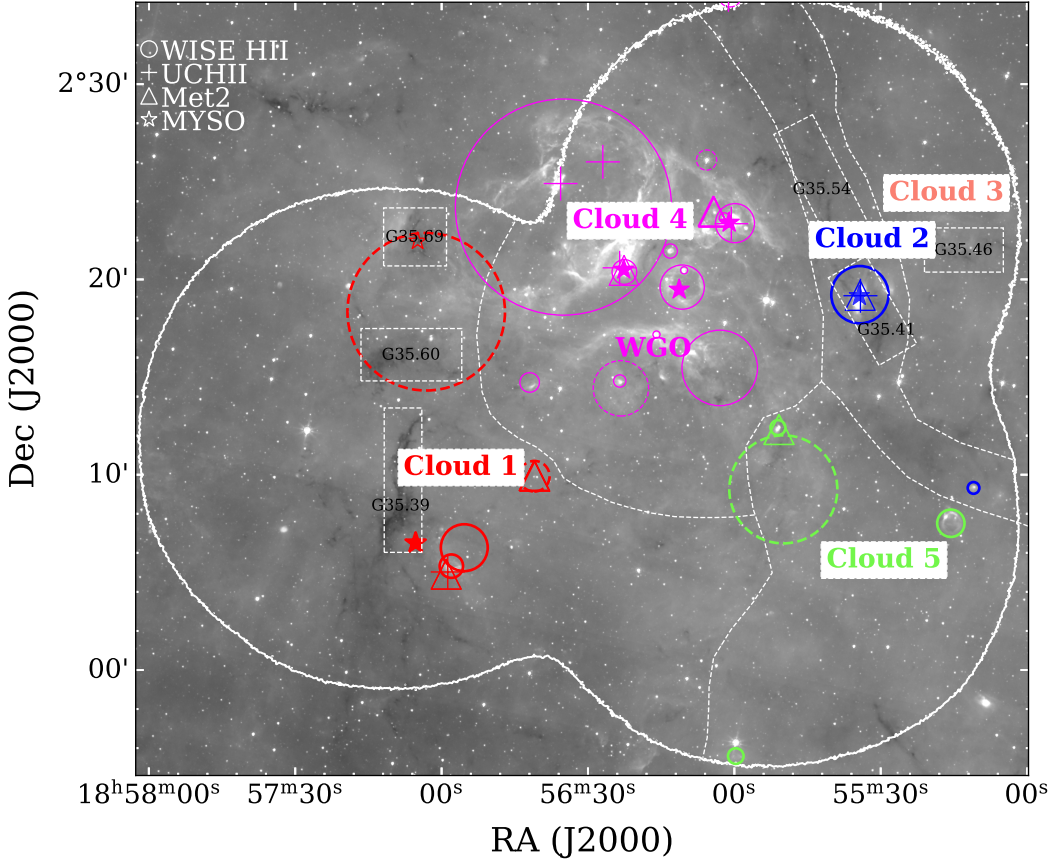


**Figure 1.** Overview of the G35 complex in *Spitzer* 8  $\mu\text{m}$  emission. The solid and dashed circles correspond to the HII regions and candidates from the WISE catalogue by Anderson et al. (2014), respectively, with the symbol size representing the actual size of those objects. The plus symbols identify the positions of ultracompact HII regions from different literature catalogs (Bronfman et al. 1996; Hou & Han 2014; Hu et al. 2016; Kalcheva et al. 2018; Ouyang et al. 2019). The class II methanol masers retrieved from Ladeyschikov et al. (2019); Nguyen et al. (2022) are marked by open triangles. The solid stars identify the Red MSX MYSOs (Urquhart et al. 2011) while the open stars identify massive protostars (Li et al. 2018). Six dark clouds mentioned in Sect. 2 with their names are marked using white dashed rectangles. The white dashed lines approximately delineate boundaries of different clouds. The region of 850  $\mu\text{m}$  continuum for final analysis is limited within a white solid contour of the 20 mJy beam $^{-1}$  rms level.

tance of the G35 complex and thus is assumed not to significantly affect the smaller-scale dense structures of filaments (i.e.,  $\sim 0.5$  pc in typical width) and clumps investigated here (see also Schuller et al. 2009; Li et al. 2016; Urquhart et al. 2018).

### 3.2. Archival Data

We used multi-wavelength infrared images from the *Spitzer* and *Herschel* telescopes to study the dust properties of the cloud complex. These include *Spitzer* 8  $\mu\text{m}$  data from the GLIMPSE (Benjamin et al. 2003) survey, and *Herschel* data (160  $\mu\text{m}$  and 250  $\mu\text{m}$ ) from the Hi-GAL survey (Molinari et al. 2010). The angular resolutions at 8  $\mu\text{m}$ , 160  $\mu\text{m}$  and 250  $\mu\text{m}$  are approximately 2'', 12'', and 18'', respectively.

Molecular line observations of  $^{13}\text{CO}$  ( $J=1-0$ ) were obtained as part of Boston University–Five College Radio

Astronomy Observatory Galactic Ring Survey (GRS; Jackson et al. 2006) using the FCRAO 14 m telescope. The data has a rms sensitivity  $< 0.4$  K, a spectral resolution of 0.21 km s $^{-1}$ , and an angular resolution of 46''.

## 4. RESULTS

### 4.1. Distance determination

Except for the well-studied IRDC G35.39-0.33 located at 2.9 kpc (Simon et al. 2006; Liu et al. 2018), the distances for the remaining clouds in the region targeted here have not yet been determined. Fig. A2 displays the average spectra of  $^{13}\text{CO}$  over the entire target region. Five strong velocity components are seen in the  $^{13}\text{CO}$  line with velocity ranges [5, 20], [20, 40], [40, 50], [50, 65], and [70, 85] km s $^{-1}$ . With the assumption that cold dust emission comes from the same region as molecular gas, the velocity-integrated intensity

of  $^{13}\text{CO}$  of these velocity components can be used to investigate their spatial association with the  $850\,\mu\text{m}$  dust continuum. Based on this, we exclude the second velocity component from further analysis. That component is most likely a non-associated component, as the line and dust emission do not spatially match well. The integrated intensity of  $^{13}\text{CO}$  of four velocity components is presented in Fig. A3, showing a good association between gas and dust emission, excluding the second component. Note that there are overlapping distributions of relatively weak gas emission from different velocity components, such as the overlap between Cloud 5 and Cloud 2 (Fig. A3). This indicates that the observed dust emission is likely contaminated by the line of sight contamination of clouds at different distances.

Based on the above-mentioned spatial association in  $850\,\mu\text{m}$  dust continuum emission, five primary clouds shown in Fig. 1 have been approximately delineated. The separation between Cloud 1 and Cloud 4 is roughly based on the appearance of relatively dark and bright  $8\,\mu\text{m}$  features and hence, is to be considered with caution for guidance purpose solely. The associated four velocity components are considered to derive kinematic distances using the latest distance calculation tool, the "Parallax-Based Distance Calculator V2" (Reid et al. 2016, 2019), leading to distance estimates of 2.1 kpc (i.e., Cloud 5), 2.5 kpc (i.e., Cloud 1, Cloud 3 and Cloud 4), and 5.1 kpc (i.e., Cloud 2), all with an uncertainty of  $\sim 10\%$ . The distance estimates of Clouds 1, 3, and 4 are very close to that of IRDC 035.39-0.33. Therefore, they are assumed to be in the same complex, and are treated for consistency to have the same distance as that of the well-studied IRDC G35.39 (i.e., 2.9 kpc).

#### 4.2. Dust Continuum Emission

Fig. 2 shows the  $850\,\mu\text{m}$  dust emission image. As an excellent tracer of column density, the continuum peak emission matches the  $8\,\mu\text{m}$  dark lanes. Overall, Cloud 1, 2, and 4 account for the vast majority of the continuum emission, while the continuum emission from Cloud 3 and 5 are relatively weak.

#### 4.3. Identification of Filaments and Clumps

##### 4.3.1. Filament extraction

Filamentary structures were extracted from the  $850\,\mu\text{m}$  continuum image, using the algorithm FILFINDER (Koch & Rosolowsky 2015). We set the minimum threshold (`glob_thresh`) to five times the  $rms$  ( $\sim 50\,\text{mJy beam}^{-1}$ ), the minimum structure area (`size_thresh`) to 18 pixels (twice the beam area), and the hole-filling size (`fill_hole_size`) to 150 pixels. Here, the first two parameters were determined to im-

prove the robustness of the identified skeletons, while the third one was to avoid the presence of holes within a skeleton. During our post selection, we discarded structures at the image edges and those in the areas with  $rms$  greater than  $20\,\text{mJy beam}^{-1}$ . We also removed structures with a major axis (length) shorter than 3 beam sizes, following Suri et al. (2019). As a result, we obtained 91 skeletons representing individual filaments, some of which form HFSs (see Sect. 1 for their definition).

The identified filaments are shown in Fig. 4 and A4. Overall, Cloud 1 is found to contain 17 individual filaments and 3 HFSs (i.e., each HFSs corresponding to a web of at least three individual filaments<sup>4</sup>). Cloud 2 has 7 individual filaments and 2 HFSs. Cloud 3 hosts 4 individual filaments and 1 HFSs. Cloud 4 consists of 15 individual filaments and 4 HFSs. Cloud 5 shows 3 individual filaments. Note that there could be a few filaments that were not identified due to our adopted strict criteria (e.g., 5  $rms$  as the minimum threshold) for a robustness. This incompleteness caused by a few unidentified filaments, however, does not affect our following analysis. In addition, we find that all HFSs identified here are included in the catalogue of filaments by Li et al. (2016) using ATLASGAL  $870\,\mu\text{m}$  dust emission observed at a similar angular resolution but with a lower sensitivity (i.e.,  $50\text{--}70\,\text{mJy beam}^{-1}$ ). In all, except for more detection of fainter structures in our observations, the dense filament detection has a good correspondence between the two different observations.

##### 4.3.2. Clump extraction

We created the clump catalog using the source extraction algorithm SExtractor (Bertin & Arnouts 1996), an aperture photometry tool widely used to detect compact objects (e.g., Contreras et al. 2013; Urquhart et al. 2014a). The  $850\,\mu\text{m}$  map and the noise  $rms$  map serve as input to the SExtractor, with a detection threshold of five times the local  $rms$ . The total flux of each object is measured from the  $850\,\mu\text{m}$  map adopting the "Bijection" paradigm (see Fig. 4 of Rosolowsky et al. 2008) using ellipse aperture photometry. The final uncertainty in the measured flux arises from the combination in quadrature of the local noise with the systematic flux uncertainty (e.g., Thompson et al. 2006; Contreras et al. 2013). As a result, 350 compact density structures are extracted, which are hereafter called clumps. Note

<sup>4</sup> The definition of the HFS structure is required to have at least three hub-composing filaments. This would allow to get rule out of the possibility of a single filament appearing as an HFS structure due to the kink by external pressures instead of the merge process by several filaments.

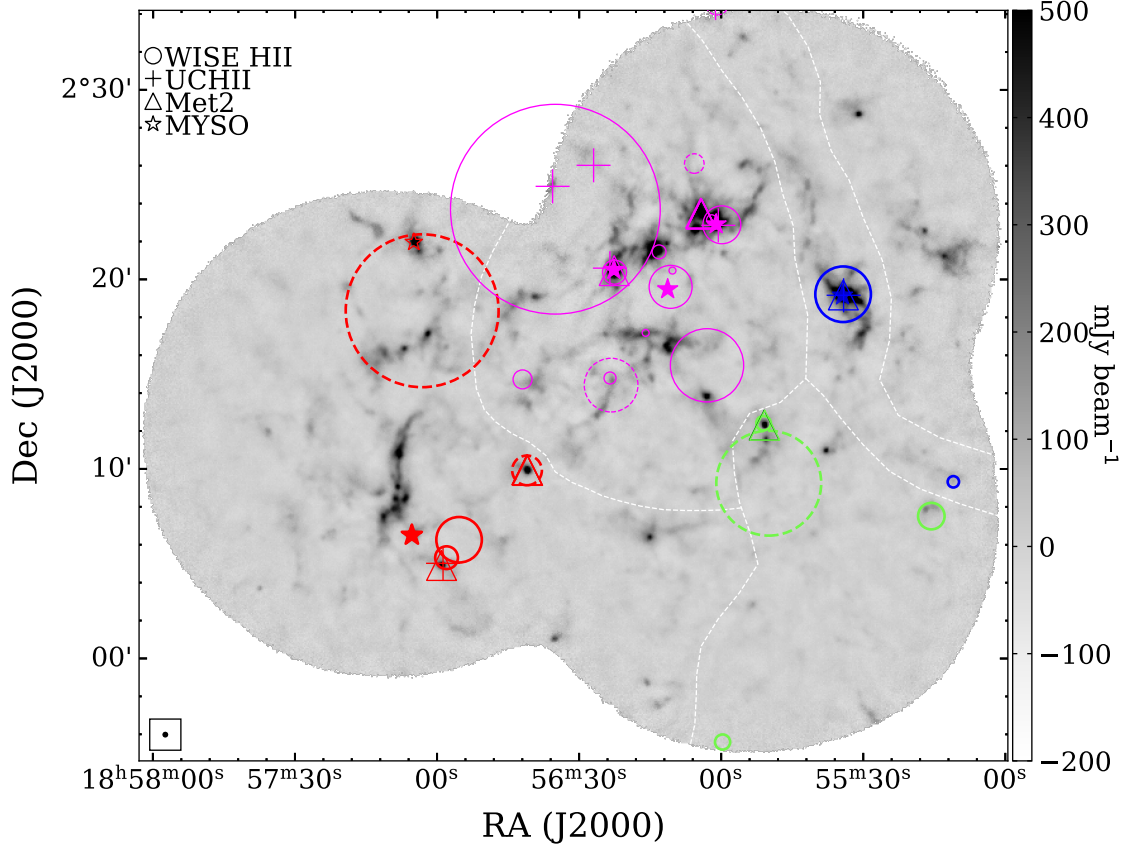


**Figure 2.** Dust emission maps as traced by 850  $\mu\text{m}$  continuum for the G35 complex. All symbols are the same as those in Fig. 1. The beam size of 850  $\mu\text{m}$  observations is displayed at the bottom left corner.

that a few clumps appear not be extracted, for example in the northermost of the observing region, which could be either due to the low intensity contrast (i.e.,  $< 5$  signal-to-noise ratio) with the local rms level or due to their sizes smaller than the beam size accessible to 850  $\mu\text{m}$  observations. The latter possibility could be due to potential artefacts of continuum map, and thus those associated sources are not considered in our clump catalogue analysis.

It is necessary to investigate the flux completeness level of our catalogued clumps given the limitation of the observing sensitivity. To this end, we randomly inserted simulated clumps into the 850  $\mu\text{m}$  noise map (e.g., Contreras et al. 2013; Yang et al. 2023a). We simulated 5000 clumps for each FoV analysis, with the input flux densities ranging from 1 to 100 mJy beam $^{-1}$  (for reference, 1 rms=10 mJy beam $^{-1}$  overall). Here, three individual FoVs (see Fig. A1), each representing different observations, and their sum as the entire FoV were considered, each having slightly different rms distributions. Subsequently, the same Sextractor algorithm was applied to the simulated map. Fig. 3 illustrates the detection fraction of the simulated clumps as a function of peak flux

density. As a result, the 95% completeness levels are  $\sim 6 \text{ rms}$  for FoVs 1 and 3,  $\sim 7 \text{ rms}$  for FoV 2, and approximately  $\sim 6.5 \text{ rms}$  ( $N_{\text{H}_2} \approx 4.3 \times 10^{21} \text{ cm}^{-2}$ ) for the entire FoV. This suggests that the slight difference in different FoVs does not significantly affect the detection of clumps. In addition, the 5 rms level adopted in practice in our clump extraction corresponds to a global flux completeness level of  $\sim 90\%$  for the entire FoV.

The measured parameters of the identified 350 clumps are listed in Table B2, including the position, peak flux and position angle. Fig. 4 shows the identified clumps overlaid on the 850  $\mu\text{m}$  continuum. The majority of the detected clumps are located in Cloud 1 and Cloud 4, i.e., 141 and 123 sources, respectively. The number of extracted clumps is similar in Cloud 2 and Cloud 5, with 33 and 36, respectively. The remaining 18 clumps are distributed in Cloud 3. The identified clumps include all 37 ATLASGAL clumps identified by Urquhart et al. (2014a) using the same SExtractor algorithm. From the present analysis, we infer that both high sensitivity and angular resolution of the ALOHA dataset allows us to detect additional hundreds of clumps located in extended diffuse background. Furthermore, the

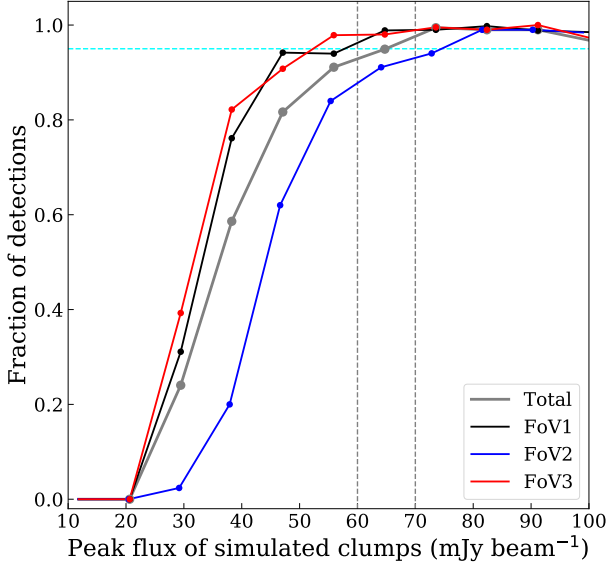


**Figure 3.** Detection fraction of simulated sources as a function of peak flux density. Different curves correspond to different FoV analysis, including FoVs 1, 2 and 3 and their sum as the total FoV. The dashed cyan line indicates the 95% detection fraction/flux completeness level. Two dashed gray lines (from left to right) show the  $6\text{rms}$  and  $7\text{rms}$  levels ( $1\text{rms} = 10\text{mJy beam}^{-1}$ ), respectively.

measured fluxes of the ATLASGAL clumps from previous  $870\mu\text{m}$  and our  $850\mu\text{m}$  observations are comparable within quoted uncertainties (see Appendix A.4 and Fig. A6).

#### 4.4. Physical Properties of Filaments and Clumps.

##### 4.4.1. Width and flux of filaments

Although the FILFINDER algorithm gives the positions and lengths of filament skeletons, the other resulting parameters (e.g., filament width) may be biased. This is because the averaged radial intensity profiles across the filamentary skeletons are not always characterized by a Gaussian/Plummer-like function, which is usually applied to derive the filament width. This situation becomes severe for the hub-composing filaments in HFSs. For the individual filaments, we can derive the averaged radial intensity profile of each skeleton using FILFINDER and an example of the Gaussian profile is shown in Fig. 5. However, in HFSs, some hub-composing filaments display significantly different irregular profiles. In some cases, limitations in the number of sample points (i.e., short filaments or those between multiple connections such as in HFSs) may also prevent obtaining accurate profiles, leading to a poor determination of the filament width. To account for the above mentioned inaccuracies, for all hub-composing filaments in HFSs, we adopt a common filament average width.

For the total flux at  $850\mu\text{m}$  within each filament, we integrate all  $850\mu\text{m}$  intensity within a curved rectangle defined by the filament width and its length, which was assumed to represent a 2D projection of each filament. During the measurement of total flux, we did not perform large-scale background subtraction. This is because such subtraction have been carried out during our data-processing stage (as detailed in Sect. 3.1). To address flux uncertainties arising from a fixed filament width, we measured the total flux by varying each filament's width by  $\pm 1/2$  times, which will be discussed in Sect. 4.4.2. Note that we did not partition the hub flux into specific filaments within the HFSs. Instead, we incorporated the hub flux into the overall flux measurement for each filament composing the hub. The total integrated flux at  $850\mu\text{m}$  for each filament are listed in Col. 5 of Table B1.

##### 4.4.2. Dust temperature, mass, and related properties of both filaments and clumps

The mass of clumps and filaments was calculated following the gray-body radiation model (e.g., Hildebrand 1983; Liu et al. 2021):

$$M = \frac{D^2 S_\nu R_{gd}}{B_\nu(T_{\text{dust}}) \kappa_\nu}, \quad (1)$$

where  $D$  is the source distance,  $S_\nu$  is the integrated flux of  $850\mu\text{m}$  emission,  $R_{gd}$  is the gas-to-dust mass ratio taken as  $R=100$ ,  $B_\nu$  is the Planck function for a dust temperature  $T_{\text{dust}}$ , and  $\kappa_\nu$  is the dust absorption coefficient taken as  $\kappa_{850\mu\text{m}} = 1.85\text{ cm}^2\text{ g}^{-1}$ . This value was derived from the interpolation of the values listed in Col. 5 of Table 1 in Ossenkopf & Henning (1994), called the OH5 model (Shirley et al. 2011). Here,  $T_{\text{dust}}$  was estimated from the  $18''$ -resolution temperature map (see Fig. A4 in Appendix), which presents a range of 14 K to 48 K with a median value of 18 K. It was created using the  $160\mu\text{m}$  and  $250\mu\text{m}$  images from the Hi-GAL survey, where the ratio of the two images serves as a temperature probe (see details in Peretto et al. 2016; Pan et al. 2023).

We estimated the average  $\text{H}_2$  column density ( $N_{\text{H}_2}$ ) as follows:

$$N_{\text{H}_2} = \frac{M}{A \mu_g m_H}, \quad (2)$$

where  $A$  is the measured area of density structures (clumps or filaments),  $\mu_g$  is the molecular weight per hydrogen molecule taken as 2.8 (Kauffmann et al. 2008), and  $m_H$  is the mass of an atomic hydrogen.

For clumps only, their mass surface densities ( $\Sigma_{\text{clump}}$ ) were computed using the following equation:

$$\Sigma_{\text{clump}} = \frac{M_{\text{clump}}}{\pi R_{\text{clump}}^2}, \quad (3)$$

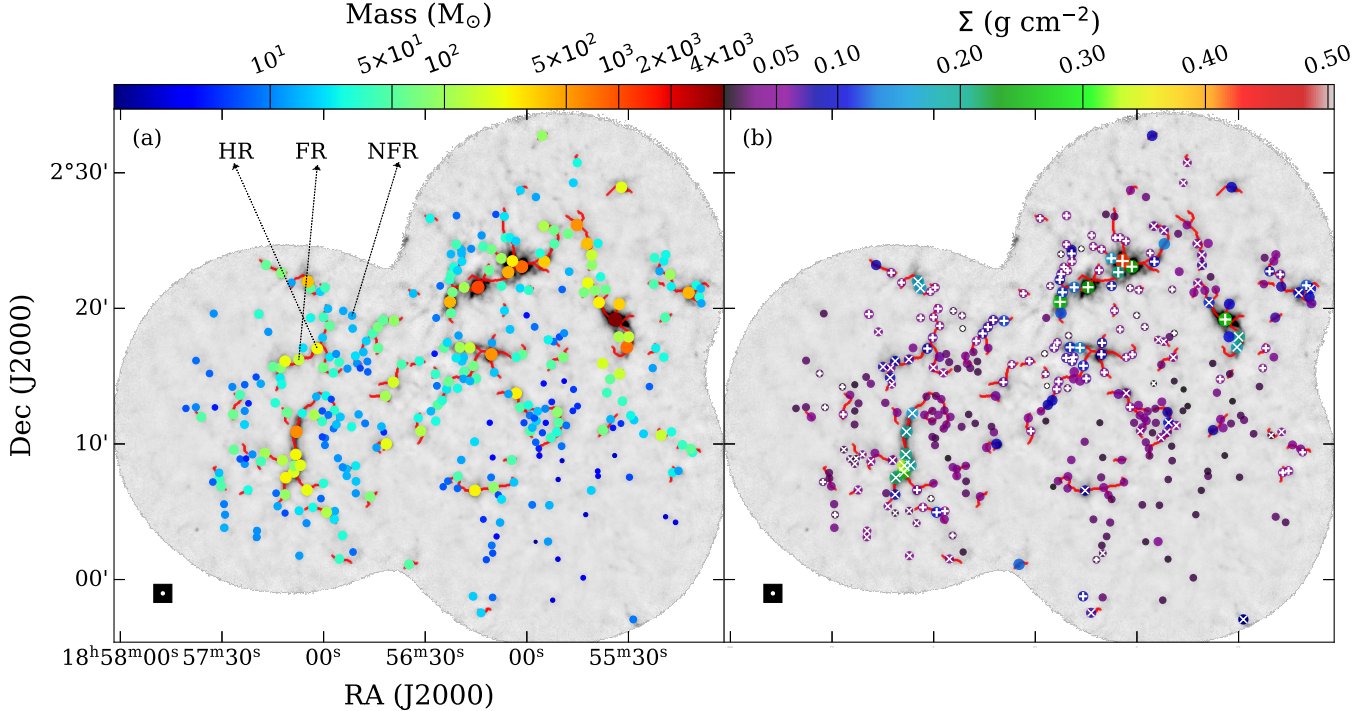


**Figure 4.** Spatial distributions of filaments (red curves) and clumps (colored dots). In panel (a), the color of the dot corresponds to the value of the clump mass while in panel (b), it corresponds to the value of the mass surface density. In both panels, the white plus and cross symbols indicate IR-bright, and IR-dark clumps inferred from *Spitzer* 8  $\mu\text{m}$  image, respectively. The examples of HR clumps, FR clumps, and NFR clumps mentioned in Section 5.1 are marked with arrows.

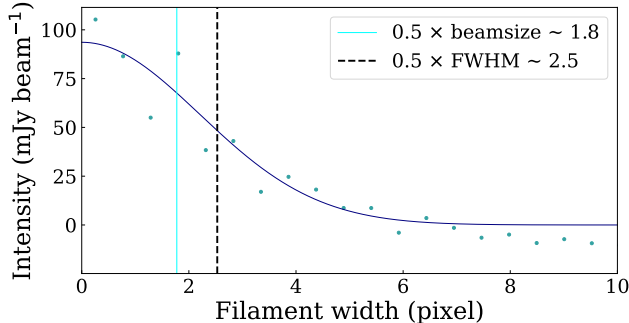


**Figure 5.** An example of the averaged radial profile from the **FILFINDER**. The solid dark blue line shows the profile fitted with a Gaussian curve. Both  $0.5 \times$  beam size and  $0.5 \times$  FWHM are presented in the plot.

where  $M_{\text{clump}}$  and  $R_{\text{clump}}$  represent the mass and radius of clumps, respectively. The derived parameters for the filaments and clumps are tabulated in Table B1 and Table B2, respectively.

The uncertainties of these properties come from various aspects. We first consider a kinematic distance uncertainty of 10% which is directly linked to the uncertainties of length and width of the filaments or the radius of clumps. The dust opacity ( $\kappa_{\nu}$ ) at the same frequency can exhibit variations across different clouds, ranging from diffuse to dense environments. This vari-

ability is observed in studies such as those by Martin (2012), Roy (2013), and Webb (2017). Similarly, the gas-to-dust ratio ( $R_{gd}$ ) is also seen to vary. According to Sanhueza et al. (2017); Xu et al. (2024),  $\kappa_{\nu}$  may vary by approximately 28%, conservatively estimated from the OH5 model. Additionally,  $R_{gd}$  can deviate by 23% relative to a reference value of  $R_{gd} = 100$ . To account for uncertainties stemming from these sources, we assumed a uniform distribution between extreme values. Employing the Monte Carlo technique with 10,000 random samples, we calculated the standard deviation as the final uncertainty in related parameter calculations.

For clumps, mass uncertainties range from 43% to 47%, with a mean value of approximately 44%. The column/surface density uncertainties span 38% to 42%, with a mean value around 39%. In the case of filaments, the related uncertainties remain the same as for clumps. However, when accounting for potential variations in filament width (up to  $\pm 1/2$  times, see Sect. 4.4.1), total flux uncertainties for each filament range from 38% to 77%, resulting in higher mass uncertainties of 58% to 91% with a mean value of approximately 78%.

#### 4.4.3. Statistical results of physical properties

Fig. 6 shows the summary statistics of the physical properties of filaments and clumps. Fig. 6 (a) shows that

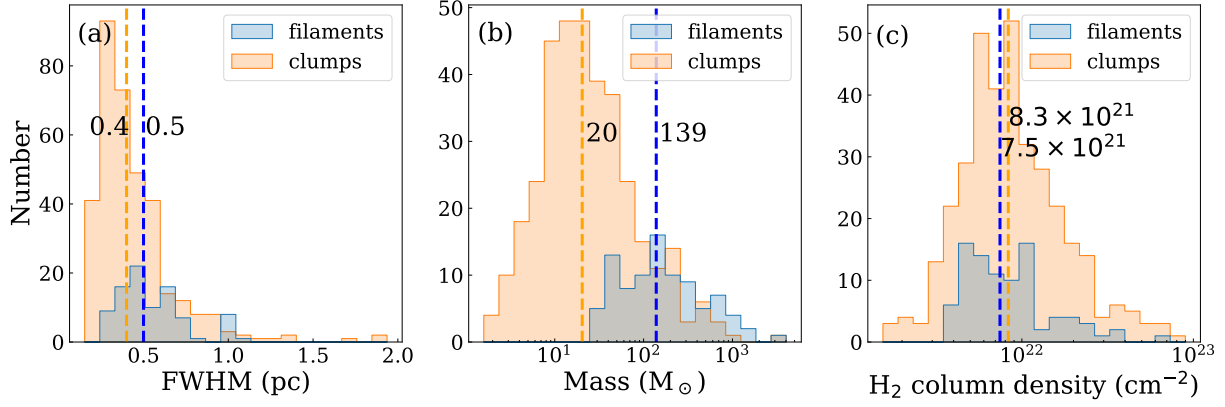


**Figure 6.** Distribution of parameters (i.e., FWHM, mass, column density) of filaments (blue) and clumps (orange). The corresponding median value is indicated with a vertical dashed line.

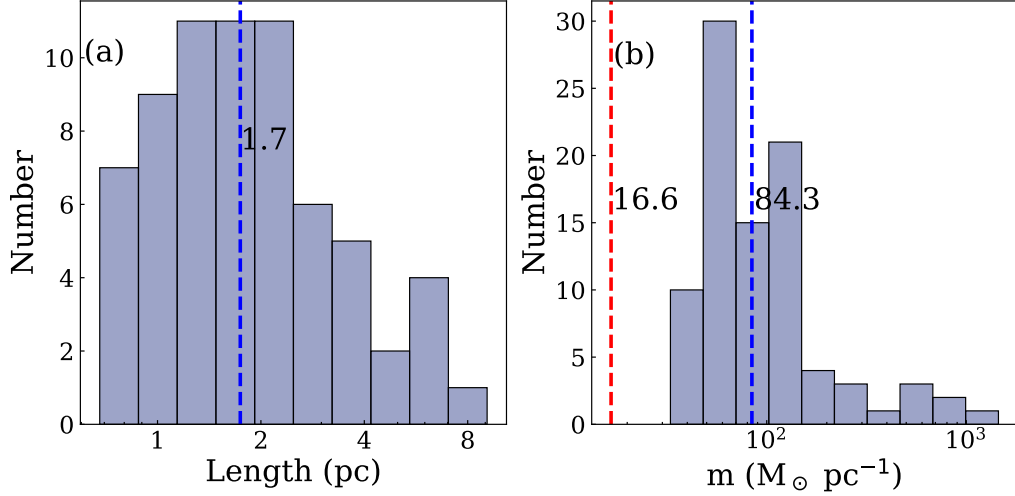


**Figure 7.** Length and line mass distributions of filaments. The vertical blue line in both panels presents the median value, while the red line in panel b gives a critical line mass of  $16.6 M_{\odot} \text{ pc}^{-1}$ .

widths of filaments have a median value of  $\sim 0.51$  pc. The width of filament, considered as one of their fundamental properties, is subject to debate (see reviews by André et al. 2014; Hacar et al. 2023; Pineda et al. 2023). In contrast, the size distribution of clumps is wider, ranging from  $\sim 0.25$  to 2 pc, with a median value of 0.37 pc slightly smaller than the filament width.

Fig. 6 (b) shows an evident difference between the distributions of the mass for filaments and clumps, with the peaks of the two types of samples clearly offset from each other. The filaments have masses of 26 to 2962  $M_{\odot}$  with a median value of 139  $M_{\odot}$ , while the clump masses range from 2 to 4023  $M_{\odot}$  with a median value of 20  $M_{\odot}$ .

Fig. 6 (c) displays the distributions of the averaged column density for filaments and clumps. The two distributions have a similar dynamical range, with a similar median value of  $\sim 8 \times 10^{21}$  cm<sup>-2</sup>.

Fig. 7 provides the distributions of the length and line mass  $m$  of filaments. The filament length ranges from 0.7 to 9.1 pc, with a median value of 1.7 pc. The line mass  $m$  is defined as the ratio of the mass to the length of a filament in a unit of  $M_{\odot} \text{ pc}^{-1}$ . Overall, the observed line masses fall within the range of the statistical results reported in previous Galactic surveys, as summarized in Table 2 of Hacar et al. (2023) and references therein.

The observed line mass, in conjunction with the critical one  $m_{crit}$ , is a standard criterion for assessing the stability of the filament.  $m_{crit}$  is  $16.6 M_{\odot} \text{ pc}^{-1}$  for an ideal isothermal cylindrical model (Ostriker 1964) at a kinematic temperature of 10 K. As a result, the observed line masses are greater than the theoretical value, indicating a dynamical state of being gravitationally bound. Furthermore, we investigated the turbulent contributions for the dense filaments using the NH<sub>3</sub>(1-1) data with a beam size  $\sim 32''$  from the RAMPS survey (Hogge

**Table 1.** Summary of correlation coefficients

	entire samples	hub-composing filaments
$\rho_{12}$	0.837	0.637
$\rho_{13}$	0.303	0.468
$\rho_{23}$	0.135	0.115
$\rho_{12,3}$	<b>0.844</b>	<b>0.664</b>

**Notes.** “1”, “2”, “3” correspond to mass, length and

distance, respectively. The notation  $\rho_{xy}$  indicates the Spearman’s rank correlation coefficient of each pairs, while  $\rho_{12,3}$  indicates the partial correlation coefficient (highlighted in bold).

(et al. 2018, and see Sect. A.5). Due to the low detection rates of the RAMPS survey across the entire G35 complex (see Fig. A7), we only report the typical values in the following. We find that IR-bright Cloud 4 exhibits larger linewidths ( $\sim 0.87 \text{ km s}^{-1}$ ) compared to the remaining relatively quiescent clouds ( $\sim 0.49 \text{ km s}^{-1}$  for Clouds 1, 2, 3, and 5). The critical line mass  $m_{\text{vir,crit}}$  including the contributions of the non-thermal motions (Fiege & Pudritz 2000), also called virial line mass, was calculated as follows:

$$m_{\text{vir,crit}} = \frac{2\sigma_v^2}{G} \quad (4)$$

where  $\sigma_v$  is the total velocity dispersion of the gas and  $G$  is the gravitational constant. Using the two typical linewidths estimated above in Eq. (4), we derived two critical line masses of  $352 \text{ M}_\odot \text{ pc}^{-1}$  for the IR-bright cloud and  $112 \text{ M}_\odot \text{ pc}^{-1}$  for the IR-quiet counterparts. The latter is comparable to the observed median line mass in Fig. 7, implying considerable turbulent contribution to the dynamical stability in early stages of filament evolution. However, in more evolved IR-bright environments, the turbulent contribution is observed to be higher by a factor of three, implying the potential role of external pressures in maintaining the dynamical stability of filaments.

#### 4.4.4. Mass-length diagram

Fig. 8 shows the mass-length diagram of filaments, including individual filaments (i.e., small solid circles) and hub-composing ones (i.e., plus symbols) within HFSs. We find the populations of individual filaments and hub-composing filaments to be differently distributed, with the latter forming a wider spread in length and mass.

In the above analysis, both parameters have distance dependence. To remove mutual dependence of mass and length on the distance, the first-order partial correlation test (e.g., Urquhart et al. 2018; Yang et al. 2018; Taniguchi et al. 2023) was adopted. The partial corre-

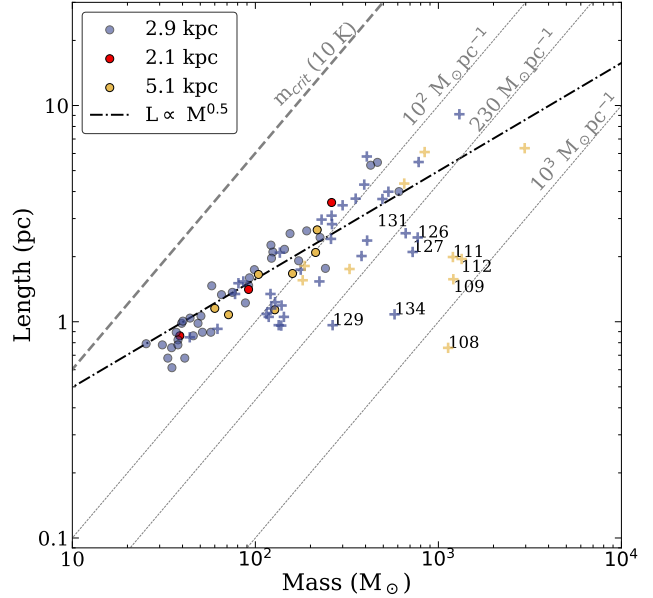


**Figure 8.** Mass-length diagram of individual filaments and hub-composing filaments within HFSs. The solid circles denote the individual filaments located at different distances, while the plus symbols mark the hub-composing filaments within HFSs. Numbers indicate hub-composing filaments characterized by notable deviations from the global trend (see text). The bold dash-dotted line presents the relation  $L \propto M^{0.5}$  described by the simple model of Hacar et al. (2023). The thick dashed line at the top of the diagram represents a typical critical line mass of  $16.6 \text{ M}_\odot \text{ pc}^{-1}$ , while the thick dashed-dotted line represents the global trend between mass and length. The light dashed lines represent different reference line masses.

lation coefficient,  $\rho_{12,3}$ , is as follows:

$$\rho_{12,3} = \frac{\rho_{12} - \rho_{13}\rho_{23}}{\sqrt{(1 - \rho_{13}^2)(1 - \rho_{23}^2)}} \quad (5)$$

Here, “1” and “2” denote the two dependent parameters (mass and length, respectively) that we prioritize, while “3” signifies the independent distance that may influence the aforementioned ones.  $\rho_{xy}$  (i.e.,  $\rho_{12}$ ,  $\rho_{13}$ ,  $\rho_{23}$ ) represents the Spearman’s rank correlation coefficient between pairs. Table 1 summarizes all of the correlation coefficients for the entire samples and hub-composing filaments alone. As shown in Table 1, the correlation between mass and length is already strong in the entire sample ( $\rho_{12,3} > 0.84$  with  $p$ -value  $\ll 0.001$ ), while the hub-composing ones show relatively weaker correlations ( $\rho_{12,3} \sim 0.66$  with  $p$ -value  $\ll 0.001$ ). These results suggest that the dispersion of the mass-length distribution can mostly be attributed to the presence of hub-composing filaments. Meanwhile, the consistency between the Spearman coefficient and the partial corre-

lation coefficient suggests that the effect of distance on the distribution of mass and length is negligible.

## 5. DISCUSSION

### 5.1. Implication of mass-length scaling of filaments

The mass-length diagram presented in Fig. 8 shows interesting trends. All the individual filaments (small solid circles) and most of the hub-composing filaments (plus symbols not numbered) are seen to approach a global trend (but with a somehow steeper slope), proposed by Hacar et al. (2023) as a power-law scaling relation of  $L \propto M^\alpha$  ( $\alpha = 0.5$ ). This scaling relation is similar to Larson's  $M \propto R^2$  (Larson 1981; Solomon et al. 1987; Heyer et al. 2009) and could be attributed to turbulent fragmentation from clouds to filaments (Tafalla & Hacar 2015; Smith et al. 2016; Hacar et al. 2023). In such a turbulent fragmentation scenario, filaments increase in mass and length as they undergo turbulence-dominated either longitudinal or radial accretion from their natal clouds. As the radial accretion progresses, the length could remain nearly steady, while the mass continues to increase, likely causing a slight deviation from the global scaling relation (e.g., Feng et al. 2024). This could account for the somewhat steeper trend observed in the global distribution of most filaments, compared to the proposed relation  $L \propto M^{0.5}$ .

Moreover, a number of the hub-composing filaments (numbered plus symbol) are seen to significantly deviate from the aforementioned power-law scaling. This deviation is reliable since even when considering the uncertainty in the mass of the filament, which could be up to  $\sim 80\%$  (see Sect. 4.4.2), we do not anticipate a significant deviation in mass, on the order of magnitude, when the length of the filaments is held constant. In addition, similar deviation has been reported in the hub-composing filaments of nearby molecular clouds, such as Musca, L1495-B213 (Taurus), and Orion A (see Hacar et al. 2023). It is worth noting that these hub-composing filaments investigated here have high line masses greater than a threshold line mass of  $230 M_\odot \text{ pc}^{-1}$ . This threshold indicates high-mass star formation as inferred by Li et al. (2016), following Eq. 12 of Fiege & Pudritz (2000), using a lower limit ( $0.7 \text{ km s}^{-1}$ ) of line widths obtained from ammonia observations of massive star-forming clumps (Dunham et al. 2011; Urquhart et al. 2011; Wienen et al. 2012).

Furthermore, these numbered hub-composing filaments (see Fig. 8) are found to be associated with HII regions (see Col. 12 of Table B2). The dust temperatures of these filaments could be higher than those reported in Table B1. If the temperature were higher by a factor of two, the mass of the filament would be underes-

**Table 2.** KWH test results of clump properties for three groups including NFR, FR and HR clumps

Property group	R (pc)	M ( $M_\odot$ )	$\Sigma$ ( $\text{g cm}^{-2}$ )
p-value	$1.8 \times 10^{-11}$	$2.6 \times 10^{-30}$	$2.3 \times 10^{-31}$
$\chi^2$	49.5	136.3	141.1

**Notes.** if  $p$ -value is smaller than the significance level, the null hypothesis will be rejected. A larger  $\chi^2$  indicates a more significant difference between different groups.

timated by the same factor. However, this would not significantly impact the evident deviation of these HFS filaments from the global trend observed in the mass-length distribution of most filaments. In light of this, these hub-composing filaments could therefore be influenced by feedback from massive star formation, such as the expansion of HII regions and bubbles. This feedback, in conjunction with ambient turbulence, acts as external forces that can condense and break up the gas. Generally, this leads to formation of more thermally supercritical filaments that compose the hub, as discussed by Shimajiri et al. (2019). Consequently, this causes the filaments to make a nearly vertical downward shift in the M-L plot.

It is important to note that the discussions we made above on the the M-L plot may be affected by observational biases. Schisano et al. (2020) found that the filament length measured from ground-based observations is generally 2-4 times shorter than those from space observations given a comparable filament mass. This difference, resulting from observational biases, could potentially explain why the HFS sample provided by space observations does not deviate significantly from non-hub filaments in the M-L plot in Kumar et al. (2020), as opposed to the result shown here in Fig. 8.

Additionally, we do not find a scaling relation (and hence not shown here) between filament density ( $\langle n \rangle$ ) and  $L$ , similar to the third Larson's relation. Hacar et al. (2023) suggested that such a relation is equivalent to the assumption of constant column density for filaments, which does not hold for our samples. This result could be due to the fact that filament densities depend on the asymmetric structure of the cylinders, and thus the density estimate under the assumption of a spherical morphology could affect the resulting  $\langle n \rangle$ - $L$  relation.

### 5.2. HFS clouds as a preferential site of HMSF

Fig. 4 shows the spatial distribution of clumps along with their masses, and mass surface densities. In Fig. 4 (a), 75% of massive clumps ( $M \geq 20 M_\odot$ ) are located in the filaments, whereas low-mass clumps are

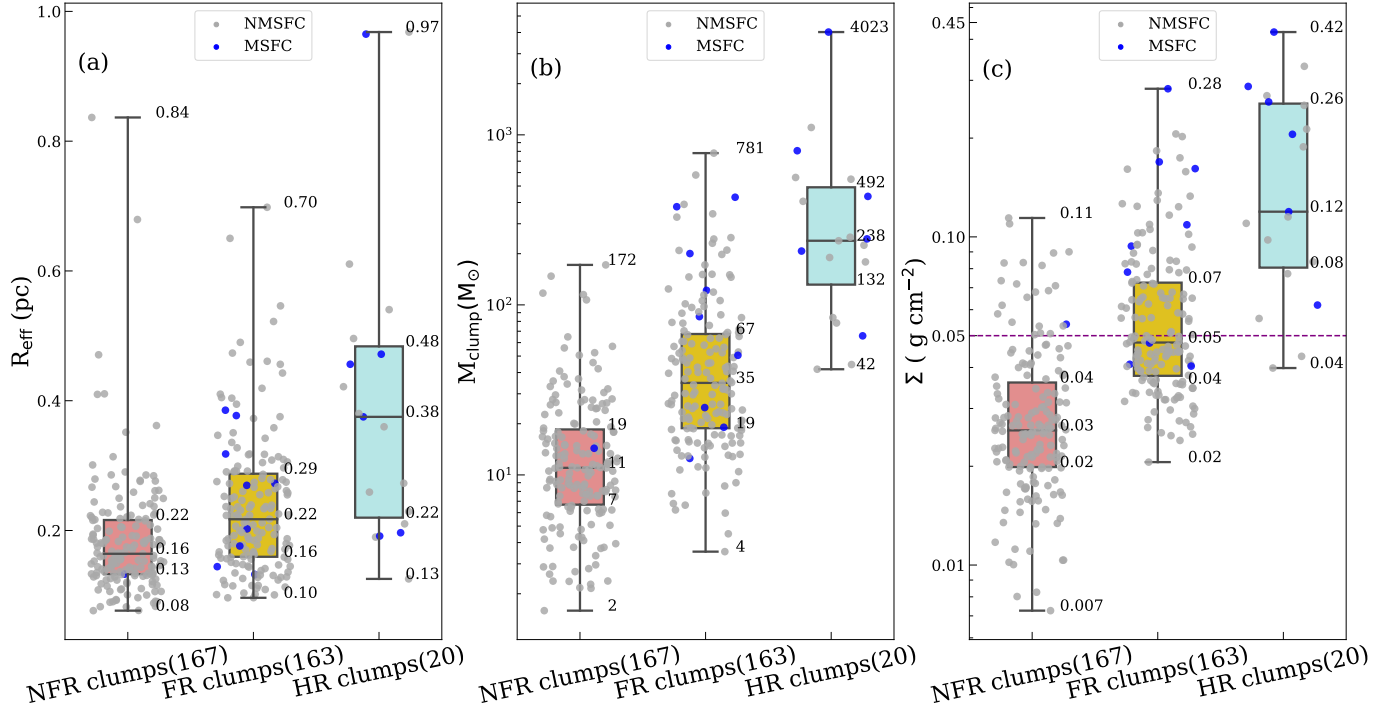


**Figure 9.** Box plots of the physical properties including effective radius (a), mass (b), and mass surface density (c) for three classes of clumps (i.e., NFR, FR, and HR clumps, see the text). The numbers within the parentheses in each classification indicate the quantity of clumps belonging to each class. The boxes represent the quartile range of the data, from the bottom to the top of each box, including the lower quartile (i.e., the 25th percentile), the median inside the box, and the upper quartile (i.e., the 75th percentile). The "whiskers" present the full extent of the data (i.e., minimum value and maximum value). The purple dashed line in panel (c) represents a mass surface density of  $0.05 \text{ g cm}^{-2}$ . Scatter plots show the concentration of data, while whiskers represent the extent of data distribution. Different colored scatters mark the MSF clumps (MSFC) and Non-MSF clumps (NMSFC).

distributed more widely. The HFSs have many massive clumps at the hubs. For example, the longest one (i.e., HFS8 in Fig. A5) contains massive clumps associated with MYSOs typical of high-mass protostars, as reported by the RMS survey (Urquhart et al. 2008), and include a nascent stellar cluster G35.60-0.00 (Kuhn et al. 2021).

The mass surface density is another key parameter in star formation, especially for high-mass star formation. Thresholds for massive star formation, advocated by several authors (e.g., Krumholz & McKee 2008; Urquhart et al. 2014b) lie in the range from  $0.05 \text{ g cm}^{-2}$  to  $1.0 \text{ g cm}^{-2}$ . As shown in Fig. 4(b), the mass surface densities of clumps in hubs or ridges (i.e., IRDC G35.39 and  $8 \mu\text{m}$ -bright ridge G35.6-0.0) are higher than the ATLASGAL clumps' lower limit of  $0.05 \text{ g cm}^{-2}$  (Urquhart et al. 2014b). These observed trends are in good agreement with the previous observations which have characterised the essential roles of HFSs in massive star formation (e.g., Schneider et al. 2012; Peretto et al. 2013; Kumar et al. 2020, 2022; Arzoumanian et al. 2023).

Our observations of massive and dense clumps lying in filamentary structures or located at their junctions are qualitatively very similar to the previous results of MHD simulations (e.g., Inoue & Fukui 2013; Gómez & Vázquez-Semadeni 2014; Chen & Ostriker 2015; Gong & Ostriker 2015; Inoue et al. 2018). In these simulations, converging turbulent flows, colliding flows or cloud–cloud collisions are considered as the vital factors to produce the dense filaments and HFSs naturally. Meanwhile, the growth pattern of central clumps follows the "clump-fed" model (Smith et al. 2009) that central massive clumps act as reservoirs of high-mass star formation in the HFSs, gaining mass through gas accretion from their large-scale environments such as filaments. Theoretically, the global hierarchical collapse scenario (Vázquez-Semadeni et al. 2019) further emphasizes the pivotal role of filaments in molecular cloud evolution, accumulating material through radial accretion from ambient gas and feeding dense clumps through longitudinal contraction.

For further analysis, we divide 350 clumps into three groups based on their location in filaments, in hubs or neither in both (see Fig. 3 for example): 167 non

filament-rooted (NFR), 163 filament-rooted (FR), and 20 hub-rooted (HR) clumps. The numbers in each category could be influenced by the level of background subtraction achieved. However, this effect will not be further examined as such background subtraction was not specifically performed, except for the one incorporated during the data-processing stage (see Sect. 3.1). Fig. 9 reveals an increasing trend of the median value for all three physical parameters (i.e., clump radius, mass, mass surface density) from NFR, FR to HR clumps. Particularly, the median value of mass surface density increases by a factor of 4 from NFR, FR, to HR clumps, while the same for mass increases by a factor of 17. The observed trends persist even if we account for the uncertainty around 10% for the radius of clumps, around 44% for the mass, and around 39% for the mass surface density (see Sect. 4.4.2). In addition, similar increasing trends of clump radius/mass from the NFR clumps and FR clumps were also found in the study of cores in Orion (Polychroni et al. 2013). To evaluate such increasing trends further, we applied Kruskal-Wallis H test, which can infer the difference among the distributions of multiple independent samples from different populations. The null hypothesis usually assumes that the samples come from the same parent population. Table 2 shows the  $p$ -values and  $\chi^2$  of the Kruskal-Wallis H test for physical parameters of one group against others. Since the  $p$ -values of all cases are much lower than 0.05, we reject the null hypothesis, and conclude that all three classification groups of clumps have different distributions, in terms of the radius, mass, and mass surface density parameters. Therefore, the observed increasing trends of these three parameters from NFR, FR to HR clumps could be significant. Accordingly, these trends underscore the tendency for massive dense clumps to associate with filaments and HFSs. Particularly, the densest HR clumps offer conducive conditions for high-mass star formation, indicating HFSs as preferential sites for such star formation.

We also used different tracers from previous catalogs, such as class II methanol masers, MYSOs, and ultra-compact (UC) HII regions, to match our clumps with signposts of massive star formation. As a result, we identified 16 such massive star-forming (MSF) clumps. Among them, 15 preferentially reside in filaments or in the hubs within HFSs (see Fig. 9). Although the counts of high-mass star-forming clumps are similar between the HFS's hubs and the isolated filaments, the former has a much higher fraction of the observed population than the latter does. This quantitative analysis favors the importance of filaments in high-mass star formation, and even the HFS clouds as a preferential site of HMSF.

### 5.3. Evolution of clump density

We select the distance-independent parameter of clump mass surface density to examine how critical parameters of HMSF evolve in different star-forming environments. For this analysis, we focus on clouds with evident infrared-dark (IR-dark) and infrared-bright (IR-bright) signatures. The presence of IRDCs (i.e., G35.39 and G35.41) suggest quiescent star formation in Clouds 1 and 2. In comparison, the detection of several HII regions (Anderson et al. 2014) in Cloud 4, which are seen as IR-bright signatures, indicates active star formation activity, and a relatively later evolutionary phase (see Sect. 2). Given the weak 850  $\mu\text{m}$  emission in Cloud 3 and Cloud 5 relative to other clouds, these have been excluded from the discussion here.

Fig. 10 (a) shows the comparison of the densities of the clumps located at two different evolutionary stages of clouds at different distances (IR-dark Cloud 1 & 4 v.s. IR-bright Cloud 4). As seen in Fig. 10 (a), the mass surface densities of clumps are slightly higher in the IR-bright clouds than in the IR-dark counterparts with a median ratio of 1.3. We conduct the two-sample Kolmogorov-Smirnov (KS) test to investigate if they are statistically identical. The statistical results, with yielding (a) in a  $p$ -value  $\sim 0.005$ , suggest that the samples are unlikely to be drawn from the same parent population. The weak trend implies a possible increasing trend for the mass surface density of clumps from the IR-dark to IR-bright stage. In their statistical study of a sample of 17 HFS clouds using ALMA data, Liu et al. (2023) have observed a similar increasing trend (by a factor of around 3) in the central massive clumps from IR-dark to IR-bright HFSs. Several other systematic studies (e.g., Giannetti et al. 2013; Urquhart et al. 2014b; Rigby et al. 2021; Xu et al. 2024) also conjecture a similar positive correlation of density as a function of evolutionary sequence. It is also worth noting that there are other studies (e.g., López-Sepulcre et al. 2010; Rathborne et al. 2010; Sánchez-Monge et al. 2013), where no significant differences in column densities (equivalent to surface densities) were observed for clumps. Furthermore, clumps in the HII region phase show an even greater difference in surface densities compared to the other stages (e.g., Urquhart et al. 2014b; He et al. 2015). On the contrary, Guzmán et al. (2015) presented results of 3000 massive MALT90 clumps in disagreement with the previous enhanced densities in the group of HII regions. Their study shows that the surface density of clumps tends to decrease during the development of HII regions. Note that the observed trend should be treated with caution, given the estimated uncertainties (see Sect. 4.4.2 and 5.2).

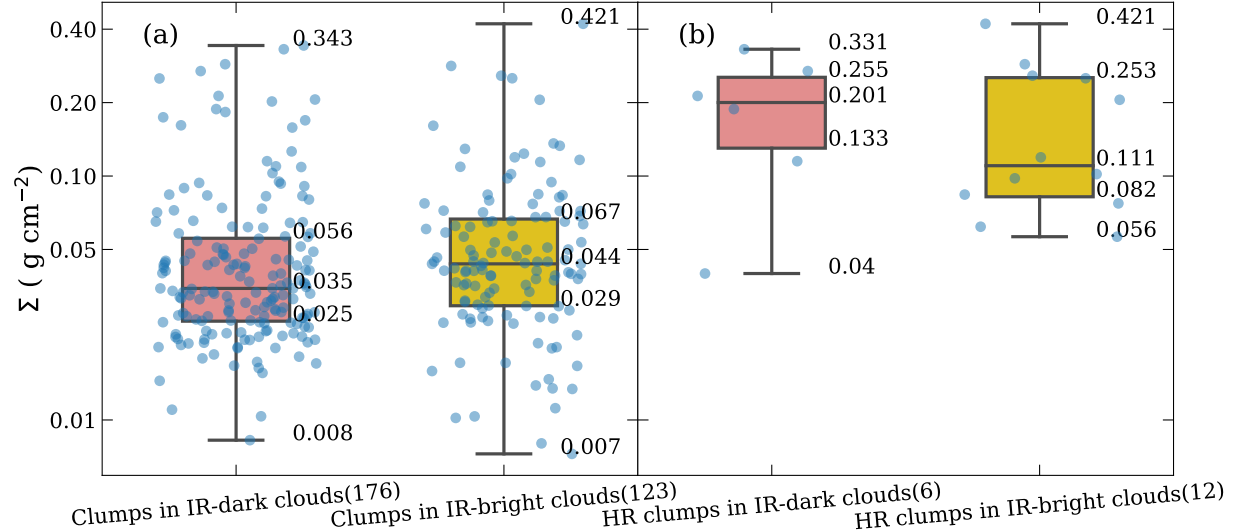


**Figure 10.** Box plots for comparison of mass surface density between clumps in IR-dark environment (i.e., in Cloud 1 and/or Cloud 2) and those in IR-bright environment (i.e., in Cloud 4). (a) Comparison between clumps in IR-dark Cloud 1 & 2 and those in IR-bright Cloud 4. (b) Distribution of mass surface density of HR clumps (i.e., located at hubs) in both IR-dark (i.e., in Cloud 1 & 2) and IR-bright (i.e., in Cloud 4) environments. The numbers in parentheses of the horizontal axis label represent the sample counts in each group.

If we consider the HR clumps depicted in Fig. 10 (b), these massive structures, rooted in the central hub of HFS clouds, exhibit a decreasing surface density trend from an IR-dark to an IR-bright stage, contrasting with the previously mentioned weak increasing trend. A two-sample KS test also conducted on the two groups yielded a  $p$ -value of 0.76, suggesting a common origin. Consequently, the observed decreasing trend should be interpreted with caution. Under the framework of the latest theoretical models like GHC and I2, high-mass star formation in HFSs involves a multiscale mass accretion/transfer process from the cloud to filaments and then onto the central hub and finally to the star-forming cores. Thus, clumps located in the central hubs would be in a state of active accretion, increasing in mass and surface mass density. However, for HR clumps in IR-bright clouds, 11 out of the 12 clumps are associated with HII regions. In this phase, ionizing feedback and radiation pressure from MYSOs would play an important role in influencing the temporal trend of mass surface density in these clumps. Given the critical role of this trend in understanding mass accretion and high-mass star formation, further dedicated observational studies are warranted.

## 6. CONCLUSIONS

In this paper, we have carried out a systematic analysis on the filaments and their hierarchically-fragmented clumps in the G35 molecular complex, centered at  $\alpha_{2000} = 18^{\text{h}}56^{\text{m}}28^{\text{s}}.16$ ,  $\delta_{2000} = 2^{\circ}14'25.^{\prime\prime}71$ , with an approximate radius of  $0.41^{\circ}$  from SCUBA-2 850  $\mu\text{m}$  con-

tinuum observations. We focus on the basic physical properties of the filaments and clumps, including the mass, density, and size. The major results are as follows:

(1) Five clouds, namely Cloud 1–5, were identified. Their respective kinematic distances, estimated from the  $^{13}\text{CO}$  (1–0) line data, are 2.9 kpc, 5.1 kpc, 2.9 kpc, 2.9 kpc, and 2.1 kpc.

(2) We extracted a sample of 91 filaments, some of which can be divided into 10 HFSs, each composed of at least 3 hub-composing filaments. A catalogue of 350 dense clumps was compiled, 183 out of which are associated with the filaments.

(3) The identified filaments have a median width of 0.51 pc, lengths ranging from 0.7 pc to 9.1 pc, and masses between  $\sim 26$ – $2962 \text{ M}_\odot$ . All exceed the thermally critical line mass of  $16.6 \text{ M}_\odot \text{ pc}^{-1}$ , with a median value of  $84 \text{ M}_\odot \text{ pc}^{-1}$ . The clumps, with a median size of  $\sim 0.4$  pc and mass of  $\sim 20 \text{ M}_\odot$ , have a similar average column density to the filaments, suggesting a density inheritance from larger-scale filaments.

(4) The global mass-length trend of filaments, close to  $L \propto M^{0.5}$ , suggests that their physical origin is linked to turbulence. For those hub-composing filaments within HFSs, they deviate from the global mass-length trend, which could be due to feedback from massive star formation therein, particularly HII regions.

(5) Massive clumps, which most likely form high-mass stars, are the densest in filaments and in the hubs of HFSs with the latter bearing a higher probability of oc-

currence of high-mass star-forming signatures, favoring the HFSs as a preferential site of high-mass star formation.

(6) We examined the variation in clumps' mass surface density relative to their host cloud environment, from the IR-dark to IR-bright stage. No significant variation was observed. This could be attributed to the regulation of clump properties, such as mass surface density, by the interplay between mass accretion and feedback from HII regions.

Overall, we have provided filament and dense clump samples in the G35 molecular complex to explore their connection with star formation. The significance of filaments, especially hub-composing filaments in HFSs, for high-mass star formation is highlighted. Further observational studies particularly on kinematics and dynamics are needed to understand the mass accretion process in high-mass star formation through these density structures.

This work has been supported by the National Key R&D Program of China (No. 2022YFA1603101). X.-J. Shen is supported by the 15th Graduate Student Research and Innovation Project of Yunnan University (Project ID:KC-23233964). H.-L. Liu is supported by National Natural Science Foundation of China (NSFC) through the grant No. 12103045, by Yunnan Fundamental Research Project (grant No. 202301AT070118, 202401AS070121), and by Xingdian Talent Support Plan–Youth Project. H.B.L. is supported by the National Science and Technology Council (NSTC) of Taiwan (Grant Nos. 111-2112-M-110-022-MY3). PS was partially supported by a Grant-in-Aid for Scientific Research (KAKENHI Number JP22H01271 and JP23H01221) of JSPS. The work of M.G.R. is supported by NOIRLab, which is managed by the Association of Universities for Research in Astronomy (AURA) under a cooperative agreement with the National Science Foundation. K.T. was supported by JSPS KAKENHI (Grant Number JP20H05645).

*Software:* Starlink (Currie et al. 2014), Astropy (Astropy Collaboration et al. 2013), FILFINDER (Koch & Rosolowsky 2015), Aplpy (Lisa & Bot 2017), Source Extractor (Bertin & Arnouts 1996; Barbary 2016)

## APPENDIX

### A. COMPLEMENTARY FIGURES

#### A.1. Noise map analysis of $850\mu\text{m}$ dust observations

Fig. A1 displays the spatial distribution of the noise map (left panel) and the associated statistics (right panel).

#### A.2. Molecular gas distribution in the G35 complex

To approximately identify each cloud in the G35 molecular complex, we provide in Fig. A2 the average spectrum of  $^{13}\text{CO}$  ( $J=1-0$ ) over the entire complex, and in Fig. A3 the JCMT  $850\mu\text{m}$  continuum image overlaid with the intensity contours of  $^{13}\text{CO}$  for each individual cloud.

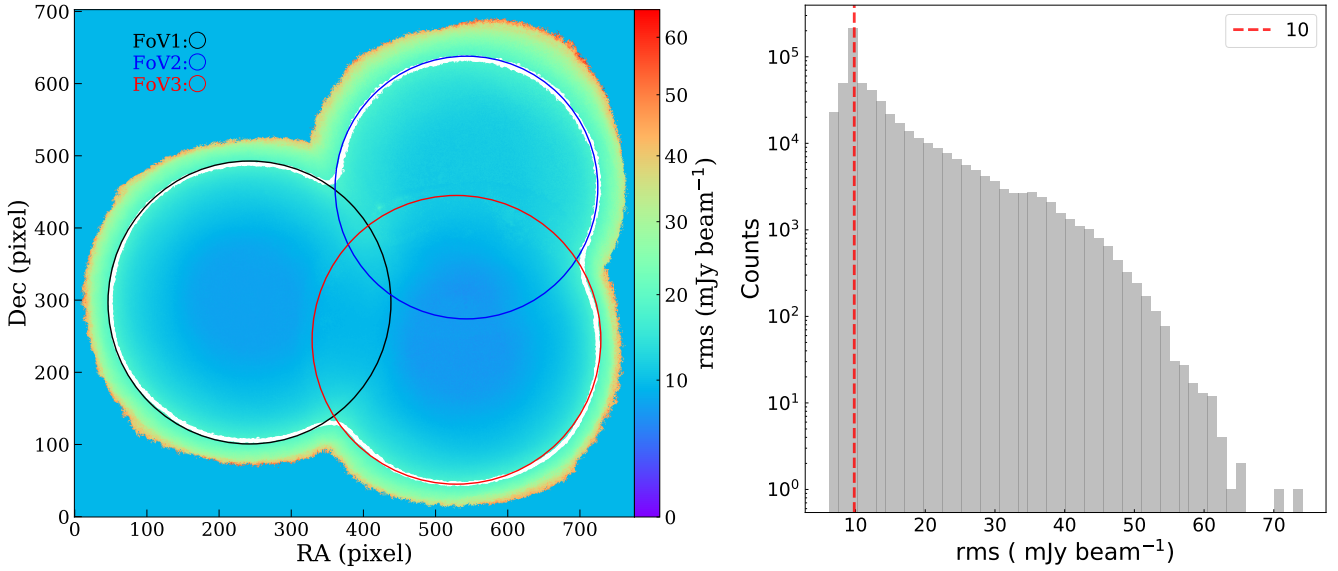


**Figure A1.** Noise map and statistical histogram of the  $rms$ . *Left:* the color map present the  $rms$  varying from 5 to  $75\text{ mJy beam}^{-1}$  and the white contour indicates  $rms$  value of  $20\text{ mJy beam}^{-1}$ . The colored circles pinpoint three FoVs considered for analysis. *Right:* the histogram shows the distribution of the  $rms$  with a median value of  $10\text{ mJy beam}^{-1}$  (red dashed line).

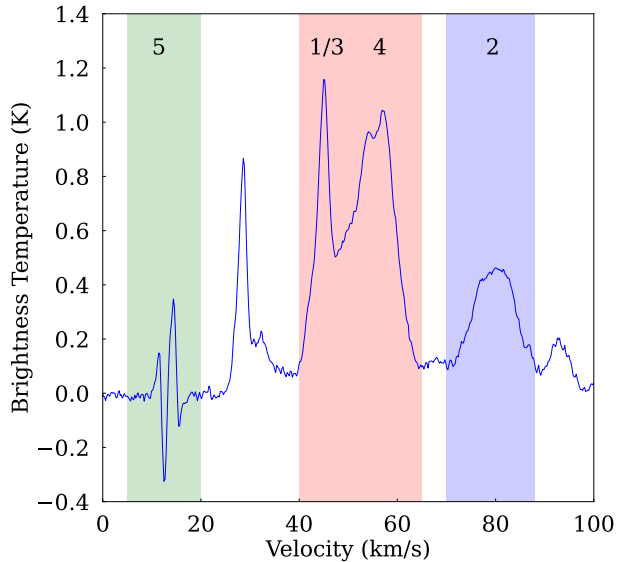


**Figure A2.** Average spectrum of  $^{13}\text{CO}$  (1–0) emission over the G35 molecular complex. The color bands highlight three major velocity components, corresponding to [5, 20], [40, 65], and [70, 85]  $\text{km s}^{-1}$  in green, red, and blue, respectively. The numbers represent the cloud IDs.

### A.3. Spatial distribution of dust filamentary structures in the G35 complex

Fig. A4 shows the filamentary structures identified in Sect. 4.3.1 overlaid on the dust temperature map. Fig. A5 presents the spatial distribution of 10 HFSs overlaid on *Spitzer* 8  $\mu\text{m}$  infrared image.

### A.4. Flux comparison of the clumps observed both in previous 870 $\mu\text{m}$ and our 850 $\mu\text{m}$ observations

We examined the variance in peak flux density of the 37 matched clumps between the two catalogues from the ATLASGAL survey (Urquhart et al. 2018) at 870  $\mu\text{m}$  and our own at 850  $\mu\text{m}$ . Owing to the higher angular resolution ( $14''$ ) of our observations, we recalibrated the 850  $\mu\text{m}$  peak flux density to match the angular resolution ( $19''$ ) at 870  $\mu\text{m}$ . This recalibrated value of the 850  $\mu\text{m}$  peak flux density was then utilized to predict the 870  $\mu\text{m}$  peak flux density using

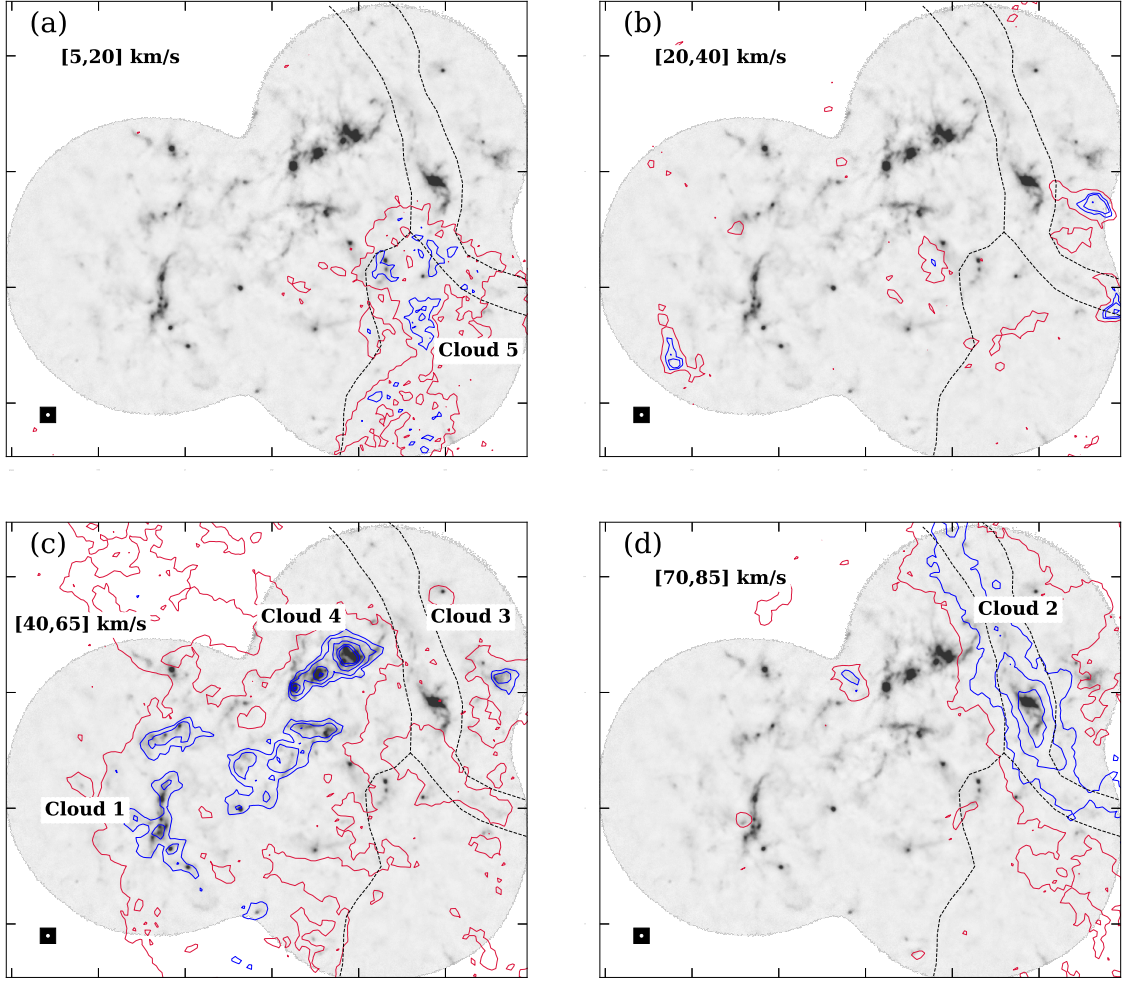
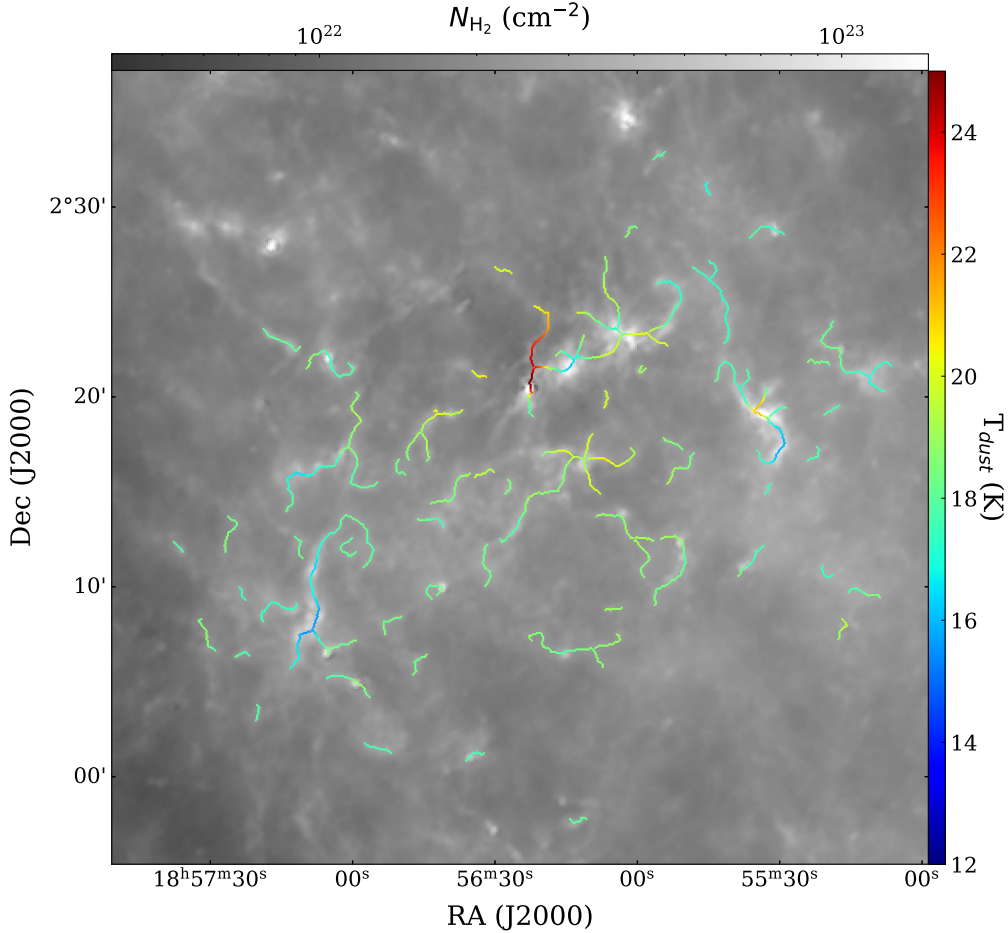


**Figure A3.** JCMT 850  $\mu\text{m}$  continuum image overlaid with  $^{13}\text{CO}$  integrated intensity contours of different velocity components. They correspond to [5, 20], [40, 65], and [70, 85] km/s. The  $rms$  levels ( $\sigma$ ) of the four integrated intensities from (a) to (b) are  $\sigma_1=0.73 \text{ K km s}^{-1}$ ,  $\sigma_2=0.72 \text{ K km s}^{-1}$ ,  $\sigma_3=2.82 \text{ K km s}^{-1}$  and  $\sigma_4=1.28 \text{ K km s}^{-1}$ , respectively. The red contour in each panel indicates the the  $5\sigma$  level. The blue contour levels from panel (a) to (b) are  $[8\sigma_1, 10\sigma_1] \text{ K km s}^{-1}$ ,  $[8\sigma_2, 10\sigma_2, 15\sigma_2] \text{ K km s}^{-1}$ ,  $[10\sigma_3, 12\sigma_3, 15\sigma_3, 18\sigma_3, 20\sigma_3] \text{ K km s}^{-1}$ , and  $[10\sigma_4, 15\sigma_4, 20\sigma_4] \text{ K km s}^{-1}$ , respectively. According to the spatial association between gas and continuum emission, boundaries of different clouds are delineated by the black dashed lines. The beam size of 850  $\mu\text{m}$  observations is also displayed at the bottom left corner of each panel.

a power-law relation ( $S_\nu \propto \nu^\alpha$ ) and a spectral index  $\alpha = -2$ . Fig. A6 illustrates the comparison between the 870  $\mu\text{m}$  peak flux density observed from the ATLASGAL survey and the result predicted from our 850  $\mu\text{m}$  observations. The peak flux densities display a strong linear correlation with a Pearson correlation coefficient of 0.99, with the predicted flux densities exceeding the observed ones by approximately 21%. This implies that the flux measurements for clump sources are consistent between the previous 870  $\mu\text{m}$  and our 850  $\mu\text{m}$  observations, considering the systematic flux uncertainties of about 15% in the former (e.g., Schuller et al. 2009) and about 6% in the latter (see Sect. 3.1).

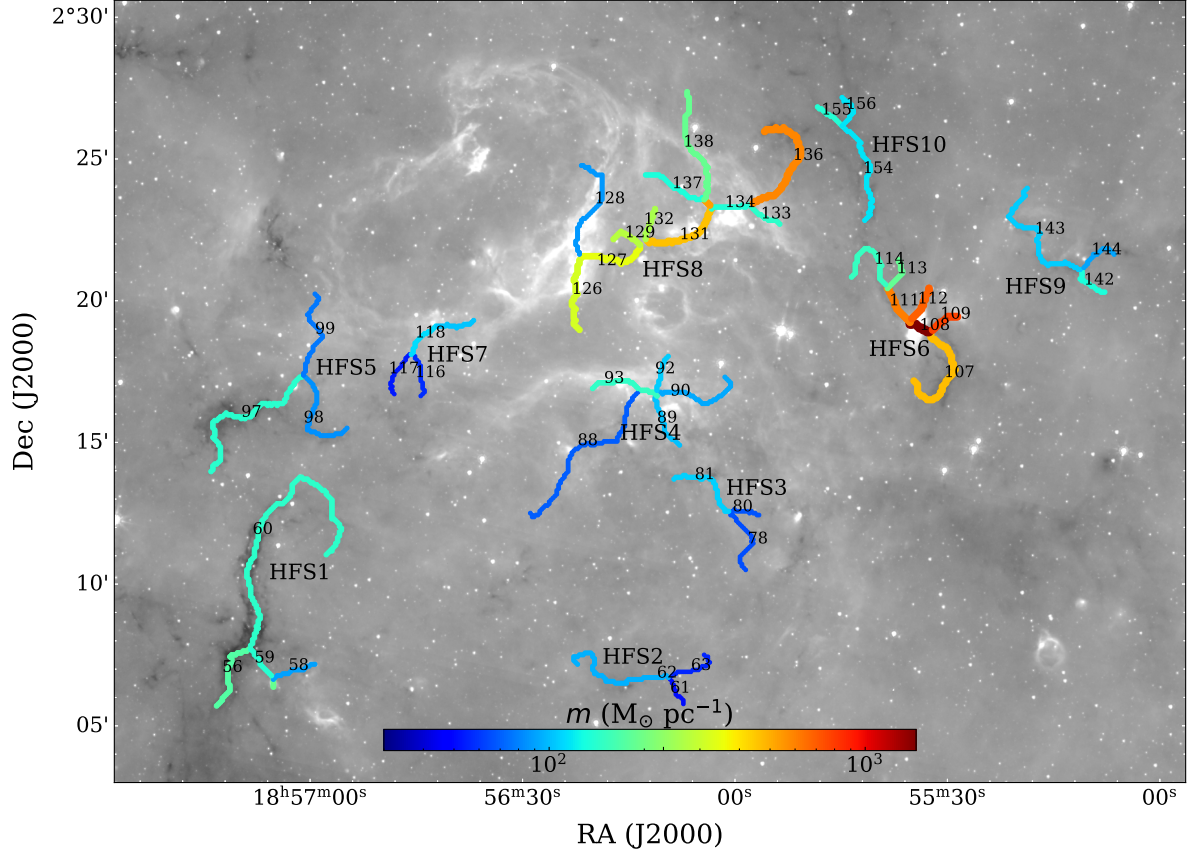
#### A.5. $NH_3$ (1-1) data selected for filament kinematic analysis

Higher-J CO line data are assumed to be superior for tracing filament kinematics compared to the CO J=1–0 line observed for example in the FUGIN (Umemoto et al. 2017) and GRS (Jackson et al. 2006) surveys. This arises from their enhanced accessibility to the dense filament's physical properties, due to their higher critical excitation density. Furthermore, the G35 complex has access to  $NH_3$  line data from the RAMPS (Hogge et al. 2018) survey, which has an angular resolution of 32''. Despite the low detection rate of the  $NH_3$  line data in the G35 complex, similar to higher-J



**Figure A4.** Filament skeletons overlaid on the column density map. The color of each structure represents its average dust temperature derived from *Herschel* observations.

CO line data, the  $\text{NH}_3$  line is assumed to be more sensitive to the kinematics of dense gas than other lines available here. Consequently, we utilize the RAMPS  $\text{NH}_3$  line data to approximately quantify the turbulence contribution. Fig. A7 displays the linewidth distribution of this species toward the G35 molecular complex.



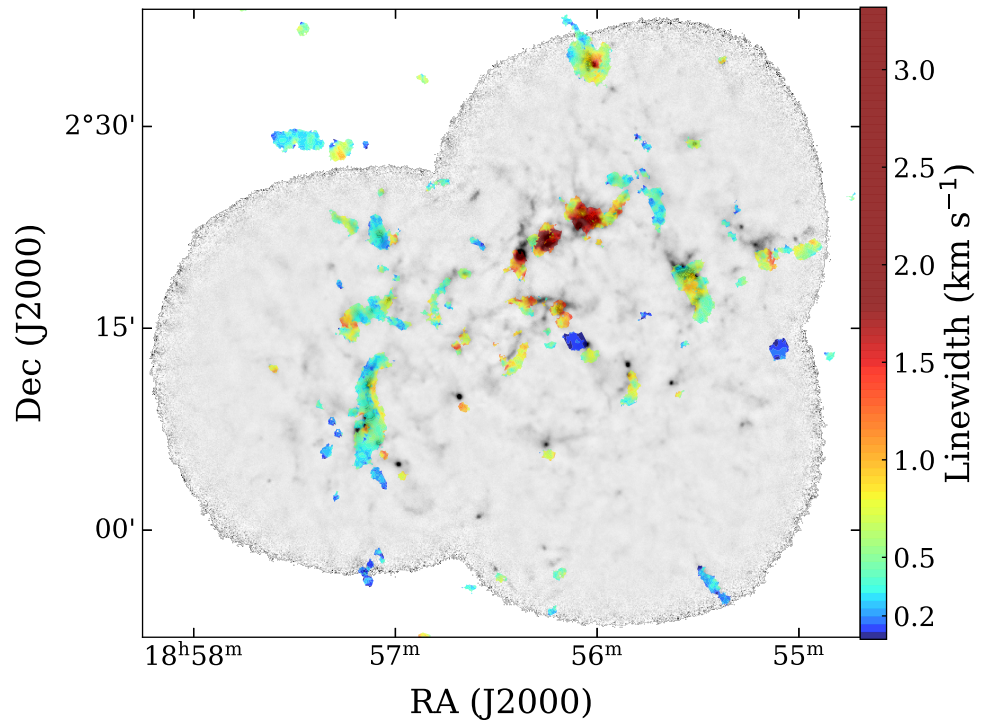


**Figure A7.**  $\text{NH}_3$  (1-1) linewidth (rainbow color) overlaid on  $850\mu\text{m}$  continuum map (gray color).

## B. COMPLEMENTARY TABLES

We list the tables of detailed parameters for the clumps and filaments. Table B1 gives basic information of each filament, the resultant physical properties for statistical analysis, their association (Assoc.) with both HMSF and HFSs. Table B2 presents the basic parameters of 350 clumps, including their position, position angle (PA), flux, distance, as well as the derived physical parameters such as mass and surface density.

**Table B1.** Parameters of filamentary structures

ID	Name	RA	Dec	Flux	D	Mass	Length	Width	T <sub>dust</sub>	N <sub>H<sub>2</sub></sub>	Assoc.	Group
(1)	(2)	(3)	(4)	(5)	(6)	(7)	(8)	(9)	(10)	(11)	(12)	(13)
44	G35.220-0.164	284.049	1.962	868±347	2.9	50±29	1.0	0.3	17.3	8.6 ± 4.7	-	-
46	G35.312-0.216	284.137	2.020	1032±671	2.9	59±46	0.9	0.3	17.4	8.7 ± 6.5	-	-
47	G35.358-0.294	284.228	2.025	1352±641	2.9	77±49	1.4	0.3	17.4	7.3 ± 4.4	-	-
51	G35.433-0.373	284.333	2.055	465±206	2.9	26±16	0.8	0.3	17.6	4.9 ± 2.8	-	-
54	G35.433-0.306	284.273	2.086	4325±2393	2.9	232±161	2.5	0.5	18.1	8.5 ± 5.7	-	-
55	G35.411-0.229	284.195	2.102	1269±916	2.9	67±56	1.3	0.4	18.2	5.3 ± 4.3	-	-
56	G35.470-0.315	284.298	2.115	6412±4680	2.9	408±350	2.4	0.4	15.9	19.0 ± 16.0	D	HFS1
58	G35.454-0.280	284.259	2.116	2300±1679	2.9	121±106	1.3	0.4	18.0	10.1 ± 8.4	Y	HFS1
59	G35.467-0.296	284.279	2.121	2970±2168	2.9	166±118	1.2	0.4	17.9	16.1 ± 13.4	Y	HFS1
60	G35.534-0.262	284.281	2.196	22578±16482	2.9	1302±1153	9.1	0.4	17.0	16.1 ± 13.4	D	HFS1
61	G35.339-0.087	284.035	2.103	880±510	2.9	44±29	0.9	0.6	18.6	4.1 ± 2.9	-	HFS2
62	G35.351-0.089	284.043	2.112	6881±3991	2.9	353±241	3.7	0.6	18.3	7.5 ± 5.3	-	HFS2
63	G35.346-0.070	284.023	2.116	1741±1010	2.9	86±58	1.5	0.6	18.7	4.4 ± 3.1	-	HFS2
64	G35.486-0.363	284.348	2.107	562±249	2.9	32±20	0.8	0.3	17.4	7.3 ± 4.2	-	-
66	G35.513-0.382	284.377	2.123	1960±1435	2.9	102±85	1.7	0.7	18.5	4.0 ± 3.2	-	-
67	G35.266+0.118	283.819	2.131	1599±821	2.1	40±26	0.9	0.4	19.6	5.9 ± 3.7	-	-
68	G35.454-0.237	284.222	2.136	1113±804	2.9	60±49	1.5	0.4	18.1	4.4 ± 3.5	-	-
69	G35.512-0.324	284.325	2.148	2741±2053	2.9	159±132	2.6	0.4	17.2	6.3 ± 5.0	-	-
70	G35.373-0.054	284.021	2.147	773±366	2.9	39±25	0.8	0.4	18.9	5.9 ± 3.5	-	-
71	G35.376+0.017	283.959	2.183	9663±5538	2.1	269±192	3.6	0.3	18.2	10.0 ± 6.8	-	-
72	G35.291+0.136	283.815	2.162	1355±965	5.1	224±185	2.7	0.7	18.1	5.5 ± 4.4	-	-
73	G35.533-0.338	284.347	2.161	597±372	2.9	34±26	0.7	0.5	17.3	4.7 ± 3.3	-	-
74	G35.463-0.192	284.185	2.165	4686±2592	2.9	249±174	1.8	0.6	18.2	11.0 ± 7.3	-	-
76	G35.458-0.138	284.135	2.185	2424±1461	2.9	128±94	2.1	0.5	18.2	5.4 ± 3.8	-	-
78	G35.397-0.006	283.989	2.191	2761±1799	2.9	136±104	2.1	0.8	18.7	3.8 ± 3.3	-	HFS3
80	G35.417-0.005	283.998	2.210	1049±799	2.9	52±44	1.0	0.5	19.0	4.7 ± 3.9	M	HFS3
81	G35.444-0.016	284.020	2.228	5241±3452	2.9	259±200	2.4	0.8	18.7	6.3 ± 5.4	-	HFS3
82	G35.311+0.131	283.828	2.177	929±505	5.1	164±113	1.7	0.8	17.4	5.3 ± 3.4	-	-
83	G35.354+0.073	283.899	2.188	3236±1758	2.1	95±65	1.4	0.4	17.7	8.1 ± 5.3	-	-
84	G35.547-0.275	284.297	2.202	1701±1279	2.9	91±78	1.2	0.7	18.1	4.7 ± 3.7	-	-
85	G35.520-0.232	284.247	2.197	1762±1279	2.9	96±80	1.6	0.8	18.0	3.5 ± 2.8	-	-
86	G35.594-0.368	284.402	2.201	499±301	2.9	28±20	0.6	0.3	17.5	6.7 ± 4.7	-	-
87	G35.586-0.325	284.359	2.214	2407±1331	2.9	126±88	2.0	0.6	18.4	5.1 ± 3.4	-	-
88	G35.494-0.069	284.089	2.248	7920±5969	2.9	407±357	5.8	0.4	18.3	7.0 ± 5.6	H	HFS4
89	G35.484-0.021	284.043	2.262	3742±2820	2.9	177±156	1.7	0.4	19.3	10.0 ± 8.7	H	HFS4

**Table B1** *continued*

**Table B1** (*continued*)

ID	Name	RA	Dec	Flux	D	Mass	Length	Width	T <sub>dust</sub>	N <sub>H<sub>2</sub></sub>	Assoc.	Group
		(°)	(°)	(mJy)	(kpc)	(M <sub>⊙</sub> )	(pc)	(pc)	(K)	(×10 <sup>21</sup> cm <sup>-2</sup> )		
(1)	(2)	(3)	(4)	(5)	(6)	(7)	(8)	(9)	(10)	(11)	(12)	(13)
90	G35.501-0.014	284.044	2.280	5766±4345	2.9	262±233	2.8	0.4	19.8	9.3 ± 7.9	H	HFS4
92	G35.510-0.009	284.044	2.291	2611±1968	2.9	122±107	1.2	0.4	19.4	11.0 ± 9.5	-	HFS4
93	G35.520-0.039	284.075	2.285	6253±4888	2.9	291±258	1.9	0.4	19.5	15.1 ± 12.9	-	HFS4
96	G35.516-0.163	284.184	2.225	1724±1245	2.9	95±78	1.5	0.4	17.8	7.6 ± 6.1	-	-
97	G35.599-0.237	284.287	2.265	13978±8273	2.9	780±577	5.5	0.6	17.3	11.2 ± 7.8	D;H	HFS5
98	G35.579-0.206	284.251	2.262	4967±2880	2.9	261±190	3.1	0.6	17.9	6.5 ± 4.5	D;H	HFS5
99	G35.622-0.176	284.244	2.314	4664±2705	2.9	230±170	3.0	0.6	18.7	5.9 ± 4.1	Y;H	HFS5
100	G35.526-0.132	284.160	2.248	3830±2500	2.9	196±152	2.6	0.5	18.6	7.4 ± 5.6	-	-
101	G35.510-0.085	284.112	2.255	670±335	2.9	36±23	0.8	0.3	18.1	7.4 ± 4.2	-	-
102	G35.403+0.115	283.885	2.252	402±220	5.1	74±58	1.1	0.4	17.0	8.7 ± 6.5	-	-
103	G35.455+0.056	283.960	2.271	2447±1402	2.9	125±89	2.3	0.5	18.7	5.0 ± 3.4	-	-
104	G35.567-0.168	284.212	2.268	974±563	2.9	52±36	1.1	0.5	18.2	4.4 ± 3.1	-	-
105	G35.530-0.100	284.134	2.266	851±589	2.9	41±33	1.0	0.4	19.5	4.7 ± 3.7	-	-
107	G35.431+0.141	283.874	2.288	15949±9212	5.1	2962±2124	6.4	1.0	16.5	21.0 ± 15.5	D	HFS6
108	G35.462+0.141	283.888	2.316	8618±5437	5.1	1241±879	0.9	1.0	20.9	63 ± 42.8	Y;H;M	HFS6
109	G35.462+0.155	283.876	2.323	6970±4321	5.1	1207±929	1.6	1.0	17.3	34.0 ± 25.5	H	HFS6
111	G35.483+0.132	283.906	2.331	7241±4289	5.1	1200±924	2.0	1.0	17.6	26.0 ± 19.5	H	HFS6
112	G35.475+0.147	283.889	2.331	9847±6105	5.1	1340±1031	2.0	1.0	20.2	30.1 ± 22.2	H	HFS6
113	G35.498+0.145	283.901	2.349	1938±1201	5.1	327±252	1.8	1.0	17.5	8.2 ± 6.1	D	HFS6
114	G35.509+0.135	283.915	2.355	3891±2412	5.1	651±501	4.4	1.0	17.6	6.5 ± 4.8	D	HFS6
116	G35.573-0.135	284.185	2.288	1581±870	2.9	78±55	1.3	0.5	18.8	5.1 ± 3.7	-	HFS7
117	G35.582-0.148	284.200	2.291	1617±889	2.9	81±58	1.5	0.5	18.6	4.7 ± 3.2	-	HFS7
118	G35.594-0.125	284.185	2.312	2470±1358	2.9	118±84	1.1	0.5	18.9	9.9 ± 6.7	-	HFS7
119	G35.589-0.102	284.163	2.318	2708±1489	2.9	143±92	1.4	0.5	19.2	9.1 ± 5.5	H	HFS7
121	G35.410+0.166	283.842	2.281	816±403	2.9	45±29	1.0	0.4	17.7	5.4 ± 3.2	-	-
123	G35.478+0.058	283.969	2.293	789±554	2.9	41±34	1.0	0.4	18.4	4.7 ± 3.7	-	-
126	G35.574-0.031	284.093	2.337	19213±14794	2.9	771±693	2.5	0.6	21.3	23.0 ± 20.2	H;Y;M	HFS8
127	G35.578+0.007	284.060	2.358	14216±10946	2.9	723±643	2.1	0.6	18.3	25.0 ± 22.0	H	HFS8
128	G35.616+0.005	284.079	2.391	7815±6017	2.9	300±264	3.5	0.6	22.2	6.2 ± 5.5	H	HFS8
129	G35.590+0.012	284.061	2.371	5527±4256	2.9	301±271	1.1	0.6	17.6	20.1 ± 17.5	H	HFS8
131	G35.574+0.042	284.028	2.371	13745±10584	2.9	663±597	2.6	0.6	19.0	19.0 ± 16.5	H	HFS8
132	G35.591+0.025	284.050	2.377	2732±2104	2.9	139±125	1.0	0.6	18.5	10.2 ± 8.9	-	HFS8
133	G35.565+0.087	283.984	2.383	3172±2442	2.9	143±127	1.1	0.6	19.9	9.8 ± 8.5	-	HFS8
134	G35.579+0.071	284.004	2.388	14436±11116	2.9	670±603	1.3	0.6	19.0	38 ± 33.1	H;Y;M	HFS8
136	G35.585+0.121	283.963	2.416	9791±7539	2.9	533±497	4.0	0.6	17.5	9.6 ± 7.7	-	HFS8
137	G35.603+0.050	284.034	2.399	7468±5750	2.9	380±336	2.0	0.6	18.4	14.1 ± 12.2	-	HFS8
138	G35.621+0.067	284.027	2.424	9974±7680	2.9	495±440	3.7	0.6	18.6	9.6 ± 8.4	-	HFS8
139	G35.441+0.198	283.828	2.323	835±570	2.9	47±38	0.9	0.3	17.5	8.0 ± 6.2	-	-
140	G35.539+0.026	284.026	2.332	803±341	2.9	38±23	0.9	0.3	19.6	7.3 ± 4.1	H	-
142	G35.442+0.239	283.791	2.343	2041±1326	2.9	115±91	1.1	0.4	17.2	11.0 ± 8.5	-	HFS9
143	G35.482+0.227	283.820	2.373	7338±4770	2.9	394±311	4.3	0.4	17.8	9.7 ± 7.5	D	HFS9
144	G35.456+0.251	283.787	2.361	2461±1600	2.9	139±110	1.2	0.4	17.2	12.0 ± 9.2	D	HFS9
145	G35.685-0.194	284.288	2.362	11334±6496	2.9	627±443	4.0	0.5	17.7	15.1 ± 10.4	D;Y	-

**Table B1** *continued*

**Table B1** (*continued*)

ID	Name	RA	Dec	Flux	D	Mass	Length	Width	T <sub>dust</sub>	N <sub>H<sub>2</sub></sub>	Assoc.	Group
(1)	(2)	(3)	(4)	(5)	(6)	(7)	(8)	(9)	(10)	(11)	(12)	(13)
146	G35.606-0.062	284.135	2.352	847±418	2.9	39±25	0.8	0.4	20.1	6.2 ± 3.8	H	-
147	G35.549+0.062	283.998	2.357	819±315	2.9	42±24	0.7	0.3	18.5	11.0 ± 5.8	-	-
150	G35.481+0.209	283.837	2.364	1347±986	5.1	220±184	2.1	1.1	18.3	4.4 ± 3.6	D	-
152	G35.716-0.207	284.314	2.383	2684±1939	2.9	149±123	2.2	0.3	17.7	9.8 ± 7.9	-	-
154	G35.559+0.154	283.921	2.408	4844±3565	5.1	841±723	6.1	0.9	17.2	6.6 ± 5.5	D	HFS10
155	G35.601+0.148	283.946	2.443	1058±772	5.1	181±157	1.6	0.9	17.4	5.6 ± 4.8	D	HFS10
156	G35.598+0.162	283.931	2.446	1087±793	5.1	185±159	1.8	0.9	17.4	7.9 ± 6.6	-	HFS10
158	G35.668-0.049	284.152	2.413	1614±1037	2.9	63±48	1.1	0.3	22.5	8.5 ± 6.3	H	-
160	G35.678-0.000	284.113	2.444	1137±742	2.9	53±41	0.9	0.6	19.9	4.4 ± 3.3	H	-
162	G35.603+0.224	283.879	2.479	3115±2219	2.9	177±146	1.9	0.4	17.4	9.8 ± 7.7	-	-
163	G35.664+0.111	284.007	2.482	660±323	5.1	107±70	1.7	0.5	18.4	5.6 ± 3.4	-	-
165	G35.663+0.187	283.939	2.516	331±232	5.1	62±50	1.2	0.6	16.8	4.2 ± 3.3	-	-
166	G35.707+0.165	283.979	2.545	758±344	5.1	131±82	1.1	0.5	17.6	11.0 ± 6.5	-	-

NOTE— Column 12 show the filaments that are linked to massive star forming sources summarized in Fig.1. The letter 'D' denotes the IRDCs, 'Y' represents the MYSOs, 'H' marks the H II regions, and 'M' stands for class II methanol masers. 'Group' indicates the structures to which the filaments belong. '-' indicates individual filaments, and the designation of the HFS to which the hub-composing filaments belong is also marked. The structure with ID 108 (belongs to HFS6) shows its width slightly greater than its length due to its location in a very bright HII region (see Fig. A5). The relative uncertainty of parameters of both length and width is 10%.

**Table B2.** Physical parameters of dense clumps

ID	RA	Dec	Size	PA	R	Flux	F <sub>peak</sub>	SNR	D	T <sub>dust</sub>	Mass	Σ	N <sub>H<sub>2</sub></sub>
(1)	(2)	(3)	(4)	(5)	(6)	(7)	(8)	(9)	(10)	(11)	(12)	(13)	(14)
1	283.869	1.951	18.4 × 14.3	-50.4	0.1	300±46	163	11	2.1	17.2	9±4	0.09±0.036	19.0±7.7
2	284.056	1.959	21.7 × 15.9	-3.8	0.1	320±47	148	13	2.9	16.9	19±9	0.07±0.03	15.8±6.3
3	284.042	1.978	27.5 × 13.7	-11.7	0.1	151±26	95	11	2.9	18.2	8±4	0.03±0.012	6.1±2.5
4	283.968	1.975	21.4 × 14.4	47.9	0.1	88±16	51	8	2.1	18.6	2±1	0.02±0.008	4.2±1.8
5	284.066	1.979	19.9 × 14.1	-44.7	0.1	328±39	196	21	2.9	18.3	17±8	0.08±0.033	17.8±7.0
6	283.931	2.002	25.2 × 14.3	-75.3	0.1	109±19	48	9	2.1	18.8	3±1	0.02±0.009	4.4±1.8
7	284.145	2.019	30.3 × 17.0	20.5	0.2	834±104	367	25	2.9	17.2	48±22	0.13±0.05	26.9±10.6
8	283.962	2.025	28.9 × 15.7	58.2	0.1	103±18	45	10	2.1	19.3	3±1	0.01±0.006	3.1±1.3
9	284.280	2.029	27.8 × 12.9	68.7	0.1	204±32	86	11	2.9	17.1	12±5	0.04±0.018	9.6±3.9
10	284.231	2.025	47.7 × 21.2	-17.9	0.2	605±89	112	12	2.9	17.2	35±16	0.05±0.019	9.9±4.0
11	284.214	2.034	36.7 × 17.8	49.5	0.2	149±27	77	9	2.9	17.9	8±4	0.02±0.007	3.6±1.5
12	283.989	2.046	25.2 × 10.4	-25.3	0.1	62±11	41	9	2.1	19.2	2±1	0.02±0.007	3.3±1.4
13	283.974	2.047	30.0 × 21.9	40.4	0.1	445±47	133	30	2.1	18.7	12±5	0.05±0.018	9.9±3.9

**Table B2** *continued*

**Table B2** (*continued*)

ID	RA	Dec	Size	PA	R	Flux	$F_{\text{peak}}$	SNR	D	T <sub>dust</sub>	Mass	$\Sigma$	N <sub>H2</sub>
	( $^{\circ}$ )	( $^{\circ}$ )	( $'' \times ''$ )	( $^{\circ}$ )	(pc)	(mJy)	(mJy beam $^{-1}$ )		(kpc)	(K)	(M $_{\odot}$ )	(g cm $^{-2}$ )	( $\times 10^{21} \text{cm}^{-2}$ )
(1)	(2)	(3)	(4)	(5)	(6)	(7)	(8)	(9)	(10)	(11)	(12)	(13)	(14)
14	284.050	2.024	24.5 $\times$ 15.0	23.8	0.1	123 $\pm$ 21	57	10	2.9	18.9	6 $\pm$ 3	0.02 $\pm$ 0.009	4.8 $\pm$ 2.0
15	284.042	2.032	24.1 $\times$ 15.3	-86.8	0.1	124 $\pm$ 19	60	12	2.9	18.6	6 $\pm$ 3	0.02 $\pm$ 0.009	5.0 $\pm$ 2.0
16	284.043	2.042	29.5 $\times$ 20.0	60.4	0.2	175 $\pm$ 29	50	10	2.9	19.0	9 $\pm$ 4	0.02 $\pm$ 0.008	4.2 $\pm$ 1.7
17	284.037	2.053	18.7 $\times$ 12.1	28.4	0.1	75 $\pm$ 12	44	9	2.9	19.2	4 $\pm$ 2	0.02 $\pm$ 0.009	4.7 $\pm$ 1.9
18	284.332	2.052	23.6 $\times$ 18.0	26.9	0.2	188 $\pm$ 28	84	13	2.9	17.4	11 $\pm$ 5	0.03 $\pm$ 0.014	7.2 $\pm$ 2.9
19	284.332	2.060	23.8 $\times$ 16.3	63.1	0.1	194 $\pm$ 26	98	16	2.9	17.3	11 $\pm$ 5	0.04 $\pm$ 0.015	8.3 $\pm$ 3.3
20	284.372	2.064	32.3 $\times$ 17.3	-14.3	0.2	266 $\pm$ 40	89	13	2.9	18.1	14 $\pm$ 6	0.03 $\pm$ 0.014	7.3 $\pm$ 3.0
21	284.054	2.074	18.6 $\times$ 14.2	-48.9	0.1	102 $\pm$ 15	60	13	2.9	19.4	5 $\pm$ 2	0.03 $\pm$ 0.01	5.4 $\pm$ 2.2
22	284.033	2.070	30.8 $\times$ 21.4	-66.2	0.2	281 $\pm$ 37	71	16	2.9	19.2	14 $\pm$ 6	0.03 $\pm$ 0.011	6.0 $\pm$ 2.4
23	283.829	2.077	18.3 $\times$ 12.4	-43.2	0.1	86 $\pm$ 14	59	10	2.1	18.4	2 $\pm$ 1	0.03 $\pm$ 0.011	5.7 $\pm$ 2.3
24	283.817	2.070	28.3 $\times$ 11.3	-50.8	0.1	100 $\pm$ 17	60	9	2.1	18.6	3 $\pm$ 1	0.02 $\pm$ 0.009	4.6 $\pm$ 1.9
25	283.928	2.080	19.3 $\times$ 17.1	16.7	0.1	84 $\pm$ 14	43	10	2.1	18.6	2 $\pm$ 1	0.02 $\pm$ 0.007	3.8 $\pm$ 1.6
26	283.993	2.092	27.6 $\times$ 19.8	-9.0	0.2	169 $\pm$ 26	51	12	2.9	18.3	9 $\pm$ 4	0.02 $\pm$ 0.009	4.7 $\pm$ 1.9
27	283.972	2.091	36.1 $\times$ 28.0	-68.2	0.2	278 $\pm$ 38	83	20	2.9	18.2	15 $\pm$ 7	0.02 $\pm$ 0.008	4.2 $\pm$ 1.7
28	284.343	2.110	30.5 $\times$ 24.1	52.4	0.2	454 $\pm$ 50	102	21	2.9	17.2	26 $\pm$ 12	0.05 $\pm$ 0.019	10.3 $\pm$ 4.0
29	283.962	2.123	25.7 $\times$ 12.3	83.8	0.1	87 $\pm$ 14	54	13	2.1	18.5	2 $\pm$ 1	0.02 $\pm$ 0.008	4.1 $\pm$ 1.7
30	283.874	2.126	38.8 $\times$ 23.6	-22.2	0.2	234 $\pm$ 34	62	14	2.1	18.8	6 $\pm$ 3	0.02 $\pm$ 0.007	3.7 $\pm$ 1.5
31	284.041	2.113	84.4 $\times$ 31.0	14.2	0.4	1624 $\pm$ 149	135	32	2.9	18.5	84 $\pm$ 37	0.04 $\pm$ 0.017	9.2 $\pm$ 3.5
32	284.064	2.110	67.3 $\times$ 58.9	25.4	0.4	4409 $\pm$ 361	466	100	2.9	17.7	244 $\pm$ 106	0.08 $\pm$ 0.032	17.7 $\pm$ 6.8
33	284.085	2.127	38.8 $\times$ 36.5	-0.2	0.3	830 $\pm$ 89	104	20	2.9	18.5	43 $\pm$ 19	0.04 $\pm$ 0.016	8.7 $\pm$ 3.4
34	284.016	2.120	37.2 $\times$ 18.5	23.3	0.2	340 $\pm$ 37	79	19	2.9	18.8	17 $\pm$ 8	0.03 $\pm$ 0.013	7.2 $\pm$ 2.8
35	284.097	2.121	25.7 $\times$ 12.5	-37.4	0.1	152 $\pm$ 18	70	13	2.9	18.7	8 $\pm$ 3	0.03 $\pm$ 0.013	6.9 $\pm$ 2.7
36	284.035	2.104	18.9 $\times$ 13.2	20.3	0.1	120 $\pm$ 13	74	18	2.9	18.5	6 $\pm$ 3	0.03 $\pm$ 0.013	7.1 $\pm$ 2.7
37	284.031	2.099	38.6 $\times$ 29.9	-40.0	0.2	404 $\pm$ 48	69	17	2.9	18.7	21 $\pm$ 9	0.02 $\pm$ 0.009	5.1 $\pm$ 2.0
38	284.085	2.112	34.4 $\times$ 9.6	-34.3	0.1	152 $\pm$ 19	70	13	2.9	18.6	8 $\pm$ 3	0.03 $\pm$ 0.013	6.8 $\pm$ 2.7
39	284.044	2.126	23.1 $\times$ 18.2	50.0	0.1	168 $\pm$ 22	60	14	2.9	18.4	9 $\pm$ 4	0.03 $\pm$ 0.011	6.0 $\pm$ 2.4
40	284.103	2.114	57.0 $\times$ 19.9	6.9	0.2	138 $\pm$ 23	57	11	2.9	18.9	7 $\pm$ 3	0.01 $\pm$ 0.003	1.8 $\pm$ 0.7
41	283.821	2.132	42.1 $\times$ 25.1	80.8	0.2	960 $\pm$ 96	239	41	2.1	20.0	23 $\pm$ 10	0.06 $\pm$ 0.022	12.0 $\pm$ 4.6
42	283.813	2.134	34.0 $\times$ 17.8	-51.4	0.1	533 $\pm$ 53	157	25	2.1	19.9	13 $\pm$ 6	0.05 $\pm$ 0.021	11.7 $\pm$ 4.5
43	283.912	2.127	34.9 $\times$ 9.0	-54.3	0.1	111 $\pm$ 15	55	13	2.1	18.8	3 $\pm$ 1	0.02 $\pm$ 0.01	5.1 $\pm$ 2.0
44	283.913	2.133	33.5 $\times$ 13.6	86.3	0.1	109 $\pm$ 17	51	12	2.1	18.8	3 $\pm$ 1	0.02 $\pm$ 0.007	3.5 $\pm$ 1.4
45	283.921	2.110	81.2 $\times$ 36.6	29.3	0.3	678 $\pm$ 97	96	23	2.1	18.7	18 $\pm$ 8	0.02 $\pm$ 0.006	3.3 $\pm$ 1.3
46	284.376	2.115	46.6 $\times$ 36.6	4.9	0.3	880 $\pm$ 104	116	22	2.9	18.1	47 $\pm$ 21	0.04 $\pm$ 0.015	8.0 $\pm$ 3.2
47	284.378	2.124	51.1 $\times$ 42.5	-27.0	0.3	789 $\pm$ 89	118	23	2.9	18.7	40 $\pm$ 18	0.03 $\pm$ 0.01	5.3 $\pm$ 2.1
48	284.379	2.131	43.9 $\times$ 19.7	-36.3	0.2	307 $\pm$ 35	82	16	2.9	18.5	16 $\pm$ 7	0.02 $\pm$ 0.01	5.3 $\pm$ 2.1
49	284.386	2.120	21.9 $\times$ 16.6	20.0	0.1	164 $\pm$ 21	71	13	2.9	20.0	8 $\pm$ 3	0.03 $\pm$ 0.011	6.0 $\pm$ 2.4
50	284.373	2.093	25.5 $\times$ 16.5	85.3	0.1	174 $\pm$ 26	70	12	2.9	17.9	9 $\pm$ 4	0.03 $\pm$ 0.012	6.5 $\pm$ 2.6
51	284.371	2.080	46.6 $\times$ 14.1	80.4	0.2	201 $\pm$ 32	84	14	2.9	17.9	11 $\pm$ 5	0.02 $\pm$ 0.009	4.8 $\pm$ 2.0
52	283.957	2.146	23.0 $\times$ 11.6	81.2	0.1	82 $\pm$ 13	48	12	2.1	18.9	2 $\pm$ 1	0.02 $\pm$ 0.008	4.5 $\pm$ 1.8
53	284.081	2.147	24.7 $\times$ 21.3	-2.7	0.2	244 $\pm$ 33	72	15	2.9	18.1	13 $\pm$ 6	0.03 $\pm$ 0.013	7.1 $\pm$ 2.8
54	284.042	2.150	19.3 $\times$ 14.0	17.7	0.1	68 $\pm$ 12	39	9	2.9	19.1	3 $\pm$ 2	0.02 $\pm$ 0.007	3.6 $\pm$ 1.5
55	284.019	2.147	52.0 $\times$ 32.9	-9.4	0.3	898 $\pm$ 98	125	30	2.9	18.8	45 $\pm$ 20	0.04 $\pm$ 0.014	7.6 $\pm$ 3.0
56	284.193	2.102	54.6 $\times$ 45.6	49.6	0.4	1359 $\pm$ 160	137	23	2.9	18.2	72 $\pm$ 32	0.04 $\pm$ 0.015	8.3 $\pm$ 3.3

**Table B2** *continued*

**Table B2** (*continued*)

ID	RA	Dec	Size	PA	R	Flux	$F_{\text{peak}}$	SNR	D	T <sub>dust</sub>	Mass	$\Sigma$	N <sub>H<sub>2</sub></sub>
	( $^{\circ}$ )	( $^{\circ}$ )	( $'' \times ''$ )	( $^{\circ}$ )	(pc)	(mJy)	(mJy beam $^{-1}$ )		(kpc)	(K)	(M $_{\odot}$ )	(g cm $^{-2}$ )	( $\times 10^{21} \text{cm}^{-2}$ )
(1)	(2)	(3)	(4)	(5)	(6)	(7)	(8)	(9)	(10)	(11)	(12)	(13)	(14)
57	284.222	2.136	33.6 $\times$ 18.8	-12.3	0.2	287 $\pm$ 30	85	18	2.9	18.1	15 $\pm$ 7	0.03 $\pm$ 0.013	7.0 $\pm$ 2.7
58	284.227	2.138	23.6 $\times$ 18.0	0.9	0.2	196 $\pm$ 21	81	18	2.9	18.1	11 $\pm$ 5	0.03 $\pm$ 0.013	7.1 $\pm$ 2.8
59	284.222	2.127	25.4 $\times$ 17.7	-64.9	0.2	266 $\pm$ 29	98	20	2.9	18.0	14 $\pm$ 6	0.04 $\pm$ 0.017	9.2 $\pm$ 3.6
60	284.211	2.140	40.0 $\times$ 24.0	-9.6	0.2	425 $\pm$ 54	78	16	2.9	18.2	23 $\pm$ 10	0.03 $\pm$ 0.012	6.8 $\pm$ 2.7
61	284.210	2.121	39.2 $\times$ 25.9	-67.3	0.2	327 $\pm$ 47	65	13	2.9	18.5	17 $\pm$ 8	0.02 $\pm$ 0.009	4.8 $\pm$ 1.9
62	284.210	2.106	27.1 $\times$ 22.8	18.2	0.2	226 $\pm$ 33	66	12	2.9	18.5	12 $\pm$ 5	0.03 $\pm$ 0.01	5.4 $\pm$ 2.2
63	284.232	2.149	46.4 $\times$ 31.3	-73.8	0.3	211 $\pm$ 34	51	11	2.9	18.3	11 $\pm$ 5	0.01 $\pm$ 0.004	2.2 $\pm$ 0.9
64	283.892	2.153	28.8 $\times$ 16.4	-58.0	0.1	81 $\pm$ 15	33	8	2.1	18.7	2 $\pm$ 1	0.01 $\pm$ 0.005	2.5 $\pm$ 1.0
65	284.064	2.169	38.1 $\times$ 24.5	28.6	0.2	381 $\pm$ 52	85	18	2.9	18.4	20 $\pm$ 9	0.03 $\pm$ 0.011	6.1 $\pm$ 2.4
66	283.796	2.157	26.8 $\times$ 13.7	42.4	0.2	199 $\pm$ 26	118	15	5.1	19.0	31 $\pm$ 14	0.04 $\pm$ 0.014	7.8 $\pm$ 3.1
67	283.799	2.161	32.3 $\times$ 17.3	46.7	0.3	331 $\pm$ 43	115	15	5.1	18.0	55 $\pm$ 25	0.04 $\pm$ 0.017	9.2 $\pm$ 3.7
68	283.809	2.166	23.0 $\times$ 16.3	9.3	0.2	212 $\pm$ 29	90	13	5.1	17.6	37 $\pm$ 16	0.04 $\pm$ 0.017	9.1 $\pm$ 3.6
69	283.835	2.177	87.6 $\times$ 36.4	-39.3	0.7	853 $\pm$ 116	93	16	5.1	17.4	151 $\pm$ 68	0.02 $\pm$ 0.008	4.4 $\pm$ 1.8
70	283.856	2.179	22.8 $\times$ 16.1	-62.2	0.2	106 $\pm$ 16	67	13	5.1	17.8	18 $\pm$ 8	0.02 $\pm$ 0.009	4.6 $\pm$ 1.9
71	283.822	2.182	19.8 $\times$ 16.0	24.7	0.2	154 $\pm$ 22	93	15	5.1	17.5	27 $\pm$ 12	0.04 $\pm$ 0.015	7.9 $\pm$ 3.2
72	284.185	2.162	21.8 $\times$ 16.3	56.6	0.1	232 $\pm$ 21	101	19	2.9	18.0	13 $\pm$ 5	0.05 $\pm$ 0.018	10.1 $\pm$ 3.9
73	284.173	2.167	65.3 $\times$ 44.1	-2.5	0.4	3863 $\pm$ 311	951	181	2.9	18.5	200 $\pm$ 87	0.09 $\pm$ 0.036	20.0 $\pm$ 7.7
74	284.176	2.181	21.1 $\times$ 9.7	1.9	0.1	94 $\pm$ 12	59	11	2.9	18.4	5 $\pm$ 2	0.03 $\pm$ 0.013	6.8 $\pm$ 2.7
75	284.179	2.188	34.8 $\times$ 27.0	52.3	0.2	283 $\pm$ 44	57	11	2.9	18.3	15 $\pm$ 7	0.02 $\pm$ 0.009	4.5 $\pm$ 1.8
76	284.046	2.193	21.9 $\times$ 16.6	-22.7	0.1	75 $\pm$ 13	40	9	2.9	18.9	4 $\pm$ 2	0.01 $\pm$ 0.006	3.0 $\pm$ 1.2
77	284.384	2.212	21.3 $\times$ 13.8	-36.4	0.1	86 $\pm$ 14	50	11	2.9	18.9	4 $\pm$ 2	0.02 $\pm$ 0.008	4.2 $\pm$ 1.7
78	284.401	2.200	49.0 $\times$ 26.3	-54.4	0.3	842 $\pm$ 96	162	33	2.9	17.2	49 $\pm$ 22	0.05 $\pm$ 0.02	10.9 $\pm$ 4.2
79	284.407	2.212	33.7 $\times$ 15.3	18.6	0.2	187 $\pm$ 26	73	14	2.9	17.9	10 $\pm$ 5	0.03 $\pm$ 0.011	5.7 $\pm$ 2.3
80	284.419	2.210	31.5 $\times$ 14.2	17.2	0.2	124 $\pm$ 22	53	9	2.9	18.0	7 $\pm$ 3	0.02 $\pm$ 0.008	4.3 $\pm$ 1.8
81	283.906	2.184	65.1 $\times$ 32.5	42.3	0.2	2236 $\pm$ 183	514	118	2.1	17.7	65 $\pm$ 28	0.08 $\pm$ 0.03	16.9 $\pm$ 6.5
82	283.897	2.197	34.8 $\times$ 24.0	-82.2	0.2	493 $\pm$ 49	116	26	2.1	17.4	15 $\pm$ 6	0.05 $\pm$ 0.017	9.7 $\pm$ 3.7
83	283.894	2.187	17.4 $\times$ 13.0	67.6	0.1	140 $\pm$ 13	85	18	2.1	17.6	4 $\pm$ 2	0.05 $\pm$ 0.018	10.0 $\pm$ 3.9
84	283.868	2.196	17.7 $\times$ 16.1	50.5	0.2	102 $\pm$ 16	49	10	5.1	17.4	18 $\pm$ 8	0.03 $\pm$ 0.011	5.9 $\pm$ 2.4
85	283.872	2.202	30.3 $\times$ 16.9	82.8	0.3	141 $\pm$ 23	54	11	5.1	17.4	25 $\pm$ 11	0.02 $\pm$ 0.009	4.5 $\pm$ 1.8
86	283.884	2.192	36.9 $\times$ 14.2	46.3	0.1	175 $\pm$ 26	51	11	2.1	17.6	5 $\pm$ 2	0.02 $\pm$ 0.01	5.3 $\pm$ 2.1
87	283.882	2.219	63.6 $\times$ 22.8	73.7	0.5	210 $\pm$ 35	52	11	5.1	17.5	37 $\pm$ 17	0.01 $\pm$ 0.004	2.3 $\pm$ 0.9
88	283.902	2.230	32.0 $\times$ 16.7	87.8	0.3	222 $\pm$ 30	60	13	5.1	17.8	38 $\pm$ 17	0.03 $\pm$ 0.012	6.6 $\pm$ 2.6
89	283.849	2.237	25.1 $\times$ 19.9	61.5	0.2	129 $\pm$ 21	67	11	2.9	17.3	7 $\pm$ 3	0.02 $\pm$ 0.008	4.3 $\pm$ 1.8
90	284.287	2.132	33.5 $\times$ 26.7	-83.4	0.2	2557 $\pm$ 158	447	108	2.1	17.4	179 $\pm$ 77	0.27 $\pm$ 0.102	57.4 $\pm$ 21.7
91	284.286	2.140	18.7 $\times$ 17.0	-1.1	0.1	1115 $\pm$ 69	508	115	2.9	15.3	78 $\pm$ 34	0.33 $\pm$ 0.126	70.6 $\pm$ 26.9
92	284.279	2.141	51.2 $\times$ 26.5	67.1	0.3	2794 $\pm$ 184	525	119	2.9	15.6	190 $\pm$ 83	0.19 $\pm$ 0.071	40.1 $\pm$ 15.1
93	284.297	2.125	48.9 $\times$ 30.8	71.5	0.3	3369 $\pm$ 222	479	107	2.9	15.2	238 $\pm$ 102	0.21 $\pm$ 0.081	45.4 $\pm$ 17.2
94	284.284	2.154	50.8 $\times$ 30.2	82.3	0.3	3562 $\pm$ 227	515	117	2.9	16.1	230 $\pm$ 99	0.2 $\pm$ 0.076	43.1 $\pm$ 16.3
95	284.283	2.182	103.2 $\times$ 41.4	77.2	0.5	9121 $\pm$ 613	633	145	2.9	16.2	581 $\pm$ 251	0.18 $\pm$ 0.069	39.0 $\pm$ 14.8
96	284.276	2.204	24.1 $\times$ 8.7	61.0	0.1	399 $\pm$ 25	265	60	2.9	16.5	25 $\pm$ 11	0.16 $\pm$ 0.06	33.7 $\pm$ 12.8
97	284.297	2.105	44.8 $\times$ 30.1	63.6	0.3	1430 $\pm$ 115	175	40	2.9	16.4	89 $\pm$ 39	0.09 $\pm$ 0.034	19.0 $\pm$ 7.2
98	284.236	2.084	24.6 $\times$ 14.5	-49.7	0.1	303 $\pm$ 28	146	27	2.9	19.6	14 $\pm$ 6	0.05 $\pm$ 0.021	11.6 $\pm$ 4.4
99	284.246	2.083	48.5 $\times$ 31.1	-36.8	0.3	2510 $\pm$ 193	675	127	2.9	19.3	122 $\pm$ 53	0.11 $\pm$ 0.041	23.2 $\pm$ 8.8

**Table B2** *continued*

**Table B2** (*continued*)

ID	RA	Dec	Size	PA	R	Flux	$F_{\text{peak}}$	SNR	D	T <sub>dust</sub>	Mass	$\Sigma$	N <sub>H2</sub>
	( $^{\circ}$ )	( $^{\circ}$ )	( $'' \times ''$ )	( $^{\circ}$ )	(pc)	(mJy)	(mJy beam $^{-1}$ )		(kpc)	(K)	(M $_{\odot}$ )	(g cm $^{-2}$ )	( $\times 10^{21} \text{cm}^{-2}$ )
(1)	(2)	(3)	(4)	(5)	(6)	(7)	(8)	(9)	(10)	(11)	(12)	(13)	(14)
100	284.301	2.147	55.6 $\times$ 46.7	44.2	0.4	2146 $\pm$ 179	256	58	2.9	17.2	124 $\pm$ 54	0.06 $\pm$ 0.025	13.7 $\pm$ 5.3
101	284.237	2.074	32.8 $\times$ 19.9	70.9	0.2	399 $\pm$ 45	105	18	2.9	18.0	22 $\pm$ 10	0.04 $\pm$ 0.017	9.4 $\pm$ 3.7
102	284.322	2.155	75.3 $\times$ 44.0	-45.8	0.4	1771 $\pm$ 179	121	28	2.9	17.4	101 $\pm$ 45	0.04 $\pm$ 0.016	8.8 $\pm$ 3.4
103	284.263	2.089	33.2 $\times$ 19.1	12.8	0.2	465 $\pm$ 45	109	21	2.9	17.6	26 $\pm$ 11	0.06 $\pm$ 0.021	11.8 $\pm$ 4.5
104	284.295	2.205	53.8 $\times$ 35.1	55.7	0.3	1080 $\pm$ 102	119	27	2.9	17.9	59 $\pm$ 26	0.04 $\pm$ 0.016	9.0 $\pm$ 3.5
105	284.270	2.110	82.0 $\times$ 54.9	-59.6	0.5	3988 $\pm$ 308	842	184	2.9	18.5	207 $\pm$ 90	0.06 $\pm$ 0.024	13.2 $\pm$ 5.0
106	284.327	2.145	40.2 $\times$ 28.3	32.2	0.2	691 $\pm$ 68	110	25	2.9	17.1	40 $\pm$ 18	0.05 $\pm$ 0.019	10.2 $\pm$ 3.9
107	284.229	2.200	37.2 $\times$ 18.9	10.3	0.2	315 $\pm$ 36	74	17	2.9	18.0	17 $\pm$ 8	0.03 $\pm$ 0.013	7.0 $\pm$ 2.7
108	284.237	2.208	51.7 $\times$ 26.5	88.1	0.3	584 $\pm$ 66	86	20	2.9	17.8	32 $\pm$ 14	0.03 $\pm$ 0.012	6.7 $\pm$ 2.6
109	284.238	2.186	25.1 $\times$ 15.0	32.8	0.1	161 $\pm$ 19	76	17	2.9	17.9	9 $\pm$ 4	0.03 $\pm$ 0.012	6.7 $\pm$ 2.6
110	284.234	2.191	29.3 $\times$ 23.9	-41.9	0.2	296 $\pm$ 35	70	16	2.9	17.8	16 $\pm$ 7	0.03 $\pm$ 0.012	6.7 $\pm$ 2.6
111	284.261	2.202	77.8 $\times$ 54.1	-80.2	0.5	2095 $\pm$ 200	185	42	2.9	17.9	114 $\pm$ 50	0.04 $\pm$ 0.014	7.8 $\pm$ 3.0
112	284.252	2.207	22.7 $\times$ 13.6	14.7	0.1	122 $\pm$ 14	68	15	2.9	17.9	7 $\pm$ 3	0.03 $\pm$ 0.011	6.2 $\pm$ 2.4
113	284.259	2.225	38.5 $\times$ 18.0	29.4	0.2	260 $\pm$ 30	68	16	2.9	18.1	14 $\pm$ 6	0.03 $\pm$ 0.011	5.8 $\pm$ 2.3
114	284.247	2.226	43.6 $\times$ 28.8	-57.5	0.3	460 $\pm$ 58	73	17	2.9	18.2	24 $\pm$ 11	0.03 $\pm$ 0.01	5.6 $\pm$ 2.2
115	284.241	2.222	25.5 $\times$ 9.5	-54.2	0.1	111 $\pm$ 12	72	16	2.9	18.1	6 $\pm$ 3	0.03 $\pm$ 0.013	7.1 $\pm$ 2.8
116	284.216	2.188	45.9 $\times$ 30.1	-80.7	0.3	477 $\pm$ 60	83	18	2.9	17.8	26 $\pm$ 12	0.03 $\pm$ 0.01	5.5 $\pm$ 2.2
117	284.250	2.118	41.4 $\times$ 27.4	34.0	0.2	579 $\pm$ 65	97	21	2.9	18.5	30 $\pm$ 13	0.04 $\pm$ 0.014	7.6 $\pm$ 3.0
118	284.252	2.195	45.6 $\times$ 33.4	3.7	0.3	622 $\pm$ 74	92	21	2.9	17.9	34 $\pm$ 15	0.03 $\pm$ 0.012	6.4 $\pm$ 2.5
119	284.307	2.090	28.4 $\times$ 19.4	60.2	0.2	228 $\pm$ 30	69	14	2.9	17.1	13 $\pm$ 6	0.03 $\pm$ 0.013	6.9 $\pm$ 2.7
120	284.227	2.054	40.3 $\times$ 38.2	30.3	0.3	547 $\pm$ 82	89	13	2.9	18.0	30 $\pm$ 13	0.03 $\pm$ 0.01	5.5 $\pm$ 2.2
121	284.244	2.202	22.2 $\times$ 15.9	-87.8	0.1	168 $\pm$ 19	63	14	2.9	17.8	9 $\pm$ 4	0.04 $\pm$ 0.014	7.5 $\pm$ 2.9
122	284.280	2.084	42.1 $\times$ 24.1	-61.4	0.2	372 $\pm$ 52	81	16	2.9	17.6	21 $\pm$ 9	0.03 $\pm$ 0.011	5.9 $\pm$ 2.3
123	284.338	2.154	34.4 $\times$ 13.8	-60.6	0.2	195 $\pm$ 25	70	16	2.9	17.4	11 $\pm$ 5	0.03 $\pm$ 0.012	6.7 $\pm$ 2.6
124	284.308	2.106	27.5 $\times$ 14.8	41.6	0.1	139 $\pm$ 18	79	17	2.9	17.2	8 $\pm$ 4	0.03 $\pm$ 0.011	5.7 $\pm$ 2.3
125	284.361	2.160	86.7 $\times$ 39.2	23.5	0.4	1004 $\pm$ 127	86	19	2.9	17.7	56 $\pm$ 25	0.02 $\pm$ 0.009	4.7 $\pm$ 1.8
126	284.248	2.165	26.8 $\times$ 17.7	-47.4	0.2	174 $\pm$ 25	63	14	2.9	18.0	9 $\pm$ 4	0.03 $\pm$ 0.011	5.7 $\pm$ 2.3
127	284.248	2.174	34.4 $\times$ 16.0	71.4	0.2	157 $\pm$ 22	53	12	2.9	18.1	8 $\pm$ 4	0.02 $\pm$ 0.008	4.4 $\pm$ 1.8
128	284.271	2.069	32.0 $\times$ 16.4	-79.8	0.2	191 $\pm$ 28	71	13	2.9	17.5	11 $\pm$ 5	0.03 $\pm$ 0.011	5.9 $\pm$ 2.4
129	284.252	2.175	25.5 $\times$ 12.6	75.0	0.1	109 $\pm$ 15	54	12	2.9	17.9	6 $\pm$ 3	0.02 $\pm$ 0.01	5.3 $\pm$ 2.1
130	284.347	2.142	31.2 $\times$ 18.3	-19.8	0.2	199 $\pm$ 27	64	14	2.9	17.4	11 $\pm$ 5	0.03 $\pm$ 0.011	5.7 $\pm$ 2.3
131	284.353	2.148	28.1 $\times$ 14.7	56.6	0.1	124 $\pm$ 18	50	11	2.9	17.5	7 $\pm$ 3	0.02 $\pm$ 0.009	4.9 $\pm$ 2.0
132	284.297	2.082	25.0 $\times$ 18.9	-58.9	0.2	112 $\pm$ 19	55	11	2.9	17.6	6 $\pm$ 3	0.02 $\pm$ 0.007	3.8 $\pm$ 1.6
133	284.253	2.100	39.1 $\times$ 17.7	42.8	0.2	158 $\pm$ 25	57	12	2.9	18.8	8 $\pm$ 4	0.02 $\pm$ 0.006	3.3 $\pm$ 1.3
134	284.310	2.217	64.2 $\times$ 21.1	-24.3	0.3	555 $\pm$ 65	100	23	2.9	17.8	31 $\pm$ 13	0.03 $\pm$ 0.012	6.4 $\pm$ 2.5
135	284.345	2.149	26.0 $\times$ 13.0	71.6	0.1	76 $\pm$ 11	54	12	2.9	17.5	4 $\pm$ 2	0.02 $\pm$ 0.007	3.6 $\pm$ 1.5
136	284.199	2.192	33.5 $\times$ 19.0	-43.5	0.2	178 $\pm$ 29	56	11	2.9	18.0	9 $\pm$ 4	0.02 $\pm$ 0.008	4.2 $\pm$ 1.7
137	284.207	2.203	33.9 $\times$ 28.5	-71.1	0.2	249 $\pm$ 38	68	14	2.9	18.1	13 $\pm$ 6	0.02 $\pm$ 0.008	4.0 $\pm$ 1.6
138	283.961	2.193	40.2 $\times$ 30.4	-3.9	0.2	1685 $\pm$ 118	410	98	2.1	17.7	49 $\pm$ 21	0.1 $\pm$ 0.039	22.0 $\pm$ 8.3
139	283.962	2.206	63.1 $\times$ 44.5	-38.5	0.3	3223 $\pm$ 243	702	170	2.1	18.8	85 $\pm$ 37	0.08 $\pm$ 0.03	16.7 $\pm$ 6.4
140	283.970	2.175	49.6 $\times$ 32.6	39.1	0.2	1273 $\pm$ 107	201	48	2.1	18.1	36 $\pm$ 16	0.06 $\pm$ 0.022	12.1 $\pm$ 4.6
141	283.963	2.181	46.8 $\times$ 23.9	-11.9	0.2	1028 $\pm$ 81	173	41	2.1	17.9	29 $\pm$ 13	0.07 $\pm$ 0.026	14.4 $\pm$ 5.5
142	284.008	2.212	51.3 $\times$ 20.7	-64.9	0.2	886 $\pm$ 67	137	33	2.9	18.9	45 $\pm$ 19	0.06 $\pm$ 0.021	12.0 $\pm$ 4.6

**Table B2** *continued*

**Table B2** (*continued*)

ID	RA	Dec	Size	PA	R	Flux	$F_{\text{peak}}$	SNR	D	T <sub>dust</sub>	Mass	$\Sigma$	N <sub>H<sub>2</sub></sub>
	( $^{\circ}$ )	( $^{\circ}$ )	( $'' \times ''$ )	( $^{\circ}$ )	(pc)	(mJy)	(mJy beam $^{-1}$ )		(kpc)	(K)	(M $_{\odot}$ )	(g cm $^{-2}$ )	( $\times 10^{21} \text{cm}^{-2}$ )
(1)	(2)	(3)	(4)	(5)	(6)	(7)	(8)	(9)	(10)	(11)	(12)	(13)	(14)
143	284.013	2.229	82.8 $\times$ 66.7	-46.9	0.5	4825 $\pm$ 381	606	137	2.9	18.6	249 $\pm$ 109	0.06 $\pm$ 0.023	12.9 $\pm$ 4.9
144	284.023	2.228	21.3 $\times$ 12.6	-30.0	0.1	246 $\pm$ 18	134	30	2.9	18.3	13 $\pm$ 6	0.06 $\pm$ 0.025	13.8 $\pm$ 5.3
145	283.951	2.189	27.8 $\times$ 15.6	-60.9	0.1	315 $\pm$ 26	111	26	2.1	18.5	9 $\pm$ 4	0.05 $\pm$ 0.019	10.8 $\pm$ 4.1
146	283.996	2.183	39.8 $\times$ 37.7	71.9	0.3	873 $\pm$ 84	120	28	2.9	18.4	46 $\pm$ 20	0.04 $\pm$ 0.016	8.7 $\pm$ 3.4
147	283.993	2.187	45.8 $\times$ 11.2	8.5	0.2	288 $\pm$ 24	111	26	2.9	18.6	15 $\pm$ 6	0.04 $\pm$ 0.015	8.3 $\pm$ 3.2
148	283.998	2.214	44.3 $\times$ 19.5	89.7	0.2	564 $\pm$ 49	102	24	2.9	19.2	28 $\pm$ 12	0.04 $\pm$ 0.016	9.1 $\pm$ 3.5
149	283.985	2.161	24.9 $\times$ 14.4	9.3	0.1	159 $\pm$ 17	82	20	2.1	18.0	5 $\pm$ 2	0.03 $\pm$ 0.013	6.9 $\pm$ 2.7
150	283.969	2.218	21.0 $\times$ 14.3	-10.3	0.1	183 $\pm$ 17	86	21	2.1	19.1	5 $\pm$ 2	0.04 $\pm$ 0.016	8.7 $\pm$ 3.4
151	283.988	2.195	32.6 $\times$ 20.0	-8.9	0.2	373 $\pm$ 34	85	20	2.9	18.8	19 $\pm$ 8	0.04 $\pm$ 0.015	8.3 $\pm$ 3.2
152	283.996	2.202	35.9 $\times$ 9.3	44.9	0.1	183 $\pm$ 17	78	19	2.9	19.1	9 $\pm$ 4	0.04 $\pm$ 0.014	7.7 $\pm$ 3.0
153	283.991	2.199	33.4 $\times$ 7.7	6.3	0.1	135 $\pm$ 13	76	18	2.9	18.9	7 $\pm$ 3	0.04 $\pm$ 0.014	7.6 $\pm$ 2.9
154	283.985	2.152	22.1 $\times$ 16.2	88.2	0.1	126 $\pm$ 16	67	16	2.1	18.2	4 $\pm$ 2	0.03 $\pm$ 0.01	5.4 $\pm$ 2.1
155	283.987	2.207	29.5 $\times$ 24.7	53.8	0.2	329 $\pm$ 34	74	18	2.9	18.8	17 $\pm$ 7	0.03 $\pm$ 0.012	6.6 $\pm$ 2.5
156	283.977	2.210	39.4 $\times$ 24.8	67.2	0.2	393 $\pm$ 45	94	23	2.1	18.8	10 $\pm$ 5	0.03 $\pm$ 0.011	5.9 $\pm$ 2.3
157	283.989	2.169	28.3 $\times$ 12.2	-51.7	0.1	142 $\pm$ 18	66	16	2.9	18.3	8 $\pm$ 3	0.03 $\pm$ 0.012	6.3 $\pm$ 2.5
158	283.977	2.193	23.8 $\times$ 14.2	-49.0	0.1	141 $\pm$ 17	56	13	2.1	18.9	4 $\pm$ 2	0.03 $\pm$ 0.011	6.0 $\pm$ 2.3
159	284.004	2.193	21.5 $\times$ 13.9	-43.2	0.1	117 $\pm$ 15	63	15	2.9	18.6	6 $\pm$ 3	0.03 $\pm$ 0.011	5.8 $\pm$ 2.3
160	283.957	2.164	42.1 $\times$ 32.4	-32.5	0.2	328 $\pm$ 43	72	17	2.1	18.8	9 $\pm$ 4	0.02 $\pm$ 0.006	3.5 $\pm$ 1.4
161	283.981	2.180	39.6 $\times$ 22.3	58.5	0.2	237 $\pm$ 32	57	13	2.1	19.1	6 $\pm$ 3	0.02 $\pm$ 0.007	3.8 $\pm$ 1.5
162	283.943	2.207	33.8 $\times$ 27.2	-17.5	0.2	180 $\pm$ 27	49	12	2.1	18.8	5 $\pm$ 2	0.01 $\pm$ 0.005	2.8 $\pm$ 1.1
163	283.938	2.213	43.0 $\times$ 30.1	66.7	0.2	187 $\pm$ 28	53	13	2.1	18.6	5 $\pm$ 2	0.01 $\pm$ 0.004	2.1 $\pm$ 0.8
164	283.979	2.241	25.6 $\times$ 19.4	17.6	0.2	76 $\pm$ 13	44	11	2.9	19.1	4 $\pm$ 2	0.01 $\pm$ 0.004	2.2 $\pm$ 0.9
165	284.353	2.227	47.5 $\times$ 32.1	-25.1	0.3	760 $\pm$ 81	91	21	2.9	18.1	41 $\pm$ 18	0.04 $\pm$ 0.014	7.7 $\pm$ 3.0
166	284.361	2.203	62.1 $\times$ 30.2	79.1	0.3	1172 $\pm$ 114	153	35	2.9	18.5	61 $\pm$ 26	0.04 $\pm$ 0.017	9.3 $\pm$ 3.6
167	284.342	2.217	22.8 $\times$ 10.0	-14.0	0.1	85 $\pm$ 11	55	13	2.9	18.3	5 $\pm$ 2	0.03 $\pm$ 0.011	5.7 $\pm$ 2.3
168	284.362	2.237	35.3 $\times$ 21.7	-74.9	0.2	197 $\pm$ 30	49	11	2.9	18.3	10 $\pm$ 5	0.02 $\pm$ 0.007	3.9 $\pm$ 1.6
169	284.347	2.207	33.1 $\times$ 25.3	67.5	0.2	208 $\pm$ 33	56	13	2.9	18.6	11 $\pm$ 5	0.02 $\pm$ 0.007	3.7 $\pm$ 1.5
170	284.347	2.191	36.4 $\times$ 28.9	18.5	0.2	366 $\pm$ 52	62	14	2.9	18.6	19 $\pm$ 9	0.02 $\pm$ 0.01	5.1 $\pm$ 2.0
171	284.347	2.240	31.1 $\times$ 22.5	35.9	0.2	142 $\pm$ 23	45	10	2.9	18.3	8 $\pm$ 3	0.01 $\pm$ 0.006	3.1 $\pm$ 1.3
172	283.954	2.244	21.6 $\times$ 13.1	24.5	0.1	56 $\pm$ 9	43	10	2.9	18.8	3 $\pm$ 1	0.01 $\pm$ 0.005	2.9 $\pm$ 1.2
173	283.943	2.234	70.3 $\times$ 13.6	-75.1	0.2	112 $\pm$ 19	46	11	2.9	18.8	6 $\pm$ 3	0.01 $\pm$ 0.003	1.7 $\pm$ 0.7
174	284.327	2.241	28.3 $\times$ 21.8	-41.2	0.2	245 $\pm$ 34	67	15	2.9	17.9	13 $\pm$ 6	0.03 $\pm$ 0.012	6.2 $\pm$ 2.5
175	284.333	2.249	20.3 $\times$ 18.0	-63.3	0.1	116 $\pm$ 17	63	14	2.9	18.0	6 $\pm$ 3	0.02 $\pm$ 0.009	4.9 $\pm$ 2.0
176	283.845	2.260	32.1 $\times$ 13.8	-79.0	0.2	226 $\pm$ 32	112	16	2.9	17.7	13 $\pm$ 6	0.04 $\pm$ 0.015	8.1 $\pm$ 3.2
177	284.132	2.269	34.3 $\times$ 25.7	55.3	0.2	608 $\pm$ 80	120	15	2.9	19.3	30 $\pm$ 13	0.05 $\pm$ 0.018	9.6 $\pm$ 3.8
178	284.174	2.226	65.3 $\times$ 34.9	-20.1	0.3	1850 $\pm$ 184	193	35	2.9	17.4	106 $\pm$ 46	0.06 $\pm$ 0.024	13.3 $\pm$ 5.1
179	284.164	2.243	67.3 $\times$ 52.8	8.6	0.4	3301 $\pm$ 327	207	33	2.9	18.5	172 $\pm$ 75	0.07 $\pm$ 0.025	13.9 $\pm$ 5.4
180	284.154	2.264	41.6 $\times$ 34.8	1.4	0.3	832 $\pm$ 107	130	19	2.9	18.6	43 $\pm$ 19	0.04 $\pm$ 0.016	8.5 $\pm$ 3.4
181	284.407	2.269	26.7 $\times$ 16.7	-64.4	0.2	161 $\pm$ 26	61	10	2.9	18.5	8 $\pm$ 4	0.03 $\pm$ 0.01	5.4 $\pm$ 2.2
182	284.390	2.253	26.1 $\times$ 17.3	-63.8	0.2	145 $\pm$ 24	45	9	2.9	18.1	8 $\pm$ 4	0.02 $\pm$ 0.009	4.9 $\pm$ 2.0
183	283.841	2.284	34.0 $\times$ 18.8	73.9	0.2	427 $\pm$ 60	137	17	2.9	17.8	23 $\pm$ 11	0.05 $\pm$ 0.02	10.6 $\pm$ 4.2
184	283.832	2.273	34.3 $\times$ 27.7	44.7	0.2	470 $\pm$ 75	118	14	2.9	17.4	27 $\pm$ 12	0.04 $\pm$ 0.015	8.1 $\pm$ 3.3
185	283.955	2.273	61.2 $\times$ 33.4	87.6	0.3	1342 $\pm$ 143	127	27	2.9	18.4	70 $\pm$ 31	0.05 $\pm$ 0.018	9.9 $\pm$ 3.8

**Table B2** *continued*

**Table B2** (*continued*)

ID	RA	Dec	Size	PA	R	Flux	$F_{\text{peak}}$	SNR	D	T <sub>dust</sub>	Mass	$\Sigma$	N <sub>H<sub>2</sub></sub>
	( $^{\circ}$ )	( $^{\circ}$ )	( $'' \times ''$ )	( $^{\circ}$ )	(pc)	(mJy)	(mJy beam $^{-1}$ )		(kpc)	(K)	(M $_{\odot}$ )	(g cm $^{-2}$ )	( $\times 10^{21} \text{cm}^{-2}$ )
(1)	(2)	(3)	(4)	(5)	(6)	(7)	(8)	(9)	(10)	(11)	(12)	(13)	(14)
186	283.967	2.292	$28.9 \times 10.6$	-12.8	0.1	$166 \pm 17$	89	18	2.9	18.5	$9 \pm 4$	$0.04 \pm 0.015$	$8.1 \pm 3.1$
187	283.974	2.295	$43.6 \times 23.3$	-41.3	0.2	$456 \pm 52$	101	20	2.9	18.3	$24 \pm 11$	$0.03 \pm 0.013$	$6.8 \pm 2.7$
188	283.970	2.264	$65.7 \times 31.0$	88.9	0.3	$927 \pm 100$	96	20	2.9	19.0	$46 \pm 20$	$0.03 \pm 0.012$	$6.5 \pm 2.5$
189	283.960	2.298	$32.0 \times 10.9$	13.3	0.1	$130 \pm 17$	67	12	2.9	18.8	$7 \pm 3$	$0.03 \pm 0.01$	$5.4 \pm 2.1$
190	283.954	2.303	$36.7 \times 27.3$	-1.7	0.2	$217 \pm 35$	70	13	2.9	18.8	$11 \pm 5$	$0.01 \pm 0.006$	$3.1 \pm 1.3$
191	284.318	2.304	$27.8 \times 12.5$	-58.8	0.1	$215 \pm 26$	93	19	2.9	18.0	$12 \pm 5$	$0.05 \pm 0.018$	$9.7 \pm 3.8$
192	284.082	2.285	$40.4 \times 31.3$	6.6	0.3	$2138 \pm 168$	340	40	2.9	18.9	$107 \pm 46$	$0.11 \pm 0.044$	$24.3 \pm 9.3$
193	284.070	2.285	$68.3 \times 21.1$	19.7	0.3	$3136 \pm 224$	391	52	2.9	19.9	$145 \pm 63$	$0.14 \pm 0.052$	$29.0 \pm 11.1$
194	284.110	2.215	$42.2 \times 18.5$	66.3	0.2	$826 \pm 65$	244	40	2.9	17.0	$49 \pm 21$	$0.08 \pm 0.032$	$17.9 \pm 6.8$
195	284.104	2.220	$34.6 \times 12.2$	52.0	0.1	$508 \pm 39$	222	35	2.9	17.1	$30 \pm 13$	$0.09 \pm 0.036$	$20.1 \pm 7.7$
196	284.044	2.277	$94.7 \times 79.7$	-5.6	0.6	$11650 \pm 910$	591	102	2.9	19.7	$549 \pm 239$	$0.1 \pm 0.037$	$20.9 \pm 7.9$
197	284.043	2.291	$22.4 \times 9.7$	-80.9	0.1	$272 \pm 20$	183	29	2.9	19.7	$13 \pm 6$	$0.08 \pm 0.03$	$16.9 \pm 6.4$
198	284.066	2.263	$37.0 \times 22.3$	78.4	0.2	$1233 \pm 99$	299	46	2.9	18.0	$67 \pm 29$	$0.11 \pm 0.042$	$23.3 \pm 8.9$
199	284.102	2.285	$38.4 \times 27.1$	0.4	0.2	$1005 \pm 112$	249	28	2.9	18.9	$51 \pm 22$	$0.07 \pm 0.026$	$14.0 \pm 5.5$
200	284.099	2.234	$38.4 \times 13.1$	43.5	0.2	$412 \pm 36$	156	24	2.9	18.2	$22 \pm 10$	$0.06 \pm 0.023$	$12.5 \pm 4.8$
201	284.096	2.243	$49.8 \times 24.7$	81.7	0.3	$1163 \pm 115$	222	32	2.9	19.0	$58 \pm 25$	$0.06 \pm 0.025$	$13.5 \pm 5.2$
202	284.098	2.291	$47.4 \times 14.0$	87.9	0.2	$410 \pm 52$	139	14	2.9	19.2	$20 \pm 9$	$0.04 \pm 0.016$	$8.7 \pm 3.4$
203	284.080	2.268	$19.9 \times 16.8$	33.0	0.1	$329 \pm 34$	149	21	2.9	18.0	$18 \pm 8$	$0.07 \pm 0.028$	$15.3 \pm 5.9$
204	284.078	2.273	$21.5 \times 15.6$	-12.4	0.1	$317 \pm 31$	133	18	2.9	18.2	$17 \pm 7$	$0.07 \pm 0.026$	$14.5 \pm 5.6$
205	284.087	2.272	$24.5 \times 17.6$	-83.2	0.2	$404 \pm 43$	180	23	2.9	17.6	$23 \pm 10$	$0.07 \pm 0.028$	$15.1 \pm 5.9$
206	284.077	2.256	$41.0 \times 28.2$	59.4	0.2	$861 \pm 93$	147	22	2.9	18.2	$46 \pm 20$	$0.05 \pm 0.021$	$11.4 \pm 4.4$
207	284.040	2.255	$28.1 \times 17.4$	-86.4	0.2	$370 \pm 34$	110	21	2.9	20.0	$17 \pm 7$	$0.05 \pm 0.018$	$10.0 \pm 3.9$
208	284.006	2.277	$62.4 \times 27.6$	72.9	0.3	$1151 \pm 114$	130	26	2.9	19.2	$56 \pm 25$	$0.04 \pm 0.017$	$9.4 \pm 3.6$
209	284.013	2.273	$45.2 \times 20.1$	67.8	0.2	$629 \pm 57$	113	23	2.9	19.5	$30 \pm 13$	$0.04 \pm 0.017$	$9.5 \pm 3.7$
210	284.078	2.247	$27.2 \times 12.8$	-50.7	0.1	$254 \pm 27$	110	17	2.9	18.7	$13 \pm 6$	$0.05 \pm 0.02$	$10.6 \pm 4.1$
211	284.130	2.183	$63.1 \times 52.3$	-41.4	0.4	$2226 \pm 235$	135	25	2.9	18.1	$119 \pm 53$	$0.05 \pm 0.019$	$10.3 \pm 4.0$
212	284.062	2.247	$37.2 \times 22.2$	-74.9	0.2	$802 \pm 77$	218	37	2.9	18.3	$42 \pm 18$	$0.07 \pm 0.027$	$14.6 \pm 5.6$
213	284.070	2.244	$28.6 \times 14.0$	-46.3	0.1	$286 \pm 32$	107	18	2.9	18.3	$15 \pm 7$	$0.05 \pm 0.02$	$10.9 \pm 4.2$
214	284.084	2.300	$42.1 \times 20.4$	18.8	0.2	$250 \pm 40$	104	11	2.9	19.0	$13 \pm 6$	$0.02 \pm 0.008$	$4.2 \pm 1.7$
215	284.134	2.199	$32.5 \times 22.0$	82.8	0.2	$484 \pm 55$	113	20	2.9	18.1	$26 \pm 11$	$0.05 \pm 0.019$	$10.5 \pm 4.1$
216	284.112	2.253	$53.5 \times 29.7$	-73.5	0.3	$656 \pm 82$	141	20	2.9	18.3	$35 \pm 15$	$0.03 \pm 0.012$	$6.2 \pm 2.4$
217	284.118	2.207	$32.0 \times 18.8$	31.1	0.2	$279 \pm 35$	88	15	2.9	17.8	$15 \pm 7$	$0.03 \pm 0.014$	$7.4 \pm 2.9$
218	284.085	2.235	$45.3 \times 30.6$	58.6	0.3	$521 \pm 78$	90	14	2.9	19.0	$26 \pm 12$	$0.03 \pm 0.01$	$5.3 \pm 2.1$
219	284.021	2.308	$27.3 \times 24.6$	6.1	0.2	$334 \pm 48$	77	13	2.9	18.9	$17 \pm 8$	$0.03 \pm 0.013$	$7.2 \pm 2.9$
220	284.114	2.278	$32.3 \times 11.0$	38.7	0.1	$86 \pm 16$	80	9	2.9	19.3	$4 \pm 2$	$0.02 \pm 0.007$	$3.4 \pm 1.4$
221	284.111	2.238	$42.8 \times 38.2$	-18.1	0.3	$176 \pm 28$	79	12	2.9	18.9	$9 \pm 4$	$0.01 \pm 0.003$	$1.5 \pm 0.6$
222	284.112	2.195	$93.7 \times 28.3$	71.3	0.4	$498 \pm 71$	97	17	2.9	18.2	$27 \pm 12$	$0.01 \pm 0.005$	$2.9 \pm 1.2$
223	283.990	2.311	$25.9 \times 16.8$	-61.6	0.2	$171 \pm 26$	68	12	2.9	19.2	$8 \pm 4$	$0.03 \pm 0.011$	$5.5 \pm 2.2$
224	283.830	2.322	$38.7 \times 20.7$	38.9	0.2	$760 \pm 99$	176	19	2.9	17.3	$44 \pm 19$	$0.07 \pm 0.029$	$15.6 \pm 6.2$
225	284.000	2.325	$21.5 \times 14.4$	-58.7	0.1	$82 \pm 15$	55	9	2.9	19.4	$4 \pm 2$	$0.02 \pm 0.007$	$3.7 \pm 1.5$
226	284.330	2.326	$29.1 \times 25.5$	-48.1	0.2	$666 \pm 69$	156	27	2.9	19.4	$32 \pm 14$	$0.06 \pm 0.023$	$12.4 \pm 4.8$
227	284.385	2.327	$42.2 \times 15.6$	-60.6	0.2	$208 \pm 35$	74	10	2.9	18.2	$11 \pm 5$	$0.02 \pm 0.009$	$4.8 \pm 2.0$
228	284.303	2.260	$56.6 \times 30.4$	47.9	0.3	$1287 \pm 95$	202	46	2.9	16.6	$79 \pm 34$	$0.06 \pm 0.023$	$13.2 \pm 5.0$

**Table B2** *continued*

**Table B2** (*continued*)

ID	RA	Dec	Size	PA	R	Flux	$F_{\text{peak}}$	SNR	D	T <sub>dust</sub>	Mass	$\Sigma$	N <sub>H<sub>2</sub></sub>
	( $^{\circ}$ )	( $^{\circ}$ )	( $'' \times ''$ )	( $^{\circ}$ )	(pc)	(mJy)	(mJy beam $^{-1}$ )		(kpc)	(K)	(M $_{\odot}$ )	(g cm $^{-2}$ )	( $\times 10^{21} \text{cm}^{-2}$ )
(1)	(2)	(3)	(4)	(5)	(6)	(7)	(8)	(9)	(10)	(11)	(12)	(13)	(14)
229	284.297	2.269	71.0 $\times$ 47.9	-38.9	0.4	3358 $\pm$ 259	313	70	2.9	16.5	209 $\pm$ 91	0.08 $\pm$ 0.032	17.6 $\pm$ 6.8
230	284.190	2.302	31.6 $\times$ 23.1	11.6	0.2	813 $\pm$ 71	189	29	2.9	18.6	42 $\pm$ 18	0.08 $\pm$ 0.03	16.5 $\pm$ 6.3
231	284.183	2.310	42.7 $\times$ 30.0	-20.2	0.3	1382 $\pm$ 128	252	35	2.9	19.0	69 $\pm$ 30	0.07 $\pm$ 0.028	15.4 $\pm$ 5.9
232	284.177	2.319	37.3 $\times$ 26.5	-81.6	0.2	1183 $\pm$ 114	227	28	2.9	20.5	53 $\pm$ 23	0.07 $\pm$ 0.028	15.3 $\pm$ 5.9
233	284.312	2.261	40.2 $\times$ 26.0	-38.9	0.2	955 $\pm$ 74	165	37	2.9	16.9	57 $\pm$ 24	0.07 $\pm$ 0.028	15.7 $\pm$ 6.0
234	284.304	2.248	29.1 $\times$ 11.3	-56.2	0.1	387 $\pm$ 28	144	33	2.9	17.3	22 $\pm$ 10	0.09 $\pm$ 0.035	19.4 $\pm$ 7.4
235	284.164	2.318	38.8 $\times$ 26.1	5.4	0.2	1645 $\pm$ 162	372	41	2.9	18.2	87 $\pm$ 38	0.12 $\pm$ 0.045	24.8 $\pm$ 9.6
236	284.281	2.270	83.2 $\times$ 34.3	56.9	0.4	2548 $\pm$ 199	435	97	2.9	17.0	150 $\pm$ 65	0.07 $\pm$ 0.027	15.1 $\pm$ 5.7
237	284.258	2.284	80.1 $\times$ 44.9	46.8	0.4	4264 $\pm$ 331	544	115	2.9	18.3	224 $\pm$ 97	0.08 $\pm$ 0.032	17.9 $\pm$ 6.8
238	284.251	2.297	25.1 $\times$ 14.0	49.2	0.1	320 $\pm$ 26	134	26	2.9	18.2	17 $\pm$ 7	0.07 $\pm$ 0.025	13.9 $\pm$ 5.3
239	284.243	2.274	24.1 $\times$ 18.3	62.1	0.2	410 $\pm$ 35	153	32	2.9	18.4	21 $\pm$ 9	0.07 $\pm$ 0.025	14.0 $\pm$ 5.3
240	284.198	2.293	29.7 $\times$ 16.7	45.6	0.2	355 $\pm$ 39	116	20	2.9	18.6	18 $\pm$ 8	0.05 $\pm$ 0.019	10.6 $\pm$ 4.1
241	284.238	2.254	38.8 $\times$ 21.8	-4.4	0.2	563 $\pm$ 53	129	28	2.9	17.6	32 $\pm$ 14	0.05 $\pm$ 0.019	10.7 $\pm$ 4.1
242	284.302	2.240	35.0 $\times$ 28.8	29.1	0.2	471 $\pm$ 47	101	23	2.9	17.8	26 $\pm$ 11	0.03 $\pm$ 0.013	7.4 $\pm$ 2.9
243	284.251	2.261	54.3 $\times$ 30.6	76.9	0.3	1151 $\pm$ 111	117	26	2.9	17.8	63 $\pm$ 28	0.05 $\pm$ 0.02	11.0 $\pm$ 4.3
244	284.250	2.323	38.9 $\times$ 28.8	64.4	0.2	741 $\pm$ 86	131	22	2.9	19.0	37 $\pm$ 16	0.04 $\pm$ 0.017	9.5 $\pm$ 3.7
245	284.245	2.333	24.5 $\times$ 14.9	72.5	0.1	293 $\pm$ 34	129	20	2.9	18.3	15 $\pm$ 7	0.06 $\pm$ 0.022	12.1 $\pm$ 4.7
246	284.243	2.312	44.3 $\times$ 35.4	51.5	0.3	1062 $\pm$ 114	124	22	2.9	19.1	52 $\pm$ 23	0.04 $\pm$ 0.018	9.6 $\pm$ 3.7
247	284.209	2.266	28.9 $\times$ 13.0	4.2	0.1	204 $\pm$ 22	81	16	2.9	18.0	11 $\pm$ 5	0.04 $\pm$ 0.015	8.5 $\pm$ 3.3
248	284.211	2.275	29.4 $\times$ 25.5	-52.3	0.2	381 $\pm$ 45	93	18	2.9	18.1	20 $\pm$ 9	0.04 $\pm$ 0.014	7.8 $\pm$ 3.1
249	284.183	2.285	65.8 $\times$ 30.3	-82.2	0.3	1050 $\pm$ 125	148	23	2.9	18.9	53 $\pm$ 23	0.04 $\pm$ 0.014	7.6 $\pm$ 3.0
250	284.201	2.280	35.6 $\times$ 19.9	-76.9	0.2	300 $\pm$ 40	75	14	2.9	18.4	16 $\pm$ 7	0.03 $\pm$ 0.012	6.3 $\pm$ 2.5
251	284.215	2.324	33.7 $\times$ 22.4	-54.7	0.2	293 $\pm$ 44	92	13	2.9	19.6	14 $\pm$ 6	0.02 $\pm$ 0.01	5.3 $\pm$ 2.1
252	284.275	2.285	32.6 $\times$ 21.2	11.6	0.2	373 $\pm$ 44	88	19	2.9	17.8	21 $\pm$ 9	0.04 $\pm$ 0.016	8.5 $\pm$ 3.3
253	284.231	2.267	48.7 $\times$ 37.6	47.0	0.3	696 $\pm$ 90	77	16	2.9	18.7	36 $\pm$ 16	0.03 $\pm$ 0.01	5.6 $\pm$ 2.2
254	284.235	2.277	29.6 $\times$ 18.1	-29.7	0.2	221 $\pm$ 28	69	14	2.9	19.0	11 $\pm$ 5	0.03 $\pm$ 0.011	5.9 $\pm$ 2.3
255	284.226	2.330	33.8 $\times$ 25.2	-65.9	0.2	284 $\pm$ 47	73	11	2.9	19.6	14 $\pm$ 6	0.02 $\pm$ 0.009	4.6 $\pm$ 1.9
256	284.266	2.322	34.9 $\times$ 22.9	11.2	0.2	463 $\pm$ 59	120	21	2.9	18.2	25 $\pm$ 11	0.04 $\pm$ 0.016	8.8 $\pm$ 3.5
257	284.205	2.260	19.6 $\times$ 15.9	-9.1	0.1	109 $\pm$ 16	69	14	2.9	18.3	6 $\pm$ 3	0.03 $\pm$ 0.01	5.4 $\pm$ 2.2
258	284.196	2.255	31.6 $\times$ 16.1	-39.9	0.2	141 $\pm$ 23	53	10	2.9	18.1	8 $\pm$ 3	0.02 $\pm$ 0.008	4.2 $\pm$ 1.7
259	284.196	2.268	40.4 $\times$ 15.9	-38.4	0.2	184 $\pm$ 28	56	11	2.9	18.1	10 $\pm$ 4	0.02 $\pm$ 0.008	4.4 $\pm$ 1.8
260	284.214	2.309	48.1 $\times$ 41.4	-25.6	0.3	308 $\pm$ 46	103	17	2.9	19.0	15 $\pm$ 7	0.01 $\pm$ 0.004	2.2 $\pm$ 0.9
261	284.221	2.259	44.1 $\times$ 16.9	19.9	0.2	224 $\pm$ 33	67	14	2.9	18.6	12 $\pm$ 5	0.02 $\pm$ 0.008	4.4 $\pm$ 1.8
262	284.028	2.331	33.7 $\times$ 18.6	79.2	0.2	399 $\pm$ 49	130	19	2.9	19.5	19 $\pm$ 8	0.04 $\pm$ 0.016	8.7 $\pm$ 3.4
263	284.140	2.352	25.0 $\times$ 19.6	-14.9	0.2	344 $\pm$ 58	126	9	2.9	19.8	16 $\pm$ 7	0.04 $\pm$ 0.018	9.4 $\pm$ 3.8
264	283.957	2.357	24.4 $\times$ 16.1	57.9	0.1	154 $\pm$ 25	67	10	2.9	18.9	8 $\pm$ 4	0.03 $\pm$ 0.011	5.6 $\pm$ 2.3
265	283.948	2.379	25.2 $\times$ 19.3	-11.4	0.2	279 $\pm$ 40	90	13	2.9	18.1	15 $\pm$ 7	0.04 $\pm$ 0.016	8.8 $\pm$ 3.5
266	284.266	2.358	26.4 $\times$ 15.9	-78.5	0.1	852 $\pm$ 60	401	53	2.9	17.0	51 $\pm$ 22	0.16 $\pm$ 0.061	34.4 $\pm$ 13.1
267	284.269	2.366	69.2 $\times$ 43.4	-71.2	0.4	6530 $\pm$ 545	1439	164	2.9	17.2	378 $\pm$ 163	0.17 $\pm$ 0.065	36.1 $\pm$ 13.8
268	284.302	2.377	63.2 $\times$ 28.7	-58.7	0.3	1345 $\pm$ 150	208	23	2.9	17.5	76 $\pm$ 33	0.06 $\pm$ 0.022	12.0 $\pm$ 4.7
269	284.254	2.354	45.7 $\times$ 13.0	31.1	0.2	329 $\pm$ 37	130	17	2.9	17.5	19 $\pm$ 8	0.04 $\pm$ 0.016	9.0 $\pm$ 3.5
270	284.248	2.359	38.9 $\times$ 28.3	51.5	0.2	724 $\pm$ 87	205	25	2.9	17.7	40 $\pm$ 18	0.05 $\pm$ 0.019	10.4 $\pm$ 4.1
271	284.321	2.387	54.9 $\times$ 16.5	-29.7	0.2	924 $\pm$ 113	208	19	2.9	17.1	54 $\pm$ 24	0.08 $\pm$ 0.032	17.1 $\pm$ 6.7

**Table B2** *continued*

**Table B2** (*continued*)

ID	RA	Dec	Size	PA	R	Flux	$F_{\text{peak}}$	SNR	D	T <sub>dust</sub>	Mass	$\Sigma$	N <sub>H<sub>2</sub></sub>
	( $^{\circ}$ )	( $^{\circ}$ )	( $'' \times ''$ )	( $^{\circ}$ )	(pc)	(mJy)	(mJy beam $^{-1}$ )		(kpc)	(K)	(M $_{\odot}$ )	(g cm $^{-2}$ )	( $\times 10^{21} \text{cm}^{-2}$ )
(1)	(2)	(3)	(4)	(5)	(6)	(7)	(8)	(9)	(10)	(11)	(12)	(13)	(14)
272	284.290	2.365	26.9 $\times$ 15.5	4.4	0.1	252 $\pm$ 37	92	11	2.9	18.8	13 $\pm$ 6	0.04 $\pm$ 0.016	8.7 $\pm$ 3.5
273	283.801	2.353	76.7 $\times$ 64.9	32.6	0.5	7040 $\pm$ 700	430	40	2.9	17.3	407 $\pm$ 179	0.11 $\pm$ 0.043	23.4 $\pm$ 9.1
274	283.792	2.362	20.9 $\times$ 13.2	8.6	0.1	440 $\pm$ 39	243	21	2.9	17.3	25 $\pm$ 11	0.12 $\pm$ 0.048	26.4 $\pm$ 10.2
275	283.786	2.358	18.3 $\times$ 11.2	64.0	0.1	275 $\pm$ 29	201	17	2.9	17.1	16 $\pm$ 7	0.11 $\pm$ 0.041	22.5 $\pm$ 8.7
276	283.837	2.379	23.2 $\times$ 9.0	0.2	0.1	239 $\pm$ 22	173	20	2.9	17.9	13 $\pm$ 6	0.08 $\pm$ 0.033	18.1 $\pm$ 7.0
277	283.822	2.360	28.8 $\times$ 14.1	-70.2	0.1	422 $\pm$ 47	150	16	2.9	17.7	23 $\pm$ 10	0.08 $\pm$ 0.03	16.6 $\pm$ 6.4
278	283.788	2.347	35.7 $\times$ 11.6	61.1	0.1	475 $\pm$ 60	155	13	2.9	17.1	28 $\pm$ 12	0.09 $\pm$ 0.036	19.2 $\pm$ 7.6
279	283.785	2.340	19.4 $\times$ 13.7	6.4	0.1	228 $\pm$ 36	119	10	2.9	17.2	13 $\pm$ 6	0.07 $\pm$ 0.027	14.3 $\pm$ 5.8
280	283.824	2.375	61.4 $\times$ 33.1	-25.8	0.3	1885 $\pm$ 215	404	44	2.9	18.5	98 $\pm$ 43	0.06 $\pm$ 0.025	13.8 $\pm$ 5.4
281	283.832	2.391	39.0 $\times$ 18.1	32.0	0.2	428 $\pm$ 58	108	12	2.9	18.0	23 $\pm$ 10	0.04 $\pm$ 0.018	9.5 $\pm$ 3.8
282	283.829	2.399	28.0 $\times$ 25.3	-4.5	0.2	451 $\pm$ 65	131	14	2.9	17.8	25 $\pm$ 11	0.05 $\pm$ 0.019	10.0 $\pm$ 4.0
283	283.844	2.363	64.6 $\times$ 27.5	-71.4	0.3	822 $\pm$ 123	127	15	2.9	18.3	43 $\pm$ 20	0.03 $\pm$ 0.013	7.0 $\pm$ 2.8
284	283.843	2.396	66.2 $\times$ 24.9	75.5	0.3	598 $\pm$ 95	125	15	2.9	18.3	32 $\pm$ 14	0.03 $\pm$ 0.01	5.5 $\pm$ 2.2
285	284.119	2.444	30.5 $\times$ 27.2	20.9	0.2	537 $\pm$ 94	126	9	2.9	19.9	25 $\pm$ 11	0.04 $\pm$ 0.017	8.6 $\pm$ 3.6
286	284.087	2.447	15.2 $\times$ 13.6	83.5	0.1	174 $\pm$ 27	112	10	2.9	19.8	8 $\pm$ 4	0.05 $\pm$ 0.022	11.4 $\pm$ 4.6
287	284.006	2.385	89.1 $\times$ 47.2	-71.2	0.5	17544 $\pm$ 1121	1678	234	2.9	20.0	807 $\pm$ 348	0.26 $\pm$ 0.098	55.0 $\pm$ 21.0
288	284.018	2.392	50.7 $\times$ 15.4	-51.5	0.2	4105 $\pm$ 254	1046	146	2.9	16.9	244 $\pm$ 106	0.42 $\pm$ 0.159	89.7 $\pm$ 34.0
289	284.023	2.378	62.2 $\times$ 45.8	-69.8	0.4	9301 $\pm$ 614	869	121	2.9	19.8	435 $\pm$ 188	0.21 $\pm$ 0.078	43.8 $\pm$ 16.7
290	284.060	2.359	84.0 $\times$ 70.3	51.0	0.5	17885 $\pm$ 1317	957	114	2.9	16.5	1105 $\pm$ 477	0.25 $\pm$ 0.096	53.7 $\pm$ 20.4
291	284.095	2.341	56.4 $\times$ 36.3	82.2	0.3	13820 $\pm$ 942	4495	405	2.9	26.4	430 $\pm$ 187	0.28 $\pm$ 0.107	60.3 $\pm$ 22.9
292	284.092	2.353	42.5 $\times$ 17.5	53.2	0.2	1799 $\pm$ 126	417	42	2.9	23.5	66 $\pm$ 28	0.12 $\pm$ 0.045	25.4 $\pm$ 9.6
293	283.877	2.286	58.8 $\times$ 33.2	48.5	0.6	3618 $\pm$ 257	430	69	5.1	15.3	781 $\pm$ 338	0.17 $\pm$ 0.066	37.1 $\pm$ 14.1
294	283.891	2.320	101.5 $\times$ 60.0	-41.7	1.0	28895 $\pm$ 1925	3404	482	5.1	20.3	4023 $\pm$ 1748	0.29 $\pm$ 0.109	61.3 $\pm$ 23.3
295	284.031	2.395	34.7 $\times$ 23.3	-77.2	0.2	1725 $\pm$ 120	407	56	2.9	17.6	97 $\pm$ 42	0.16 $\pm$ 0.061	34.3 $\pm$ 13.1
296	283.875	2.298	28.7 $\times$ 10.8	-22.1	0.2	720 $\pm$ 49	302	44	5.1	15.9	146 $\pm$ 63	0.21 $\pm$ 0.078	43.9 $\pm$ 16.6
297	284.093	2.328	32.4 $\times$ 17.5	-69.0	0.2	936 $\pm$ 87	326	30	2.9	17.7	52 $\pm$ 23	0.12 $\pm$ 0.047	26.3 $\pm$ 10.1
298	284.095	2.369	30.1 $\times$ 17.9	52.2	0.2	929 $\pm$ 79	275	27	2.9	23.6	34 $\pm$ 15	0.08 $\pm$ 0.032	18.0 $\pm$ 6.9
299	284.093	2.376	44.6 $\times$ 17.6	-68.9	0.2	1041 $\pm$ 92	291	29	2.9	22.8	40 $\pm$ 17	0.07 $\pm$ 0.026	14.5 $\pm$ 5.5
300	284.077	2.359	41.2 $\times$ 26.8	56.4	0.2	2047 $\pm$ 161	355	38	2.9	18.5	106 $\pm$ 46	0.13 $\pm$ 0.049	27.6 $\pm$ 10.6
301	283.966	2.413	30.6 $\times$ 15.1	55.6	0.2	750 $\pm$ 59	266	37	2.9	16.7	46 $\pm$ 20	0.13 $\pm$ 0.051	28.4 $\pm$ 10.9
302	284.080	2.401	19.1 $\times$ 14.1	84.2	0.1	358 $\pm$ 32	216	23	2.9	21.1	15 $\pm$ 7	0.08 $\pm$ 0.03	16.4 $\pm$ 6.3
303	284.081	2.405	19.2 $\times$ 12.7	-81.7	0.1	349 $\pm$ 30	216	23	2.9	21.1	15 $\pm$ 6	0.08 $\pm$ 0.031	17.5 $\pm$ 6.7
304	283.979	2.391	104.1 $\times$ 43.6	47.9	0.5	6530 $\pm$ 531	364	51	2.9	18.3	343 $\pm$ 149	0.1 $\pm$ 0.039	21.7 $\pm$ 8.3
305	283.911	2.341	34.6 $\times$ 27.3	-23.8	0.4	1355 $\pm$ 108	224	31	5.1	16.9	250 $\pm$ 109	0.12 $\pm$ 0.044	24.5 $\pm$ 9.3
306	283.887	2.298	28.4 $\times$ 16.4	69.3	0.3	627 $\pm$ 48	210	33	5.1	16.8	117 $\pm$ 51	0.11 $\pm$ 0.042	23.4 $\pm$ 8.9
307	283.886	2.339	52.7 $\times$ 26.4	48.5	0.5	1842 $\pm$ 165	303	39	5.1	17.3	328 $\pm$ 143	0.1 $\pm$ 0.04	21.9 $\pm$ 8.4
308	284.031	2.361	30.4 $\times$ 18.1	34.0	0.2	663 $\pm$ 61	205	28	2.9	18.5	34 $\pm$ 15	0.08 $\pm$ 0.032	17.8 $\pm$ 6.9
309	284.090	2.384	34.5 $\times$ 26.4	26.7	0.2	732 $\pm$ 90	155	16	2.9	23.2	27 $\pm$ 12	0.04 $\pm$ 0.016	8.6 $\pm$ 3.4
310	284.085	2.380	26.3 $\times$ 20.2	-85.2	0.2	516 $\pm$ 59	155	16	2.9	23.6	19 $\pm$ 8	0.05 $\pm$ 0.018	10.1 $\pm$ 3.9
311	284.044	2.406	57.8 $\times$ 33.4	-59.1	0.3	1237 $\pm$ 136	151	20	2.9	18.6	64 $\pm$ 28	0.04 $\pm$ 0.017	9.5 $\pm$ 3.7
312	284.080	2.391	39.5 $\times$ 13.4	64.2	0.2	472 $\pm$ 59	153	17	2.9	21.4	20 $\pm$ 9	0.05 $\pm$ 0.02	10.7 $\pm$ 4.2
313	284.027	2.420	48.1 $\times$ 21.4	-83.9	0.2	666 $\pm$ 71	167	23	2.9	19.5	32 $\pm$ 14	0.04 $\pm$ 0.016	8.9 $\pm$ 3.5
314	284.021	2.420	32.9 $\times$ 21.6	79.5	0.2	488 $\pm$ 55	119	16	2.9	19.7	23 $\pm$ 10	0.04 $\pm$ 0.017	9.3 $\pm$ 3.6

**Table B2** *continued*

**Table B2** (*continued*)

ID	RA	Dec	Size	PA	R	Flux	$F_{\text{peak}}$	SNR	D	T <sub>dust</sub>	Mass	$\Sigma$	N <sub>H<sub>2</sub></sub>
	( $^{\circ}$ )	( $^{\circ}$ )	( $'' \times ''$ )	( $^{\circ}$ )	(pc)	(mJy)	(mJy beam $^{-1}$ )		(kpc)	(K)	(M $_{\odot}$ )	(g cm $^{-2}$ )	( $\times 10^{21} \text{cm}^{-2}$ )
(1)	(2)	(3)	(4)	(5)	(6)	(7)	(8)	(9)	(10)	(11)	(12)	(13)	(14)
315	284.047	2.380	49.2 $\times$ 27.4	-25.2	0.3	1115 $\pm$ 125	175	23	2.9	18.7	57 $\pm$ 25	0.06 $\pm$ 0.022	12.1 $\pm$ 4.7
316	284.087	2.412	40.6 $\times$ 31.0	-27.7	0.3	885 $\pm$ 113	162	17	2.9	20.0	41 $\pm$ 18	0.04 $\pm$ 0.017	9.3 $\pm$ 3.7
317	283.967	2.429	41.7 $\times$ 33.1	-73.9	0.3	1118 $\pm$ 115	183	25	2.9	16.9	67 $\pm$ 29	0.07 $\pm$ 0.025	13.9 $\pm$ 5.4
318	283.979	2.435	77.1 $\times$ 32.4	31.0	0.4	1969 $\pm$ 199	309	43	2.9	17.1	115 $\pm$ 51	0.06 $\pm$ 0.024	13.2 $\pm$ 5.1
319	283.920	2.387	30.6 $\times$ 16.5	70.7	0.3	461 $\pm$ 50	146	20	5.1	17.0	84 $\pm$ 37	0.07 $\pm$ 0.028	15.4 $\pm$ 6.0
320	283.920	2.399	50.3 $\times$ 20.3	66.4	0.4	843 $\pm$ 93	158	22	5.1	17.2	151 $\pm$ 67	0.06 $\pm$ 0.025	13.8 $\pm$ 5.4
321	283.926	2.413	82.7 $\times$ 33.5	78.4	0.7	2156 $\pm$ 244	195	27	5.1	17.1	390 $\pm$ 172	0.06 $\pm$ 0.024	13.1 $\pm$ 5.1
322	283.984	2.401	47.4 $\times$ 20.3	-9.2	0.2	555 $\pm$ 63	142	20	2.9	18.8	28 $\pm$ 12	0.04 $\pm$ 0.015	8.3 $\pm$ 3.2
323	284.014	2.416	30.3 $\times$ 18.8	76.7	0.2	401 $\pm$ 46	130	18	2.9	19.7	19 $\pm$ 8	0.04 $\pm$ 0.018	9.5 $\pm$ 3.7
324	283.925	2.364	52.9 $\times$ 29.7	-85.9	0.5	1186 $\pm$ 141	181	25	5.1	17.4	210 $\pm$ 93	0.06 $\pm$ 0.023	12.4 $\pm$ 4.8
325	283.916	2.355	36.1 $\times$ 21.8	-70.9	0.4	458 $\pm$ 53	132	18	5.1	17.8	78 $\pm$ 34	0.04 $\pm$ 0.017	9.2 $\pm$ 3.6
326	284.054	2.409	45.1 $\times$ 29.2	62.4	0.3	864 $\pm$ 113	123	16	2.9	19.9	40 $\pm$ 18	0.04 $\pm$ 0.016	8.7 $\pm$ 3.5
327	284.107	2.361	38.5 $\times$ 10.4	45.0	0.1	230 $\pm$ 38	100	9	2.9	23.5	8 $\pm$ 4	0.03 $\pm$ 0.012	6.0 $\pm$ 2.5
328	283.938	2.436	123.3 $\times$ 49.7	-43.0	1.0	3165 $\pm$ 411	143	20	5.1	17.3	561 $\pm$ 252	0.04 $\pm$ 0.016	8.5 $\pm$ 3.4
329	283.912	2.413	19.4 $\times$ 10.7	-74.0	0.2	142 $\pm$ 18	95	13	5.1	17.9	24 $\pm$ 11	0.05 $\pm$ 0.02	10.7 $\pm$ 4.2
330	283.930	2.353	30.4 $\times$ 20.6	-82.2	0.3	397 $\pm$ 53	106	15	5.1	17.6	69 $\pm$ 31	0.05 $\pm$ 0.019	10.2 $\pm$ 4.0
331	283.903	2.357	34.5 $\times$ 22.2	82.5	0.3	359 $\pm$ 49	82	11	5.1	17.8	61 $\pm$ 27	0.03 $\pm$ 0.014	7.4 $\pm$ 2.9
332	284.112	2.322	39.3 $\times$ 11.7	31.4	0.2	171 $\pm$ 28	122	11	2.9	18.1	9 $\pm$ 4	0.03 $\pm$ 0.011	5.7 $\pm$ 2.3
333	284.028	2.446	57.9 $\times$ 18.7	81.6	0.2	409 $\pm$ 62	95	12	2.9	18.5	21 $\pm$ 10	0.03 $\pm$ 0.011	5.6 $\pm$ 2.3
334	284.093	2.400	47.6 $\times$ 25.3	4.0	0.2	365 $\pm$ 64	122	12	2.9	21.3	15 $\pm$ 7	0.02 $\pm$ 0.007	3.7 $\pm$ 1.5
335	284.056	2.423	29.3 $\times$ 14.2	-83.0	0.1	255 $\pm$ 39	94	12	2.9	20.2	12 $\pm$ 5	0.04 $\pm$ 0.015	8.0 $\pm$ 3.3
336	284.008	2.358	36.5 $\times$ 27.1	-45.0	0.2	373 $\pm$ 51	119	17	2.9	18.6	19 $\pm$ 9	0.03 $\pm$ 0.01	5.6 $\pm$ 2.2
337	283.998	2.356	58.6 $\times$ 20.1	-44.0	0.2	655 $\pm$ 73	200	28	2.9	18.8	33 $\pm$ 15	0.04 $\pm$ 0.015	8.1 $\pm$ 3.2
338	283.949	2.425	51.9 $\times$ 21.3	-38.2	0.4	373 $\pm$ 60	93	13	5.1	17.5	65 $\pm$ 29	0.03 $\pm$ 0.01	5.5 $\pm$ 2.2
339	284.038	2.449	28.1 $\times$ 14.0	-33.3	0.1	129 $\pm$ 24	64	8	2.9	18.9	6 $\pm$ 3	0.02 $\pm$ 0.009	4.7 $\pm$ 2.0
340	284.068	2.407	41.0 $\times$ 30.9	-30.6	0.3	233 $\pm$ 40	112	13	2.9	20.3	11 $\pm$ 5	0.01 $\pm$ 0.005	2.4 $\pm$ 1.0
341	283.909	2.372	29.2 $\times$ 18.9	30.4	0.3	164 $\pm$ 29	65	9	5.1	17.9	28 $\pm$ 13	0.02 $\pm$ 0.009	4.7 $\pm$ 1.9
342	283.898	2.246	27.4 $\times$ 18.2	69.3	0.3	299 $\pm$ 34	133	27	5.1	17.5	52 $\pm$ 23	0.05 $\pm$ 0.018	9.7 $\pm$ 3.8
343	283.886	2.253	102.7 $\times$ 29.4	77.6	0.7	837 $\pm$ 97	170	31	5.1	17.4	148 $\pm$ 65	0.02 $\pm$ 0.008	4.5 $\pm$ 1.8
344	283.907	2.266	102.9 $\times$ 44.5	27.4	0.8	1040 $\pm$ 130	131	25	5.1	18.1	172 $\pm$ 76	0.02 $\pm$ 0.006	3.5 $\pm$ 1.4
345	284.008	2.479	28.4 $\times$ 19.9	59.1	0.2	356 $\pm$ 52	96	12	2.9	18.3	19 $\pm$ 8	0.04 $\pm$ 0.018	9.5 $\pm$ 3.8
346	283.989	2.470	29.3 $\times$ 20.8	73.5	0.2	242 $\pm$ 40	78	10	2.9	17.8	13 $\pm$ 6	0.03 $\pm$ 0.012	6.3 $\pm$ 2.6
347	283.943	2.488	19.9 $\times$ 11.3	-19.0	0.2	98 $\pm$ 17	71	9	5.1	17.0	18 $\pm$ 8	0.03 $\pm$ 0.014	7.4 $\pm$ 3.0
348	283.884	2.482	61.0 $\times$ 46.1	-5.5	0.4	3379 $\pm$ 367	618	71	2.9	17.1	198 $\pm$ 88	0.09 $\pm$ 0.037	20.2 $\pm$ 7.9
349	283.938	2.513	22.1 $\times$ 11.1	-47.3	0.2	135 $\pm$ 22	88	9	5.1	16.7	25 $\pm$ 12	0.05 $\pm$ 0.018	9.6 $\pm$ 3.9
350	283.981	2.546	22.6 $\times$ 18.8	-14.2	0.3	512 $\pm$ 70	231	18	5.1	17.3	91 $\pm$ 41	0.09 $\pm$ 0.037	19.9 $\pm$ 7.9

NOTE—The relative uncertainty of parameters of both length and width is 10%.

## REFERENCES

- Anderson, L. D., Bania, T. M., Balser, D. S., et al. 2014, *ApJS*, 212, 1, doi: [10.1088/0067-0049/212/1/1](https://doi.org/10.1088/0067-0049/212/1/1)
- André, P., Di Francesco, J., Ward-Thompson, D., et al. 2014, in *Protostars and Planets VI*, ed. H. Beuther, R. S. Klessen, C. P. Dullemond, & T. Henning, 27–51, doi: [10.2458/azu\\_uapress\\_9780816531240-ch002](https://doi.org/10.2458/azu_uapress_9780816531240-ch002)

- André, P., Men'shchikov, A., Bontemps, S., et al. 2010, *A&A*, 518, L102, doi: [10.1051/0004-6361/201014666](https://doi.org/10.1051/0004-6361/201014666)
- Arzoumanian, D., Arakawa, S., Kobayashi, M. I. N., et al. 2023, *ApJL*, 947, L29, doi: [10.3847/2041-8213/acc849](https://doi.org/10.3847/2041-8213/acc849)
- Astropy Collaboration, Robitaille, T. P., Tollerud, E. J., et al. 2013, *A&A*, 558, A33, doi: [10.1051/0004-6361/201322068](https://doi.org/10.1051/0004-6361/201322068)
- Barbary, K. 2016, *The Journal of Open Source Software*, 1, 58, doi: [10.21105/joss.00058](https://doi.org/10.21105/joss.00058)
- Barnes, A. T., Kong, S., Tan, J. C., et al. 2016, *MNRAS*, 458, 1990, doi: [10.1093/mnras/stw403](https://doi.org/10.1093/mnras/stw403)
- Barnes, A. T., Henshaw, J. D., Fontani, F., et al. 2021, *MNRAS*, 503, 4601, doi: [10.1093/mnras/stab803](https://doi.org/10.1093/mnras/stab803)
- Benjamin, R. A., Churchwell, E., Babler, B. L., et al. 2003, *PASP*, 115, 953, doi: [10.1086/376696](https://doi.org/10.1086/376696)
- Bertin, E., & Arnouts, S. 1996, *A&AS*, 117, 393, doi: [10.1051/aas:1996164](https://doi.org/10.1051/aas:1996164)
- Bronfman, L., Nyman, L. A., & May, J. 1996, *A&AS*, 115, 81
- Brunthaler, A., Menten, K. M., Dzib, S. A., et al. 2021, *A&A*, 651, A85, doi: [10.1051/0004-6361/202039856](https://doi.org/10.1051/0004-6361/202039856)
- Chen, C.-Y., & Ostriker, E. C. 2015, *ApJ*, 810, 126, doi: [10.1088/0004-637X/810/2/126](https://doi.org/10.1088/0004-637X/810/2/126)
- Contreras, Y., Schuller, F., Urquhart, J. S., et al. 2013, *A&A*, 549, A45, doi: [10.1051/0004-6361/201220155](https://doi.org/10.1051/0004-6361/201220155)
- Currie, M. J., Berry, D. S., Jenness, T., et al. 2014, in *Astronomical Society of the Pacific Conference Series*, Vol. 485, *Astronomical Data Analysis Software and Systems XXIII*, ed. N. Manset & P. Forshay, 391
- Dunham, M. K., Robitaille, T. P., Evans, Neal J., I., et al. 2011, *ApJ*, 731, 90, doi: [10.1088/0004-637X/731/2/90](https://doi.org/10.1088/0004-637X/731/2/90)
- Dzib, S. A., Yang, A. Y., Urquhart, J. S., et al. 2023, *A&A*, 670, A9, doi: [10.1051/0004-6361/202143019](https://doi.org/10.1051/0004-6361/202143019)
- Feng, J., Smith, R. J., Hacar, A., Clark, S. E., & Seifried, D. 2024, *MNRAS*, 528, 6370, doi: [10.1093/mnras/stae407](https://doi.org/10.1093/mnras/stae407)
- Fiege, J. D., & Pudritz, R. E. 2000, *MNRAS*, 311, 85, doi: [10.1046/j.1365-8711.2000.03066.x](https://doi.org/10.1046/j.1365-8711.2000.03066.x)
- Giannetti, A., Brand, J., Sánchez-Monge, Á., et al. 2013, *A&A*, 556, A16, doi: [10.1051/0004-6361/201321456](https://doi.org/10.1051/0004-6361/201321456)
- Gómez, G. C., & Vázquez-Semadeni, E. 2014, *ApJ*, 791, 124, doi: [10.1088/0004-637X/791/2/124](https://doi.org/10.1088/0004-637X/791/2/124)
- Gong, M., & Ostriker, E. C. 2015, *ApJ*, 806, 31, doi: [10.1088/0004-637X/806/1/31](https://doi.org/10.1088/0004-637X/806/1/31)
- Guzmán, A. E., Sanhueza, P., Contreras, Y., et al. 2015, *ApJ*, 815, 130, doi: [10.1088/0004-637X/815/2/130](https://doi.org/10.1088/0004-637X/815/2/130)
- Hacar, A., Clark, S. E., Heitsch, F., et al. 2023, in *Astronomical Society of the Pacific Conference Series*, Vol. 534, *Protostars and Planets VII*, ed. S. Inutsuka, Y. Aikawa, T. Muto, K. Tomida, & M. Tamura, 153, doi: [10.48550/arXiv.2203.09562](https://doi.org/10.48550/arXiv.2203.09562)
- He, Y.-X., Zhou, J.-J., Esimbek, J., et al. 2015, *MNRAS*, 450, 1926, doi: [10.1093/mnras/stv732](https://doi.org/10.1093/mnras/stv732)
- He, Y.-X., Liu, H.-L., Tang, X.-D., et al. 2023, *ApJ*, 957, 61, doi: [10.3847/1538-4357/acf766](https://doi.org/10.3847/1538-4357/acf766)
- Heyer, M., Krawczyk, C., Duval, J., & Jackson, J. M. 2009, *ApJ*, 699, 1092, doi: [10.1088/0004-637X/699/2/1092](https://doi.org/10.1088/0004-637X/699/2/1092)
- Hildebrand, R. H. 1983, *QJRAS*, 24, 267
- Hogge, T., Jackson, J., Stephens, I., et al. 2018, *ApJS*, 237, 27, doi: [10.3847/1538-4365/aacf94](https://doi.org/10.3847/1538-4365/aacf94)
- Hou, L. G., & Han, J. L. 2014, *A&A*, 569, A125, doi: [10.1051/0004-6361/201424039](https://doi.org/10.1051/0004-6361/201424039)
- Hu, B., Menten, K. M., Wu, Y., et al. 2016, *ApJ*, 833, 18, doi: [10.3847/0004-637X/833/1/18](https://doi.org/10.3847/0004-637X/833/1/18)
- Inoue, T., & Fukui, Y. 2013, *ApJL*, 774, L31, doi: [10.1088/2041-8205/774/2/L31](https://doi.org/10.1088/2041-8205/774/2/L31)
- Inoue, T., Hennebelle, P., Fukui, Y., et al. 2018, *PASJ*, 70, S53, doi: [10.1093/pasj/psx089](https://doi.org/10.1093/pasj/psx089)
- Jackson, J. M., Rathborne, J. M., Shah, R. Y., et al. 2006, *ApJS*, 163, 145, doi: [10.1086/500091](https://doi.org/10.1086/500091)
- Jayasinghe, T., Dixon, D., Povich, M. S., et al. 2019, *MNRAS*, 488, 1141, doi: [10.1093/mnras/stz1738](https://doi.org/10.1093/mnras/stz1738)
- Jiao, S., Lin, Y., Shui, X., et al. 2022, *Science China Physics, Mechanics, and Astronomy*, 65, 299511, doi: [10.1007/s11433-021-1902-3](https://doi.org/10.1007/s11433-021-1902-3)
- Jiménez-Serra, I., Caselli, P., Fontani, F., et al. 2014, *MNRAS*, 439, 1996, doi: [10.1093/mnras/stu078](https://doi.org/10.1093/mnras/stu078)
- Kalcheva, I. E., Hoare, M. G., Urquhart, J. S., et al. 2018, *A&A*, 615, A103, doi: [10.1051/0004-6361/201832734](https://doi.org/10.1051/0004-6361/201832734)
- Kauffmann, J., Bertoldi, F., Bourke, T. L., Evans, N. J., I., & Lee, C. W. 2008, *A&A*, 487, 993, doi: [10.1051/0004-6361:200809481](https://doi.org/10.1051/0004-6361:200809481)
- Koch, E. W., & Rosolowsky, E. W. 2015, *MNRAS*, 452, 3435, doi: [10.1093/mnras/stv1521](https://doi.org/10.1093/mnras/stv1521)
- Krumholz, M. R., & McKee, C. F. 2008, *Nature*, 451, 1082, doi: [10.1038/nature06620](https://doi.org/10.1038/nature06620)
- Kuhn, M. A., de Souza, R. S., Krone-Martins, A., et al. 2021, *ApJS*, 254, 33, doi: [10.3847/1538-4365/abe465](https://doi.org/10.3847/1538-4365/abe465)
- Kumar, M. S. N., Arzoumanian, D., Men'shchikov, A., et al. 2022, *A&A*, 658, A114, doi: [10.1051/0004-6361/202140363](https://doi.org/10.1051/0004-6361/202140363)
- Kumar, M. S. N., Palmeirim, P., Arzoumanian, D., & Inutsuka, S. I. 2020, *A&A*, 642, A87, doi: [10.1051/0004-6361/202038232](https://doi.org/10.1051/0004-6361/202038232)
- Ladeyschikov, D. A., Bayandina, O. S., & Sobolev, A. M. 2019, *AJ*, 158, 233, doi: [10.3847/1538-3881/ab4b4c](https://doi.org/10.3847/1538-3881/ab4b4c)
- Larson, R. B. 1981, *MNRAS*, 194, 809, doi: [10.1093/mnras/194.4.809](https://doi.org/10.1093/mnras/194.4.809)
- Li, G.-X., Urquhart, J. S., Leurini, S., et al. 2016, *A&A*, 591, A5, doi: [10.1051/0004-6361/201527468](https://doi.org/10.1051/0004-6361/201527468)

- Li, Q., Zhou, J., Esimbek, J., et al. 2018, ApJ, 867, 167, doi: [10.3847/1538-4357/aae2b8](https://doi.org/10.3847/1538-4357/aae2b8)
- Lisa, M., & Bot, H. 2017, My Research Software, 2.0.4, doi: [10.5281/zenodo.1234](https://doi.org/10.5281/zenodo.1234)
- Liu, H. B., Jiménez-Serra, I., Ho, P. T. P., et al. 2012a, ApJ, 756, 10, doi: [10.1088/0004-637X/756/1/10](https://doi.org/10.1088/0004-637X/756/1/10)
- Liu, H. B., Quintana-Lacaci, G., Wang, K., et al. 2012b, ApJ, 745, 61, doi: [10.1088/0004-637X/745/1/61](https://doi.org/10.1088/0004-637X/745/1/61)
- Liu, H.-L., Sanhueza, P., Liu, T., et al. 2020, ApJ, 901, 31, doi: [10.3847/1538-4357/abafde](https://doi.org/10.3847/1538-4357/abafde)
- Liu, H.-L., Stutz, A., & Yuan, J.-H. 2019, MNRAS, 487, 1259, doi: [10.1093/mnras/stz1340](https://doi.org/10.1093/mnras/stz1340)
- Liu, H.-L., Liu, T., Evans, N.J., I., et al. 2021, MNRAS, 505, 2801, doi: [10.1093/mnras/stab1352](https://doi.org/10.1093/mnras/stab1352)
- Liu, H.-L., Tej, A., Liu, T., et al. 2022, MNRAS, 510, 5009, doi: [10.1093/mnras/stab2757](https://doi.org/10.1093/mnras/stab2757)
- . 2023, MNRAS, 522, 3719, doi: [10.1093/mnras/stad047](https://doi.org/10.1093/mnras/stad047)
- Liu, T., Li, P. S., Juvela, M., et al. 2018, ApJ, 859, 151, doi: [10.3847/1538-4357/aac025](https://doi.org/10.3847/1538-4357/aac025)
- López-Sepulcre, A., Cesaroni, R., & Walmsley, C. M. 2010, A&A, 517, A66, doi: [10.1051/0004-6361/201014252](https://doi.org/10.1051/0004-6361/201014252)
- Lu, X., Zhang, Q., Liu, H. B., Wang, J., & Gu, Q. 2014, ApJ, 790, 84, doi: [10.1088/0004-637X/790/2/84](https://doi.org/10.1088/0004-637X/790/2/84)
- Lu, X., Zhang, Q., Liu, H. B., et al. 2018, ApJ, 855, 9, doi: [10.3847/1538-4357/aaad11](https://doi.org/10.3847/1538-4357/aaad11)
- Mairs, S., Dempsey, J. T., Bell, G. S., et al. 2021, AJ, 162, 191, doi: [10.3847/1538-3881/ac18bf](https://doi.org/10.3847/1538-3881/ac18bf)
- Molinari, S., Swinyard, B., Bally, J., et al. 2010, PASP, 122, 314, doi: [10.1086/651314](https://doi.org/10.1086/651314)
- Motte, F., Bontemps, S., & Louvet, F. 2018, ARA&A, 56, 41, doi: [10.1146/annurev-astro-091916-055235](https://doi.org/10.1146/annurev-astro-091916-055235)
- Myers, P. C. 2009, ApJ, 700, 1609, doi: [10.1088/0004-637X/700/2/1609](https://doi.org/10.1088/0004-637X/700/2/1609)
- Nguyen, H., Rugel, M. R., Murugeshan, C., et al. 2022, A&A, 666, A59, doi: [10.1051/0004-6361/202244115](https://doi.org/10.1051/0004-6361/202244115)
- Nguyen Luong, Q., Motte, F., Hennemann, M., et al. 2011, A&A, 535, A76, doi: [10.1051/0004-6361/201117831](https://doi.org/10.1051/0004-6361/201117831)
- Ossenkopf, V., & Henning, T. 1994, A&A, 291, 943
- Ostriker, J. 1964, ApJ, 140, 1056, doi: [10.1086/148005](https://doi.org/10.1086/148005)
- Ouyang, X.-J., Chen, X., Shen, Z.-Q., et al. 2019, ApJS, 245, 12, doi: [10.3847/1538-4365/ab4db2](https://doi.org/10.3847/1538-4365/ab4db2)
- Padoan, P., Pan, L., Juvela, M., Haugbølle, T., & Nordlund, Å. 2020, ApJ, 900, 82, doi: [10.3847/1538-4357/abaaa47](https://doi.org/10.3847/1538-4357/abaaa47)
- Pan, S., Liu, H.-L., & Qin, S.-L. 2023, MNRAS, 519, 3851, doi: [10.1093/mnras/stac3658](https://doi.org/10.1093/mnras/stac3658)
- . 2024, ApJ, 960, 76, doi: [10.3847/1538-4357/ad10ac](https://doi.org/10.3847/1538-4357/ad10ac)
- Peretto, N., & Fuller, G. A. 2009, A&A, 505, 405, doi: [10.1051/0004-6361/200912127](https://doi.org/10.1051/0004-6361/200912127)
- Peretto, N., Lenfestey, C., Fuller, G. A., et al. 2016, A&A, 590, A72, doi: [10.1051/0004-6361/201527064](https://doi.org/10.1051/0004-6361/201527064)
- Peretto, N., Fuller, G. A., Duarte-Cabral, A., et al. 2013, A&A, 555, A112, doi: [10.1051/0004-6361/201321318](https://doi.org/10.1051/0004-6361/201321318)
- Peretto, N., Fuller, G. A., André, P., et al. 2014, A&A, 561, A83, doi: [10.1051/0004-6361/201322172](https://doi.org/10.1051/0004-6361/201322172)
- Pineda, J. E., Arzoumanian, D., Andre, P., et al. 2023, in Astronomical Society of the Pacific Conference Series, Vol. 534, Protostars and Planets VII, ed. S. Inutsuka, Y. Aikawa, T. Muto, K. Tomida, & M. Tamura, 233, doi: [10.48550/arXiv.2205.03935](https://doi.org/10.48550/arXiv.2205.03935)
- Polychroni, D., Schisano, E., Elia, D., et al. 2013, ApJL, 777, L33, doi: [10.1088/2041-8205/777/2/L33](https://doi.org/10.1088/2041-8205/777/2/L33)
- Rathborne, J. M., Jackson, J. M., Chambers, E. T., et al. 2010, ApJ, 715, 310, doi: [10.1088/0004-637X/715/1/310](https://doi.org/10.1088/0004-637X/715/1/310)
- Reid, M. J., Dame, T. M., Menten, K. M., & Brunthaler, A. 2016, ApJ, 823, 77, doi: [10.3847/0004-637X/823/2/77](https://doi.org/10.3847/0004-637X/823/2/77)
- Reid, M. J., Menten, K. M., Brunthaler, A., et al. 2019, ApJ, 885, 131, doi: [10.3847/1538-4357/ab4a11](https://doi.org/10.3847/1538-4357/ab4a11)
- Ren, Z., Zhu, L., Shi, H., et al. 2021, MNRAS, 505, 5183, doi: [10.1093/mnras/stab1509](https://doi.org/10.1093/mnras/stab1509)
- Rigby, A. J., Peretto, N., Adam, R., et al. 2021, MNRAS, 502, 4576, doi: [10.1093/mnras/stab200](https://doi.org/10.1093/mnras/stab200)
- Rosolowsky, E. W., Pineda, J. E., Kauffmann, J., & Goodman, A. A. 2008, ApJ, 679, 1338, doi: [10.1086/587685](https://doi.org/10.1086/587685)
- Saha, A., Tej, A., Liu, H.-L., et al. 2022, MNRAS, 516, 1983, doi: [10.1093/mnras/stac2353](https://doi.org/10.1093/mnras/stac2353)
- Sánchez-Monge, Á., Palau, A., Fontani, F., et al. 2013, MNRAS, 432, 3288, doi: [10.1093/mnras/stt679](https://doi.org/10.1093/mnras/stt679)
- Sanhueza, P., Jackson, J. M., Foster, J. B., et al. 2012, ApJ, 756, 60, doi: [10.1088/0004-637X/756/1/60](https://doi.org/10.1088/0004-637X/756/1/60)
- Sanhueza, P., Jackson, J. M., Zhang, Q., et al. 2017, ApJ, 841, 97, doi: [10.3847/1538-4357/aa6ff8](https://doi.org/10.3847/1538-4357/aa6ff8)
- Sanhueza, P., Girart, J. M., Padovani, M., et al. 2021, ApJL, 915, L10, doi: [10.3847/2041-8213/ac081c](https://doi.org/10.3847/2041-8213/ac081c)
- Schisano, E., Molinari, S., Elia, D., et al. 2020, MNRAS, 492, 5420, doi: [10.1093/mnras/stz3466](https://doi.org/10.1093/mnras/stz3466)
- Schneider, N., Csengeri, T., Hennemann, M., et al. 2012, A&A, 540, L11, doi: [10.1051/0004-6361/201118566](https://doi.org/10.1051/0004-6361/201118566)
- Schuller, F., Menten, K. M., Contreras, Y., et al. 2009, A&A, 504, 415, doi: [10.1051/0004-6361/200811568](https://doi.org/10.1051/0004-6361/200811568)
- Shimajiri, Y., André, P., Ntormousi, E., et al. 2019, A&A, 632, A83, doi: [10.1051/0004-6361/201935689](https://doi.org/10.1051/0004-6361/201935689)
- Shirley, Y. L., Huard, T. L., Pontoppidan, K. M., et al. 2011, ApJ, 728, 143, doi: [10.1088/0004-637X/728/2/143](https://doi.org/10.1088/0004-637X/728/2/143)
- Simon, R., Rathborne, J. M., Shah, R. Y., Jackson, J. M., & Chambers, E. T. 2006, ApJ, 653, 1325, doi: [10.1086/508915](https://doi.org/10.1086/508915)
- Smith, R. J., Glover, S. C. O., Klessen, R. S., & Fuller, G. A. 2016, MNRAS, 455, 3640, doi: [10.1093/mnras/stv2559](https://doi.org/10.1093/mnras/stv2559)

- Smith, R. J., Longmore, S., & Bonnell, I. 2009, MNRAS, 400, 1775, doi: [10.1111/j.1365-2966.2009.15621.x](https://doi.org/10.1111/j.1365-2966.2009.15621.x)
- Sokolov, V., Wang, K., Pineda, J. E., et al. 2017, A&A, 606, A133, doi: [10.1051/0004-6361/201630350](https://doi.org/10.1051/0004-6361/201630350)
- Solomon, P. M., Rivolo, A. R., Barrett, J., & Yahil, A. 1987, ApJ, 319, 730, doi: [10.1086/165493](https://doi.org/10.1086/165493)
- Suri, S., Sánchez-Monge, Á., Schilke, P., et al. 2019, A&A, 623, A142, doi: [10.1051/0004-6361/201834049](https://doi.org/10.1051/0004-6361/201834049)
- Tafalla, M., & Hacar, A. 2015, A&A, 574, A104, doi: [10.1051/0004-6361/201424576](https://doi.org/10.1051/0004-6361/201424576)
- Taniguchi, K., Sanhueza, P., Oguin, F. A., et al. 2023, ApJ, 950, 57, doi: [10.3847/1538-4357/acca1d](https://doi.org/10.3847/1538-4357/acca1d)
- Thompson, M. A., Hatchell, J., Walsh, A. J., MacDonald, G. H., & Millar, T. J. 2006, A&A, 453, 1003, doi: [10.1051/0004-6361:20054383](https://doi.org/10.1051/0004-6361:20054383)
- Umemoto, T., Minamidani, T., Kuno, N., et al. 2017, PASJ, 69, 78, doi: [10.1093/pasj/psx061](https://doi.org/10.1093/pasj/psx061)
- Urquhart, J. S., Hoare, M. G., Lumsden, S. L., Oudmaijer, R. D., & Moore, T. J. T. 2008, in Astronomical Society of the Pacific Conference Series, Vol. 387, Massive Star Formation: Observations Confront Theory, ed. H. Beuther, H. Linz, & T. Henning, 381, doi: [10.48550/arXiv.0711.4715](https://doi.org/10.48550/arXiv.0711.4715)
- Urquhart, J. S., Morgan, L. K., Figura, C. C., et al. 2011, MNRAS, 418, 1689, doi: [10.1111/j.1365-2966.2011.19594.x](https://doi.org/10.1111/j.1365-2966.2011.19594.x)
- Urquhart, J. S., Csengeri, T., Wyrowski, F., et al. 2014a, A&A, 568, A41, doi: [10.1051/0004-6361/201424126](https://doi.org/10.1051/0004-6361/201424126)
- Urquhart, J. S., Moore, T. J. T., Csengeri, T., et al. 2014b, MNRAS, 443, 1555, doi: [10.1093/mnras/stu1207](https://doi.org/10.1093/mnras/stu1207)
- Urquhart, J. S., König, C., Giannetti, A., et al. 2018, MNRAS, 473, 1059, doi: [10.1093/mnras/stx2258](https://doi.org/10.1093/mnras/stx2258)
- Vázquez-Semadeni, E., Palau, A., Ballesteros-Paredes, J., Gómez, G. C., & Zamora-Avilés, M. 2019, MNRAS, 490, 3061, doi: [10.1093/mnras/stz2736](https://doi.org/10.1093/mnras/stz2736)
- Wang, K., Testi, L., Burkert, A., et al. 2016, ApJS, 226, 9, doi: [10.3847/0067-0049/226/1/9](https://doi.org/10.3847/0067-0049/226/1/9)
- Wienen, M., Wyrowski, F., Schuller, F., et al. 2012, A&A, 544, A146, doi: [10.1051/0004-6361/201118107](https://doi.org/10.1051/0004-6361/201118107)
- Xie, J., Fuller, G. A., Li, D., et al. 2021, Science China Physics, Mechanics, and Astronomy, 64, 279511, doi: [10.1007/s11433-021-1695-0](https://doi.org/10.1007/s11433-021-1695-0)
- Xu, F., Wang, K., Liu, T., et al. 2024, ApJS, 270, 9, doi: [10.3847/1538-4365/acfee5](https://doi.org/10.3847/1538-4365/acfee5)
- Xu, F.-W., Wang, K., Liu, T., et al. 2023, MNRAS, 520, 3259, doi: [10.1093/mnras/stad012](https://doi.org/10.1093/mnras/stad012)
- Yang, A. Y., Thompson, M. A., Urquhart, J. S., & Tian, W. W. 2018, ApJS, 235, 3, doi: [10.3847/1538-4365/aaa297](https://doi.org/10.3847/1538-4365/aaa297)
- Yang, A. Y., Dzib, S. A., Urquhart, J. S., et al. 2023a, A&A, 680, A92, doi: [10.1051/0004-6361/202347563](https://doi.org/10.1051/0004-6361/202347563)
- Yang, D., Liu, H.-L., Tej, A., et al. 2023b, ApJ, 953, 40, doi: [10.3847/1538-4357/acdf42](https://doi.org/10.3847/1538-4357/acdf42)
- Yuan, J., Li, J.-Z., Wu, Y., et al. 2018, ApJ, 852, 12, doi: [10.3847/1538-4357/aa9d40](https://doi.org/10.3847/1538-4357/aa9d40)
- Zavagno, A., Dupé, F. X., Bensaid, S., et al. 2023, A&A, 669, A120, doi: [10.1051/0004-6361/202244103](https://doi.org/10.1051/0004-6361/202244103)
- Zhang, C., Zhang, G.-Y., Li, J.-Z., & Yuan, J.-H. 2023, ApJS, 264, 24, doi: [10.3847/1538-4365/aca325](https://doi.org/10.3847/1538-4365/aca325)
- Zhou, J.-W., Liu, T., Evans, N. J., et al. 2022, MNRAS, 514, 6038, doi: [10.1093/mnras/stac1735](https://doi.org/10.1093/mnras/stac1735)
- Zinnecker, H., & Yorke, H. W. 2007, ARA&A, 45, 481, doi: [10.1146/annurev.astro.44.051905.092549](https://doi.org/10.1146/annurev.astro.44.051905.092549)